Modelling of Compression Resin Transfer Moulding Process Using Fast Cure Resins for Ground Transportation Applications

Sidharth Sarojini Narayana

Department of Mechanical Engineering

McGill University

A thesis submitted to McGill University

in partial fulfilment of the requirements of the degree of

Doctor of Philosophy

"Dream, Dream, Dream. Dream transform into thoughts and thoughts result in action"

Dr. A.P.J. Abdul Kalam

Former President of India (1931-2015)

TABLE OF CONTENTS

ABSTRACT

The reduction of cost and process cycle time is a major challenge faced by the ground transportation industry when introducing composite components in their design. To address this issue, researchers over the last decade have developed fast curing thermosetting resin systems. This has paved the way for the use of the cost-effective compression resin transfer moulding (CRTM) process, a variant of the resin transfer moulding (RTM) process. However, the dynamic nature of the resin poses a high risk of manufacturing defects and poor-quality parts. Moreover, there is a lack of sufficient data regarding the application of fast curing resins in industrial settings for the manufacturing of components used in ground transportation.

The aim of the present work was to develop a fully coupled process model for the CRTM process using fast curing resins. Cure kinetic and viscosity models were developed for four epoxy and one polyester fast curing resin system. Permeability and compaction material models were developed for a glass non-crimp fabric (NCF). Initial simulations were performed on a flat tool geometry using a fluid-solid coupled solver, which is the latest feature of the tool PAM-RTM from the ESI group. The cure kinetics and viscosity material models were implemented as user-defined subroutines using C scripts. The results were validated through interrupted filling experiments and sensor (pressure and temperature) readings. Once this was established, a complex 3D seat base demonstrator part for ground transportation application was simulated. The parameters obtained from the simulation were used to manufacture the seat base with minimal porosity. The total fill time for complete injection of the part showed an accuracy of 73%. This case study demonstrated the ability of the process modelling approach to manufacture a complex demonstrator part using a fast curing resin. Finally, an optimization tool was developed based on a dimensionless characteristic number to generate mouldability diagrams. This approach provides details of the optimal fill time for a given mould temperature and resin injection pressure based on a single simulation result. The use of such tool can help industries to reduce the number of simulations and experimental trials thereby minimizing cost and cycle time.

RÉSUMÉ

La réduction des coûts et de la durée du cycle de mise en forme constitue un défi majeur auquel est confrontée l'industrie du transport terrestre lors de l'introduction de composantes composites dans leur conception. Pour résoudre ce problème, les chercheurs ont développé, au cours de la dernière décennie, des systèmes de résine thermodurcissable à polymérization rapide. Cela a permis l'utilisation d'un procédé de moulage efficace, le moulage par transfert de résine par compression (CRTM), une variante du procédé de moulage par transfert de résine (RTM). Cependant, la polymérization dynamique de la résine présente un risque élevé de présence de défauts de fabrication et de pièces de mauvaise qualité. De plus, il y a un manque de données suffisantes concernant l'application de ces résines en milieu industriel pour la fabrication de composantes utilisés dans le transport terrestre.

Le but de cette thèse était de développer un modèle de mise en forme entièrement couplé pour le procédé CRTM utilisant des résines à polymérization rapide. Des modèles de cinétique de polymérization et de viscosité ont été développés pour quatre systèmes de résine époxy et une polyester. Des modèles de perméabilité et de compaction des renforts ont été développés pour un tissu de verre non tissé (NCF). Les premières simulations ont été réalisées sur une géométrie d'outil plat à l'aide d'un solveur couplé fluide-solide, qui est la dernière fonctionnalité de l'outil PAM-RTM du groupe ESI. Les modèles de cinétique de polymérization et de viscosité des matériaux ont été implémentés sous forme de sous-programmes définis par l'utilisateur à l'aide de programmes en langage C. Les résultats ont été validés par des expériences de remplissage interrompues et des relevés de capteurs (pression et température). Une fois cela établi, une pièce de démonstration complexe de base de siège destinée aux applications de transport terrestre a été simulée. Les paramètres obtenus à partir de la simulation ont été utilisés pour fabriquer une base de siège ayant une très faible porosité. La prédiction du temps de remplissage total pour une injection complète de la pièce était de 73 %. Cette étude de cas a démontré la possibilité de de la modélisation du procédé CRTM pour la fabrication de pièces complexes en utilisant des résines à polymérization rapide. Enfin, un outil d'optimisation a été développé sur la base d'un nombre caractéristique non dimensionnel pour générer des diagrammes de moulabilité. Cette méthode permet d'obtenir le temps de remplissage optimal à une température du moule et une pression

d'injection de résine données à partir d'une seule simulation. L'utilisation de cet outil peut aider les industries à réduire le nombre de simulations et d'essais expérimentaux, minimisant ainsi les coûts de conception et le temps de cycle de muse en forme.

LIST OF TABLES

LIST OF FIGURES

ACKNOWLEDGEMENTS

My heartfelt thanks go to Prof. Pascal Hubert, my research supervisor, for the opportunities he offered, his steadfast support, and his insightful guidance. I am especially grateful for his unwavering belief in me through both the highs and lows of this journey. His dedication and professionalism have been truly inspiring, and I will strive to follow his example.

I would like to extend my sincere gratitude to the National Research Council Canada in Boucherville, especially to Dr. Loleï Khoun for being a role model and for her unwavering support in providing expertise and guidance with composite manufacturing processes and material characterization. I am very thankful to Nicolas Milliken for his indispensable guidance and support in composite design, simulation, and experimental part fabrication. Special thanks to Paul Trudeau for his valuable advice throughout the course of my PhD studies. Furthermore, I would like to express my appreciation to all the industrial partners for their contributions, which helped me consider the real-world applications of this technology.

Special thanks to Dr. Arnaud Dereims from ESI Group for teaching me PAM-RTM software and providing valuable technical advice and support in finite element analysis and performing liquid moulding simulations.

I must acknowledge Professors Andrew Hrymak and Jeffrey Wood for the opportunity to join the NSERC CREATE program at Western University's International Composite Research Centre (ICRC). Further acknowledgement goes to the Deutsche Forschungsgemeinschaft (DFG, German Research Foundation), project number 255730231, for providing additional funding during my stay at McGill University.

I am extremely grateful to all the members of the Structures and Composite Materials Laboratory. Many thanks go to my colleague and friend Leonardo Barcenas for years of close collaboration about fast curing resins and offering invaluable advice on process simulation for my PhD work. I would like to thank my summer intern undergraduate student Tony Jie for writing the LabVIEW code for the DAQ system and conducting permeability measurements. Special thanks to David-Michael Phillips for designing the through-thickness permeability measuring equipment. I would

like to acknowledge Fernanda Blanc for writing the optimization code and teaching me to code efficiently. I would also like to extend my thanks to our Research Assistant, Lucie Riffard, for providing the necessary training on handling laboratory equipment. Special mention goes to my best friend and colleague, Julieta Barroeta Robles for all the support and advice during my entire time as a PhD student.

I must thank the financial support of the Natural Sciences and Engineering Research Council of Canada (NSERC), the Research Centre for High Performance Polymer and Composite Systems (CREPEC), PRIMA Quebec, Texonic, and INDexpert.

I sincerely appreciate the advisory and evaluation committee members for agreeing to review the thesis, and for their invaluable input and time.

Finally, I want to thank my parents, Prof. Badiadka Narayana and Prof. Balladka Kunhanna Sarojini, for all the sacrifices they have made over the years and being my source of inspiration. I would like to extend my gratitude to my family friends, Dr. K.K Vijaya Raj and Dr. B.V Ashalatha, for looking after me when I arrived in Montreal. This PhD would not have been possible without the love and moral support of my three dogs, Genna, Bree, and Isabella. Lastly, I owe my success to the love of my life, my beautiful wife, Katie Komorek.

CONTRIBUTION TO ORIGINAL KNOWLEDGE

This work has led to several contributions resulting in a journal publication on highly reactive thermosets [1], and several conference papers on process modelling of the CRTM process [2], [3]. The contributions are highlighted as follows:

1) Characterizing highly reactive thermoset resins posed a significant challenge due to the capability of the characterization equipment (differential scanning calorimeter and rheometer). To tackle this problem, novel experimental methodologies were adapted for capturing the experimental data and fitting the cure kinetic and viscosity material models. The material models were used to enhance the predictability and processability of the fast curing resin in the manufacturing of composite materials. Furthermore, the implementation of these material models into existing commercial codes provided a valuable tool for optimizing processing and manufacturing parameters, thereby improving the efficiency of composite material production.
2) A significant contribution was made in the modelling of the CRTM process using the material models developed for fast curing resin. The modelling framework was fully coupled and was able to capture most of the processing steps: from placement of the preform to the demoulding of the final composite part, thereby significantly reducing the need for trial and error. Furthermore, the process model was extended to successfully manufacture a large scale demonstrator part using the fast curing resin, which demonstrated a practical application of this work.
3) Further contribution was made in the optimization of the CRTM process, by developing a tool to generate process maps based on a dimensionless characteristic number using Python. The optimization tool could predict resin injection times for a given resin injection pressure and mould temperature. Furthermore, the tool required data from just one simulation to generate a mouldability range, significantly reducing the overall computational costs required to run multiple simulations.

CONTRIBUTION OF THE AUTHOR

The entire work presented in this thesis was performed by the author, except for the following:

CHAPTER 3

Leonardo Barcenas conducted Differential Scanning Calorimeter (DSC) tests on Airstone, Hexion, Gurit Standard and Gurit fast resin systems and developed cure kinetic models. Rheology tests on Airstone and Hexion resin systems were performed by Dr. Loleï Khoun at National Research Council Canada (NRC) facility at Boucherville. DSC and rheological measurements on AOC resin system was performed by Lucie Riffard at McGill Structures and Composite Materials Laboratory. Permeability measurements were performed by Tony Jie as a part of his undergraduate research project (SURE) within the department of mechanical engineering.

CHAPTER 4 & 5

The composite parts for validating the simulation results were performed by Dr. Loleï Khoun and Nicolas Milliken from NRC Canada at Boucherville facility.

CHAPTER 6

The main part of the optimization code for generating the process map was written by Fernanda Blanc.

CHAPTER 1

1. Introduction

1.1 Background

In the landscape of manufacturing, fibre reinforced composites are being increasingly used in the aerospace, ground transportation, and marine industries. According to the Global Fuel Economy Initiative (GFEI) [4], a 65% reduction in CO_2 emissions is required by 2050 for all means of road transportation to comply with the Paris agreement. Particularly in the ground transportation industry, original equipment manufacturers (OEMs) are moving extensively towards composite solutions for structural lightweighting to increase the fuel efficiency of vehicles [5]. Furthermore, the last decade has seen a shift in OEMs towards manufacturing hybrid and electric vehicles to improve mileage and battery range. For example, a reduction of 5-8 % of fuel consumption is possible with a reduction of 10% in vehicle weight [6].

Composite materials are widely used due to their rigidity and high specific strength. The main barriers hindering the advancement of composite materials in vehicles are the fibre cost and long production cycle time [7]. A four axes chart was defined considering the production cost, production volume, sustainability, and process cycle time comparing the current manufacturing region to the targeted manufacturing region as shown in Figure 1. For example, the current advanced composite manufacturing processes fail to meet the target cycle time for high volume production (5-10 minutes for ground transportation) [8]. Therefore, it is extremely important to develop a fast and cost-effective composite processing technique to benefit from the performance of these materials [5]. Numerous processes are currently available for the manufacturing of composite parts: autoclave manufacturing, automated fibre placement (AFP), wet layup, liquid composite moulding (LCM), sheet moulding compound (SMC) and pultrusion [9]. To meet the requirements of the ground transportation industry, manufacturing processes need to be fast, versatile, and economical. The manufacturing technology that has the potential to satisfy these

requirements is resin transfer moulding (RTM), a branch of the LCM process [10]. It is the most widely used process among all the LCM processes due to its ability to produce near net-shape parts efficiently and cost-effectively [11]. The RTM process involves the injection of a liquid resin into a stationary, dry reinforcement placed inside a two-sided rigid mould [12]. However, RTM is a relatively slow process. Therefore, over the past two decades, researchers have been working on the variants of the RTM process. The two significant variants are High-Pressure RTM (HPRTM) and Compression RTM (CRTM). Baskaran et al. [13] manufactured an automotive roof using RTM, HPRTM and CRTM process and compared the process parameters. Figure 1-2 shows a comparison of the cycle time, clamping force, and injection pressure used to create the same part. The CRTM process outperformed the RTM and HPRTM processes significantly. Furthermore, life-cycle analysis of a car hood manufactured using the same three processes showed that the CRTM process had the lowest Cumulative Energy Demand (CED) [14].

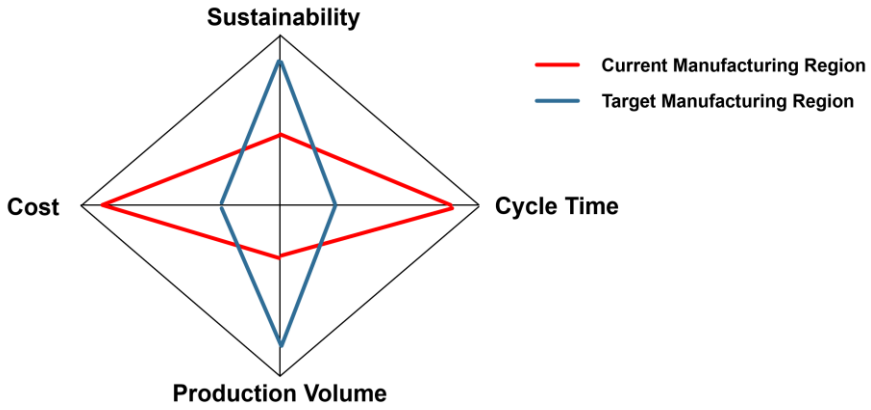

Figure 1-1: Comparison between the current manufacturing and targeted manufacturing regions based on the production cost, volume, cycle time and sustainability.

In recent years, material suppliers have come up with innovative thermoset resins that are fast curing in nature [15]. This has further aided the manufacturers the possibility of reducing the process cycle time and subsequently lowering the manufacturing costs [16]. The versatile and

economic nature of the CRTM process has a strong potential to introduce the fast curing resins at the production level.

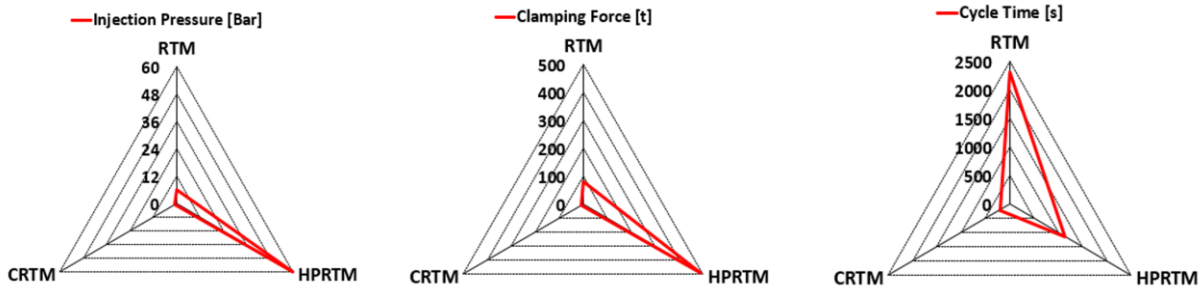

Figure 1-2: Comparison of process parameters for the RTM, CRTM and HPRTM process for the manufacturing of an automotive roof [13].

The CRTM process is as shown in Figure 1-3. Here, we mention two types of the CRTM process as defined by Bickerton et al. [17]. The CRTM process involves the following steps: (i) the preform is placed inside a preheated mould, (ii) the closure of the top mould with a small air gap, (iii) injection of resin into the mould either from the top directly into the gap or from the bottom, (iv) closure of the mould until the final thickness of the part, (v) allow the resin to cure for a desired amount of time, and (vi) finally open the top mould to demould the part. In CRTM-1, the injection of resin into the air gap facilitates faster filling of the resin through the surface followed by the compression sequence forcing the resin to travel shorter distance (through-thickness direction) with reduced flow resistance, thereby ensuring complete infiltration and lowering the injection time significantly. The CRTM-2 configuration is used when it is more feasible to access the mould from the bottom, due to the layout of the manufacturing environment. Furthermore, this setup allows better control of the flow front during the injection stage, reducing the risk of void formation due to air entrapment.

The main physical and chemical phenomena that take place during the CRTM process are heat transfer, cure, resin flow, compaction and residual stress development [18]. Figure 1-4 shows several key material properties and their interactions that take place during composite manufacturing. All these effects must be thoroughly studied to examine the entire process. Hence,

researchers have widely used process modelling to study the various complex phenomena that happen during the entire manufacturing process. The process modelling of CRTM can be subdivided into three main sub-models: heat transfer and resin cure kinetics, resin flow and compaction, and residual stresses [19]. The sub-models can be solved individually and the output from one sub-model can serve as an input for the subsequent sub-model. One of the major challenges involved in this method is the ability to reproduce the manufacturing cycle using numerical simulation. A comprehensive understanding of the intrinsic and extrinsic mechanisms that affect the process is necessary to accurately predict the final part quality.

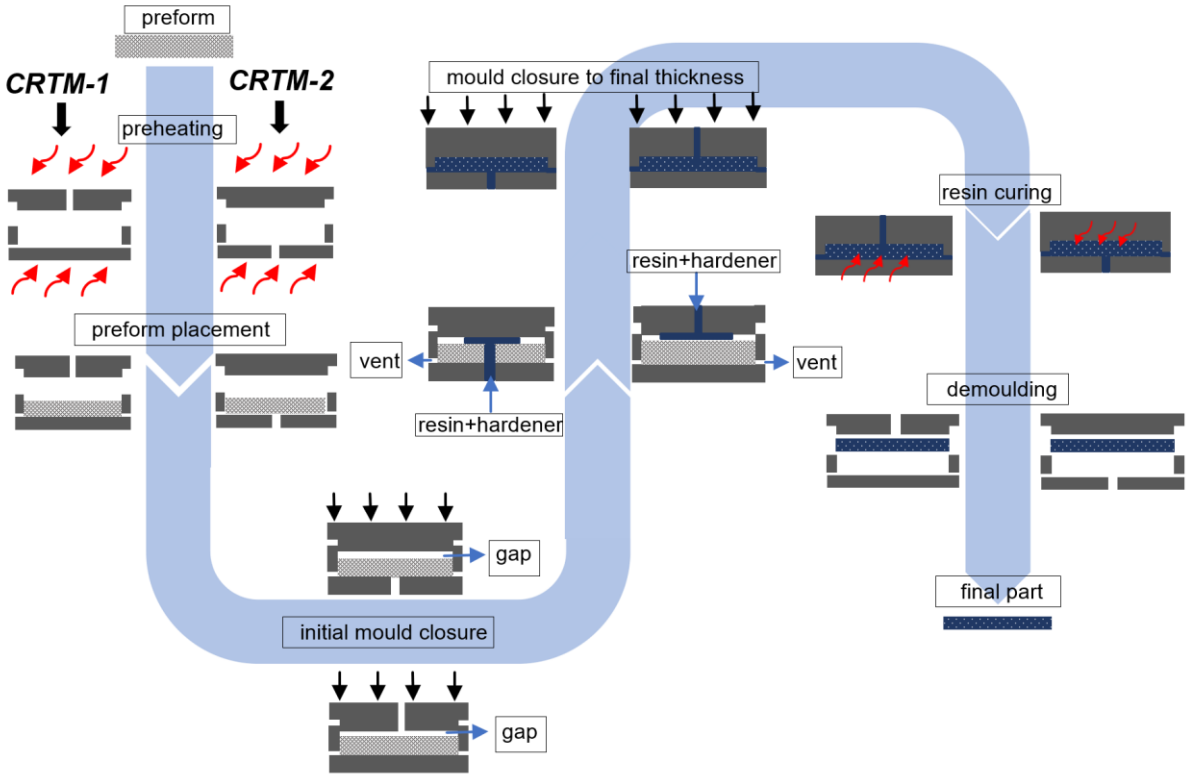

Figure 1-3: Two types of CRTM process are shown here: (i) CRTM-1, where the resin and hardener mixture are directly injected into the gap, and (ii) CRTM-2, where the resin and hardener mixture are directly injected into the preform.

The simulation approach for the CRTM process mainly consists of two stages. The first stage involves the mould filling step, while the second stage addressed the mould compression step. The simulations focus on the prediction of the resin flow front location, mould fill time, void content, pressure, temperature, and degree-of-cure progression [17–27]. The simulations also focus on the optimization of process parameters such as injection pressure, initial resin and mould temperatures, and finding ideal injection/vent locations [31-32]. Earlier simulations used only isothermal conditions for the mould filling and compression steps. The heat transfer and cure simulations were performed only after the onset of compression step. However, this approach does not hold true in the case of fast curing thermoset resins. The resin begins to cure as soon as it enters the heated mould. This causes a significant cure gradient at the end of the mould compression step. Figure 1-5 shows a comparison of the different stages of the CRTM process with respect to process cycle time between slow/medium curing and fast curing resins.

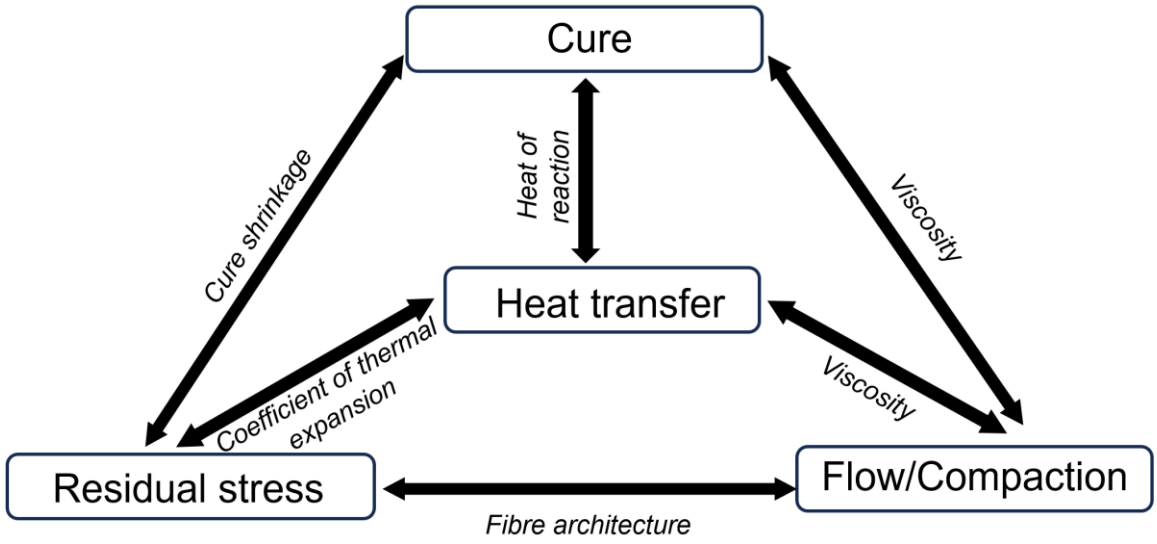

Figure 1-4: The CRTM phenomena interactions. Adapted from [33] with permission.

1.2 Motivation

To bridge the hurdle of fibre costs and increased production cycle times, it is imperative to choose an ideal composite processing technique that balances production speed, cost-effectiveness, and

sustainability. In this context, the CRTM process has emerged as a promising candidate. The process, aided with the potential of fast curing thermoset resins, has a huge capability of reducing the process cycle time, and in turn, manufacturing costs. However, the path to realizing the potential of the CRTM process lies in a comprehensive understanding of the intricate physical and chemical phenomena associated with the process. Through process modelling, we aim to study the key mechanisms at play, from heat transfer and resin cure kinetics to resin flow and compaction. Although process modelling has been well established to study the CRTM process, most studies revolve around the isothermal process [11], [24]. Moreover, there are insufficient data on the use of fast curing resins in an industrial environment for producing parts for ground transportation. Additionally, the highly reactive nature of the resins poses manufacturing and quality hurdles for moulded components, impacting aspects like part design and tooling.

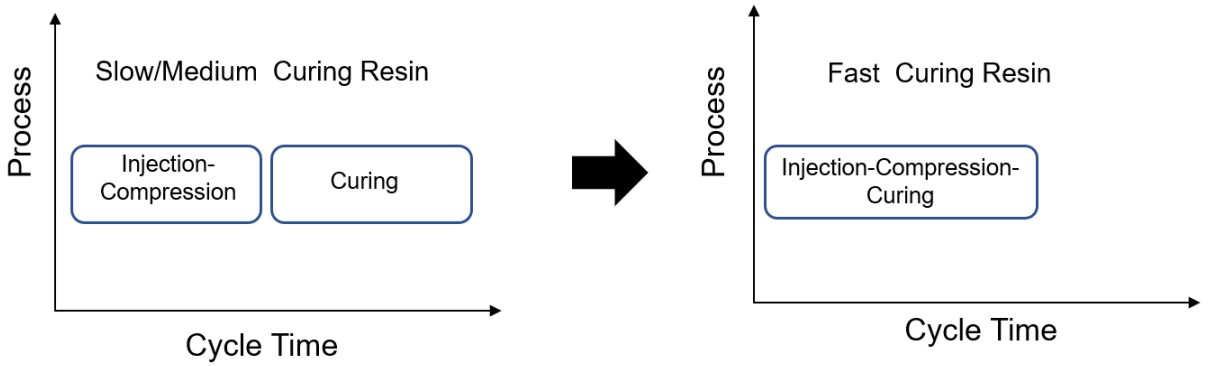

Figure 1-5: A plot of different stages of the CRTM process vs the cycle time showing the difference in the modelling approach for slow/medium curing resin and fast curing resin.

The last three decades have seen the development of numerous state-of-the-art tools to simulate the RTM process. However, only a few of the tools have shown the ability to simulate the CRTM process [34-35]. Moreover, the current simulation strategies exclude the mould geometry to increase the overall computational efficiency. As a result, the heat transfer between the mould and preform and their surroundings are not accurately captured. On the other hand, fewer studies have

been performed to simulate and validate the entire CRTM process: preheating, injection-compression, and curing.

This research could benefit ground transportation by using new advanced materials and advanced manufacturing methods. The key to achieving this purpose is by harnessing the potential of fast curing resins in the CRTM process. This way, we not only increase the efficiency of the process but also promote the cause of a more sustainable and environmentally friendly transportation landscape.

1.3 Thesis outline

The primary goal of the research project is to model the CRTM process with fully coupled heat transfer, resin flow, resin cure and compaction using fast curing resins. This will be accomplished by implementing resin and fibre material models into a commercial code. To achieve this goal, the present research is organized into the following chapters:

Chapter 2 presents a detailed literature review on the development of material models of resins and fibres required to model the CRTM process. Additionally, this section will present a detailed review of the existing process models and the simulation tools available for the CRTM process.
Chapter 3 presents a detailed information on the characterization and material model development of fast curing resins and glass non crimp fibre (NCF).
Chapter 4 investigates numerical and experimental setup of the CRTM process.
Chapter 5 examines the application of the simulation results to manufacture a complex net shape 3D ground transportation demonstrator part.
Chapter 6 discusses the sensitivity analysis of important process parameters involved in the CRTM process and development of an optimization tool to generate process maps.
Finally, Chapter 7 concludes with the recommendations derived from the work.

CHAPTER 2

2. Literature Review

This chapter gives a comprehensive scientific review on the material behaviour of the fast curing resins and fibres. In addition, it offers an in-depth analysis of the existing literature pertaining to the CRTM process. The review covers basic principles and recent progresses, addressing the gaps and potential solutions.

2.1 Material behaviour

2.1.1 Resin behaviour

The processing of composite materials involves the crosslinking of a low molecular weight thermoset material into a macromolecular solid stable structure. The monomeric reactant of thermoset resin requires chemical reactions to form a crosslinked structure. To form this crosslinked structure, a tailor-made hardener or a catalyst is typically used. The degree-of-cure or degree of conversion is used to describe the extent of crosslinking in a thermoset resin. A value of 0 corresponds to uncured state without crosslinking, whereas a value of 1 corresponds to a fully cured state with a densely crosslinked network. The next important resin behaviour that defines the processability of a composite material is viscosity. The addition of hardeners to the thermoset resin has a significant impact on the development of rheological properties [36]. Initially, the hardeners behave like solvents, reducing the intermolecular forces between the resin molecules. As a result, an initial drop in viscosity is observed. Eventually, the exothermic reaction between the resin and hardener leads to the formation of a crosslinked three-dimensional structure, thereby increasing the viscosity of the resin. The heat generated by the exothermic reaction further contributes to the increase in viscosity. As the crosslink density increases, the resin changes its behaviour from a liquid state to a rubbery gel state at a certain point in time. This point in the process is called gelation when the viscosity of the resin reaches an infinite value. Furthermore, the point at which the curing temperature exceeds the glass transition temperature is called vitrification, beyond which the resin attains a solid glassy state. During this stage, the progression

of the cure drops significantly. Figure 2-1 shows the different stages of phase transformation of the thermoset resin during the curing process.

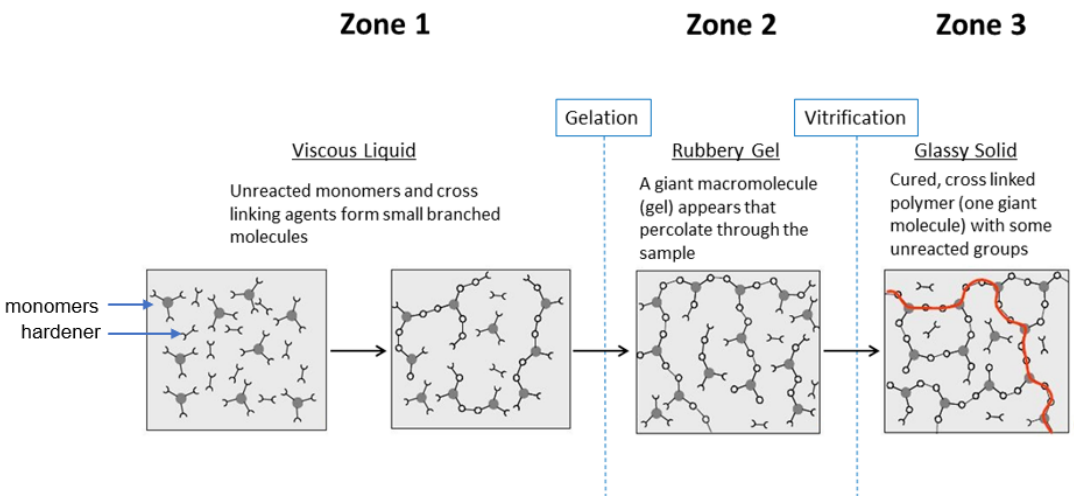

Figure 2-1: Stages of thermoset resin behaviour: Zone 1: monomer and hardener at its initial viscous liquid state forming small network; Zone 2: rubbery gel formation of the polymer due to cross linking; Zone 3: glassy solid formation due to rapid increase in crosslink density. Reproduced from [37] with permission.

2.1.1.1 Fast curing resins

Traditionally the aerospace, automotive, wind energy and marine industries have used slow curing thermoset resin systems to make fibre reinforced composite materials. In many cases, to fasten the production rate, high temperatures or energy is required to speed up the chemical reaction [38]. However, this can cause the degradation of the resin. The last decade has seen the researchers come up with fast curing thermoset resin systems as an energy saving and mass production tool [39]. These systems were designed to possess long pot life, low viscosity and high performance [40]. Amine-based hardeners were commonly used as accelerators for epoxy resins to achieve the fast curing effect for liquid composite moulding and applications requiring high mechanical performance [41-43]. Figure 2-2 shows the significant difference in the evolution of degree-of-cure and viscosity between a traditional slow curing RTM resin and a newly developed fast curing resin.

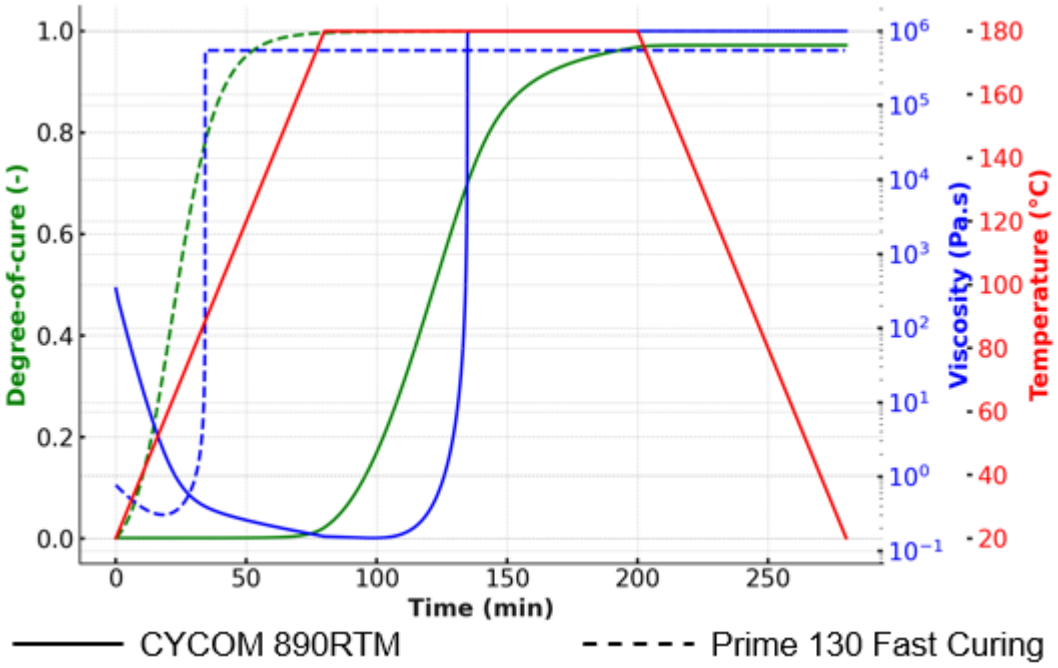

Figure 2-2: Evolution of degree-of-cure and viscosity of CYCOM 890RTM slow curing and Gurit standard fast curing resin from Gurit showing huge difference in time for the same cure cycle.

Infusing larger part requires longer times, which can become challenging while using a fast curing resin system. To overcome this Zhang et al. [44] developed the use of thermal latent curing agent for epoxy resins. These curing agents can cure faster than normal curing after reaching a threshold temperature. This provides the ability to infuse the fibres at lower temperatures and cure faster once the infusion is complete. Many thermoset resins are available to be used for the CRTM process. A general overview of the resins and their ability to be mass produced as a composite part are shown in Figure 2-3. Epoxies have been traditionally used in manufacturing industries for making composites due its excellent mechanical properties [45]. However, long cycle times have prevented them from being suitable for mass production. Similarly, polyimides and polyesters have long cure times making it not suitable for mass production. However, recent advances in chemistry have led to the use of new class of polyester and epoxy - dicyclopentadiene (DCPD) polyester and fast curing epoxy (high performance) respectively. This is due to the addition of hardeners or curing agents which drastically improve the cross-linking reaction making the resins to cure within minutes. This property makes them ideal candidates for mass production.

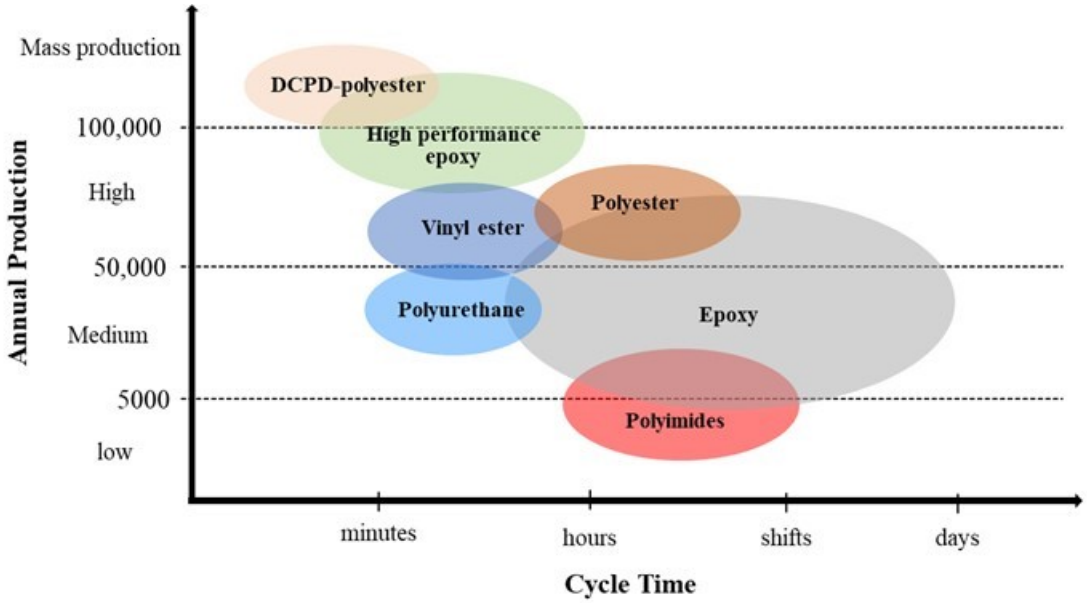

Figure 2-3: A map of thermoset resin categories with the time required and their ability for producing composite parts. [1] .

2.1.1.2 Resin cure kinetics

Two different approaches can be used to model the cure kinetics of a thermoset resin: mechanistic models (non-empirical) and phenomenological models (empirical or semi-empirical). Mechanistic kinetic models describe the underlying chemical reaction mechanisms of the curing process. These models have the capability to distinctively examine the impact of factors like concentration, or the number of initiators on the overall cure rate [46]. These resins undergo chain growth polymerization, and complete reactions which take place during the curing reaction (initiation, propagation and termination) is considered [47]. Several partial differential equations (PDE) are involved to evaluate the curing degree as each step in the chain growth polymerization is defined by a PDE. In contrast, the phenomenological models are simpler compared to mechanistic models and describe the curing process with one reaction typically by an ordinary differential equation (ODE) [48].

From an engineering perspective, phenomenological models are advantageous compared to mechanistic models since the models usually require limited number of parameters. However, mechanistic models require large number of parameters that require experimental data fitting or numerical optimization schemes [49]. Recently, machine learning techniques have also been employed to capture the cure kinetic behaviour of the resin [50-51]. However, while developing a coupled process model for a complex process like the CRTM process, having fewer equations reduces the overall difficulty of the process model. Therefore, this review focuses on phenomenological models.

Heat flow measurements from differential scanning calorimetry (DSC) under dynamic and isothermal conditions are used to develop the phenomenological cure kinetic models. Based on the DSC data, semi-empirical models of resin cure kinetics consisting of cure rate ($d\alpha/dt$) as a function of time, temperature and degree-of-cure were fitted to form a correlation [52]. The rate of heat flow (dH/dt) was assumed to be proportional to the cure rate based on the equation:

$$\frac{d\alpha}{dt} = \frac{1}{H_T}\frac{dH}{dt} \qquad \text{Eq. 2-1}$$

where H_T is the total heat of reaction (exothermic) (J/g). The degree-of-cure (α) was then obtained by the integrating area under the curve of cure rate versus time as:

$$\alpha = \frac{1}{H_T}\int_0^t \frac{dH}{dt}\,dt \qquad \text{Eq. 2-2}$$

Lee et al. [53] developed a simple cure kinetic model for a relating cure rate to degree-of-cure for a mono-reactive autocatalytic reaction for a polyester resin system:

$$\frac{d\alpha}{dt} = K\alpha^m(1-\alpha)^n \qquad \text{Eq. 2-3}$$

where m and n are catalytic constants determined empirically. K is the rate constant which follows an Arrhenius dependency:

$$K = A\ exp\left(\frac{-E_a}{RT}\right)$$ Eq. 2-4

here A is the Arrhenius constant (1/s), E_a is the activation energy (J/mol), R is the universal gas constant (J/kg.mol), and $T$is the temperature (K). However, these reactions do not include the effect of glass transition on the curing behaviour. The reaction slows down from kinetic dominated to diffusion dominated once the resin undergoes glass transition. In order to include the effect of vitrification in the cure kinetic equation Khanna and Chanda [54] introduced a diffusion factor $f(\alpha)$ which was modified by Cole et al. [55] as:

$$f(\alpha) = \frac{1}{1 + exp\ [C(\alpha - (\alpha_{C0} + \alpha_{CT}T))]}$$ Eq. 2-5

where C is the diffusion constant, α_{C0} is the critical degree-of-cure at absolute zero temperature and α_{CT} is the constant that replicates the increase in critical resin degree-of-cure with temperature. Hubert et al. [56] included the modifications from Cole et al. [55] and defined a bi- reactive cure kinetic model for an epoxy resin:

$$\frac{d\alpha}{dt} = \frac{(K_1 + K_2\alpha^m)(1-\alpha)^n}{1 + exp\ [C(\alpha - (\alpha_{C0} + \alpha_{CT}T))]}$$ Eq. 2-6

where the rate constant was defined similar to Eq. 2-4:

$$K_i = A_i\ exp\left(\frac{-E_{ai}}{RT}\right) \quad , where\ i = 1,2, \ldots$$ Eq. 2-7

The entirety of the curing process including vitrification was captured with a good fit using Eq. 2.6. However, Eq. 2.6 only includes two rate constants. The equation does not capture multiple autocatalytic reactions. Moreover, the current resin manufacturers use accelerators and inhibitors based on the processing requirements demanded by the industries. These effects are not captured by the equations mentioned so far. To include the effects of inhibitors and glass transition temperature, Ruiz et al. [57] proposed a model which was extended from the model developed by Bailleul et al. [58] for a polyester resin:

$$\frac{d\alpha}{dt} = K_1(T).K_2(\alpha).K_3(\alpha,T).K_4(I_d) \quad \text{Eq. 2-8}$$

$$K_1(T) = A\ exp\left[-E_a\left(\frac{T_{ref}}{T} - 1\right)\right] \quad \text{Eq. 2-9}$$

$$K_2(\alpha) = \sum_{i=0}^{s} a_i \alpha^i \quad \text{Eq. 2-10}$$

$$K_3(T,\alpha) = (\alpha_{max} - \alpha)^n; \qquad n = f(T) \quad \text{Eq. 2-11}$$

The term $K_1(T)$ is the Arrhenius term with a reference temperature of T_{ref}, $K_2(\alpha)$ is derived from Bailleul's approach [58] by fitting a polynomial of degree s, $K_3(T,\alpha)$ relates glass transition temperature to the kinetic reaction (α_{max} is dependent on T_g) and $K_4(I_d)$ is a weight function which includes the effect of inhibitor. The inhibitor decomposition equation is given by:

$$I_d(T,t) = t_{ref} - \int_0^t exp\left(-C_{ind}.\left(\frac{T_{ref}}{T} - 1\right)\right).dt, \qquad K_4(I_d) = \begin{cases} = 0\ if\ I_d > 0 \\ = 1\ if\ I_d \leq 0 \end{cases} \quad \text{Eq. 2-12}$$

here t_{ref} is the reference time, $C_{ind}$is the induction time and T_{ref} is the induction reference temperature. These are fitting constants, and the Eq. 2.8 is set to value 1 when the induction time is zero, hence capturing the effect of inhibitor.

In summary, the equations mentioned in this section have the potential to capture the entire curing history of the fast curing thermoset resin systems.

2.1.1.3 Resin viscosity

The evolution of viscosity of a thermoset resin depends on multiple variables like temperature, degree-of-cure, or inhibitors. At the application of thermal energy, initially the viscosity of the resin decreases to a minimum value as shown in Figure 2-2. As the cross-linking reaction begins, the viscosity increases and at gel point, reaches an infinite value. Rheometer is used to measure

the viscosity of the resin. Typically, cone-plate or parallel-plate geometries have been used to measure the viscosity of thermoset resin, as these geometries provide a consistent gap across the sample area, offer precise control of sample deformation and shear stress, and allow for straightforward calculation of shear stress based on the plate dimensions and applied torque [59].

Like cure kinetic models, semi-empirical models have been used to describe the evolution of viscosity of the resin system. A simple Arrhenius relation of viscosity η (Pa.s) of a resin depending on temperature is given by [60]:

$$\eta = \eta_{ref}\left[\frac{E}{R}\left(\frac{1}{T_{ref}} - \frac{1}{T}\right)\right] \quad \text{Eq. 2-13}$$

where E is the activation energy (J/mol) and T_{ref} is the reference temperature (K). The viscosity of a thermoset resin is dependent on the degree-of-cure of the resin. Castro and Macosko [61] developed an Arrhenius relationship to link the complex viscosity of the thermoset resin with the degree-of-cure:

$$\eta = \eta_o\left(\frac{\alpha_{gel}}{\alpha_{gel} - \alpha}\right)^{A+B\alpha} \quad \text{Eq. 2-14}$$

here α_{gel} is the degree-of-cure of the resin at gel point and A, B are the fitting constants. To better capture the evolution of viscosity around the gel point, Robles [62] used the equation consisting of an additional Arrhenius term:

$$\eta = \eta_1 + \eta_2\left(\frac{\alpha_{gel}}{\alpha_{gel} - \alpha}\right)^{A+B\alpha+C\alpha^2} \quad \text{Eq. 2-15}$$

Like the cure kinetic models, the term η_1 and η_2 are represented by a generalized equation:

$$\eta_i = A_{\eta i} exp\left(\frac{E_{\eta i}}{RT}\right) \ , where \ \ i = 1, 2, \ldots \quad \text{Eq. 2-16}$$

Here $A_{\eta i}$ is the Arrhenius constant (Pa.s). Since the viscosity of the resins increase in an exponential manner, Arrhenius based models have been extensively used predict the evolution of viscosity for fast curing resins [41], [61-63].

2.1.1.4 Glass transition temperature

Despite few kinetic models including the effect of glass transition temperature (T_g), it is a very important parameter which needs to be considered while modelling a thermoset resin. Vitrification occurs when the operating temperature approaches T_g . However, this can occur prior to the gel point, which can reduce the processing window available. To capture the evolution of T_g, DiBenedetto [66-67] used a model describing the relationship with α:

$$\frac{T_g - T_{g0}}{T_{g\infty} - T_{g0}} = \frac{\lambda\alpha}{1-(1-\lambda)\alpha} \qquad \text{Eq. 2-17}$$

where T_g is the current glass transition temperature (K) , T_{g0} and $T_{g\infty}$ are uncured and fully cured glass transition temperatures (K), respectively and λ is a fitting parameter with a value in the range between 0 and 1. Modulated DSC (MDSC) has been used extensively to capture the T_g of a thermoset resin which is characterized by a sudden change in specific heat [68]. Thermo Mechanical Analysis (TMA) is another technique widely used to measure the T_g, as the thermoset resin undergoes a marked changed in the coefficient of thermal expansion during the glass transition.

2.1.2 Fibre reinforcement behaviour

Fibres in polymer matrix composites (PMCs) play an extensive role as the main load bearing component. They are characterized by high stiffness, high strength, low density, and low thermal expansion. The manufactured fibres have extremely small diameter ranging from 1-10 μm [69]. Due to handling difficulties, these fibres are always supplied in bundles or tows. The fibre reinforcement tows are further architectured to obtain weaves and yarns. The map in Figure 2-4 shows the different types of architectured fibres [70]. The most extensively used fibre material are carbon and glass. However, depending on the application, the fibre materials can also be composed

of aramid, polyethylene (PE) and ceramics. Recently, there has been a rise in the use of natural fibres like flax, banana, and jute to help with recyclability.

Different fibre architectures are designed for different manufacturing processes. For a dry fibre infusion process like CRTM, the designed fibre architecture is called preform. Manufacturing a preform involves precise cutting of the fabrics, stacking them into multiple layers followed by the application of binders between each layer to give dimensional stability [71]. From Figure 2-4, two class of preforms namely woven and non-crimp fabric (NCF) have been extensively used in the CRTM process. The weft and warp yarns of the fabric are interlaced with an engineered weave pattern for woven fabric preforms. However, with the structures becoming complex, woven fabrics are subjected to the formation of crimp and misalignments leading to the loss of structural integrity [72-74]. However, the NCFs are characterized by stitching up unidirectional fibre layers in the direction required for the application using thermoplastic stitching threads or chemical bonding [75]. NCFs are extensively used in cases of complex geometries as they produce minimal crimp. An example of a woven and an NCF are shown in Figure 2-5.

To model the CRTM process, two main properties of the preform need to be characterized: permeability and compaction. The next subsection provides literature review on the up-to-date characterization techniques and the material models available on the permeability and compaction of fibre reinforcement.

2.1.2.1 Permeability

Permeability is defined by the ease at which the resin can infiltrate and flow through the fibre. Good impregnation of resin leads to higher quality of the manufactured part. Therefore, permeability of a preform needs to be accurately characterized and modelled. To model the flow of resin through dry preform, Darcy's law has been widely used [77]:

$$\vec{v} = -\frac{\overline{\overline{K}}}{\eta}.\nabla P \qquad \text{Eq. 2-18}$$

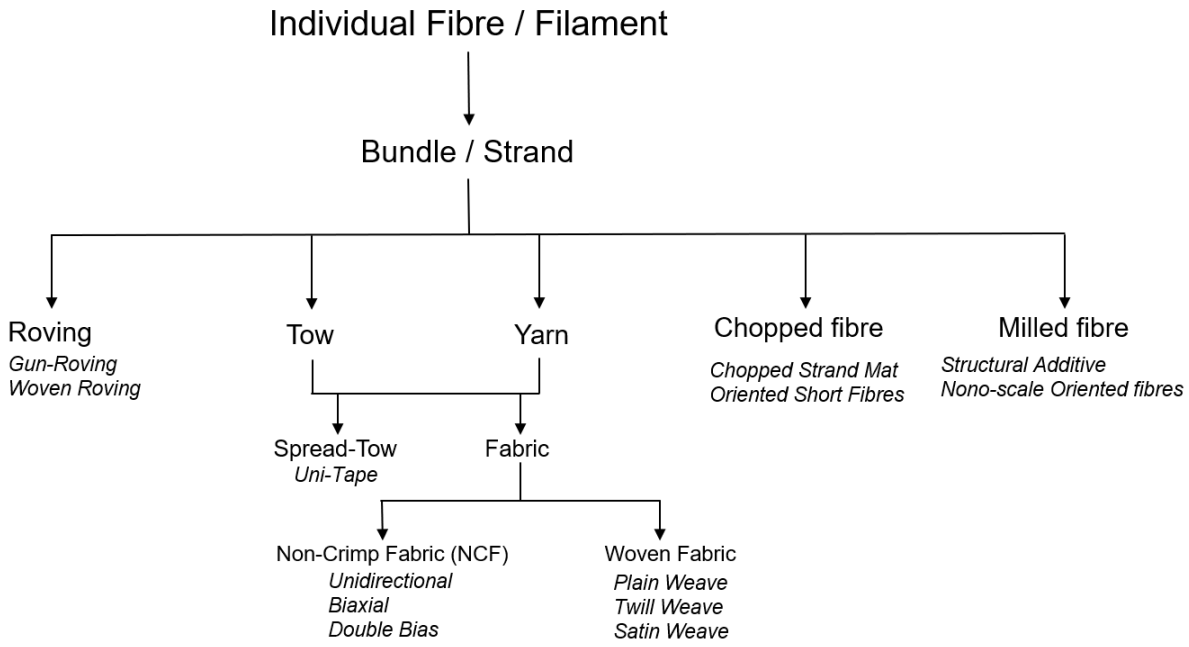

Figure 2-4: Map showing the different methods of combining fibres to form an architecture. Adapted from[70] with permission.

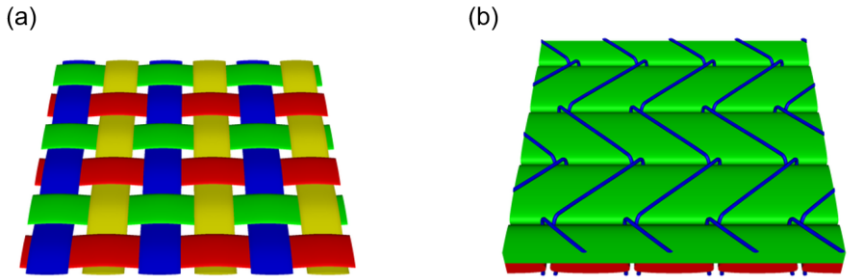

Figure 2-5: (a) Plain weave, and (b) bi-axial NCF produced using TexGen. Reproduced from [76] with permission.

where $\vec{v}$ is the phase averaged flow velocity (m/s), $\overline{\overline{K}}$ is the permeability (generally a second order tensor) (m^2), η is the resin viscosity (Pa.s) and ∇P is the resin pressure gradient (Pa). The permeability tensor consists of three main components, i.e., K_1, K_2 and K_3. For woven and NCF, there are two main permeability directions. K_1 and K_2 represent the in-plane or axial direction whereas K_3 represents out-of-plane or transverse direction.

In the last two decades, significant efforts have been undertaken to benchmark a standard procedure to measure the permeability in both in-plane and transverse directions [69–72]. Three types of experimental methods are considered to measure the permeability [78]: (i) flow geometry (linear/radial) , (ii) injection boundary condition (constant pressure/flow-rate) and (iii) saturation state of the preform (saturated or unsaturated). For a linear constant pressure unsaturated flow condition, a rectangular flow channel is used such that the fluid enters all the layers of the fabric at the same time. The flow front of the fluid is measured at a regular time interval until it's completely saturated. In this case, the following equation can be used to calculate the unsaturated permeability:

$$K = -\frac{x_{ff}^2 \phi \eta}{2\Delta p t_{ff}} \qquad \text{Eq. 2-19}$$

where x_{ff} is the flow front position (m) of the fluid at the corresponding time t_{ff}(s), Δp is the pressure gradient (injection pressure and outlet pressure), and ϕ is the porosity. Similarly, for a radial planar injection with constant pressure the equation can be modified as [79]:

$$K = \frac{R_o^2 \phi \eta}{4\Delta p t_{ff}} \left(\left(\frac{R_{ff}}{R_o} \right)^2 \left(2ln\left(\frac{R_{ff}}{R_o} \right) - 1 \right) + 1 \right) \qquad \text{Eq. 2-20}$$

Here R_o is the radius of the injection gate (m) and $R_{ff}$is the radius of the flow front (m) at time t_{ff}. Figure 2-6 shows the schematics of both the measurement techniques.

For saturated permeability, similar experimental setup can be used. Permeability can be calculated directly from the Darcy's law for unidirectional rectangular flow using:

$$K = -\frac{Q\eta L}{A\Delta p} \qquad \text{Eq. 2-21}$$

where Q is the volumetric flow rate (m^3/s), L is the length of the rectangular channel (m) and A is the flow channel cross sectional area (m^2). For an in-plane radial injection the Eq. 2-21 can be modified as [78]:

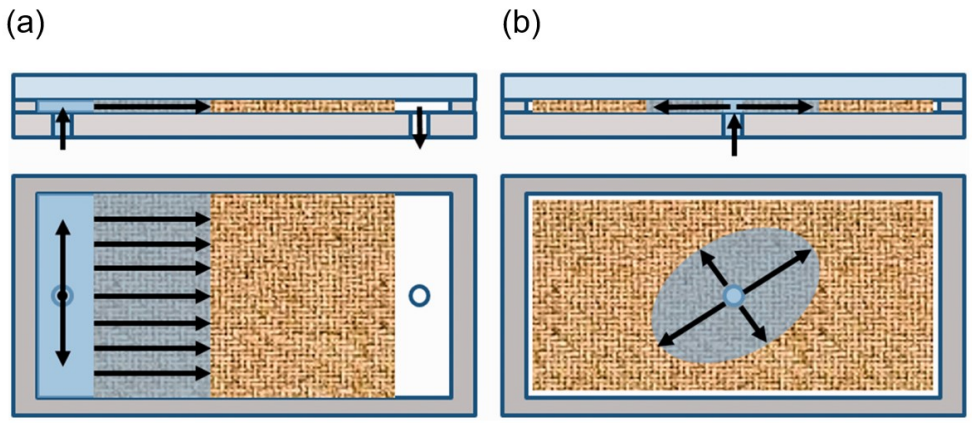

Figure 2-6: Schematics of unsaturated flow for the measurement of permeability: (a) unidirectional and (b) radial (right). Reproduced from [80] with permission**.**

$$K = -\frac{Q\eta}{2\pi h\Delta p} ln\left(\frac{R_{ff}}{R_o}\right) \qquad \text{Eq. 2-22}$$

where h is the thickness of the preform (m). Similarly, transverse permeability can be calculated for 1D unsaturated and saturated cases using Eq. 2-19 and 2-21 respectively. 3D unsaturated experiments can also be used to measure the transverse permeability. However, the set up used is complex and requires expensive ultrasonic sensor to measure the flow front [81]. The schematic of the transverse measurement technique for both 1D and 3D scenarios are shown in Figure 2-7.

The unsaturated permeability values are usually lower compared to the saturated permeability measurement due to capillary effects present on the fibre tows. However, for a process like CRTM, the high pressure experienced by the fluid during the compression sequence is far higher compared

to the capillary forces. Therefore, both measurement techniques can be used to calculate permeability.

Permeability is highly dependent on the architecture of the preforms. Therefore, developing material models can be challenging. To simplify this issue, permeability is generally described as a function of fibre volume fraction. Experimental data obtained for permeability at different fibre volume fractions can be used to develop simple semi-empirical models such as:

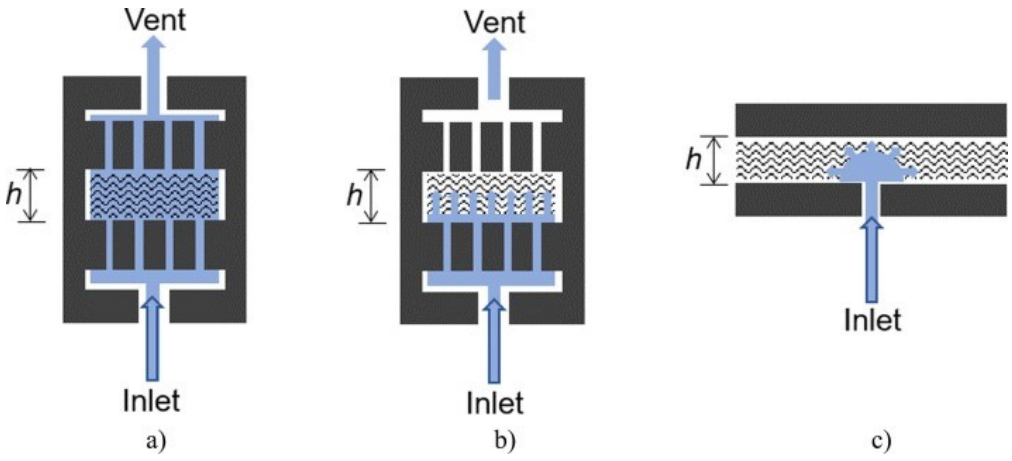

Figure 2-7: Schematics representing the transverse permeability measurement principle: (a) 1D saturated, (b) 1D unsaturated, and (c) 3D unsaturated. Reproduced from [82] with permission.

$$V_f = \mathrm{a}{V_f}^b \qquad \text{Eq. 2-23}$$

where a and b are the fitting constants. The volume fraction V_f is related to the porosity as:

$$V_f = 1 - \phi \qquad \text{Eq. 2-24}$$

One of the most extensively used equation for processes involving resin infusion is the modified Carman-Kozeny equation [83]:

$$K = c\frac{(1-V_f)^{n+1}}{V_f^n} \qquad \text{Eq. 2-25}$$

here c is the Carman-Kozeny constant (m^2). Both c and n are parameters determined from the experiment. This model is based on a homogenized geometry considering inter tow macroscale permeability. However, there exists an intra tow permeability which is not accounted for by this model. To account for the dual scale nature of the preforms, Nedanov and Advani [84] developed a two step approach to predict the permeability. The results obtained from this study showed that the intra tow permeability was two orders of magnitude lower than the inter tow permeability. Therefore, this effect has been excluded in material models. Though the models simplify the characterization process, their predictive accuracy is still heavily dependent on the experimental data [85-86] .

To reduce the number of experiments needed to characterize the permeability, significant efforts have been made in the recent years to calculate permeability virtually. Seuffert et al. [87] used micrographs from manufactured composite material to develop micro-scale model for computing permeability. For a more complex 3D structure, a combination of experimental and numerical approach was used to compute the permeability. Micro-CT (X-ray microtomography) was used to generate a 3D model representative of the entire architecture of the preform [88], [89]. Flow simulation was then performed to calculate the permeability of the preform. The procedure is illustrated in Figure 2-8 as described by Dei Sommi et al. [88]. However, the micrographs and micro-CT images do not exactly represent the entire preform structure and the values obtained would still need experimental validation. Recently, efforts have also been made to benchmark the Image based permeability measurement using the previously mentioned hybrid methodology [90]. The measurements were made on a 3D orthogonal carbon fibre with an interlacing z-binder. The results showed this approach had a good fit with the Kozeny-Carman equation and the experimental results proving the method's potential to reduce experiments in the future.

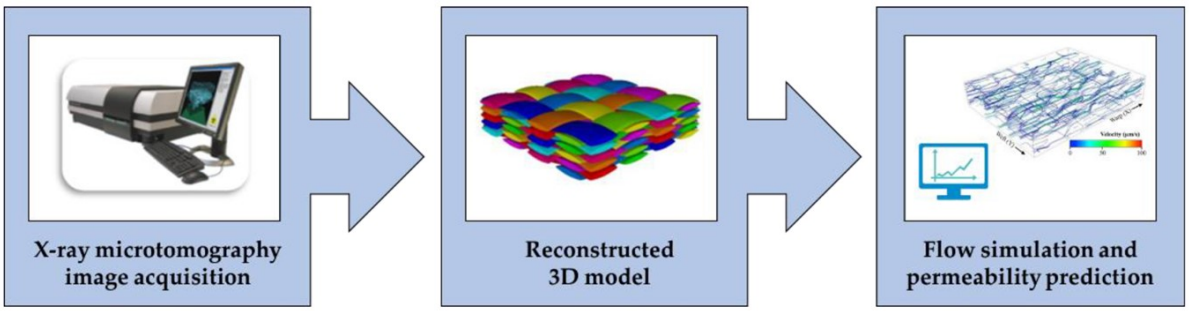

Figure 2-8: Procedure to obtain the permeability using a combination of experiment (micro-CT) and simulation [88].

2.1.2.2 Compaction

For a closed mould process like RTM and its variants, the preform is either compressed to a known cavity thickness prior to the injection of the resin or the preform is compressed to a certain thickness from an initial thickness post injection of the resin. The stresses experienced by the fibre bed is referred to as preform compaction. Since the thickness dictates permeability and volume fraction of the preform, characterizing and developing a material model for stress experienced by the preform as a function of volume fraction becomes important as it helps to define the necessary mould clamping force [91]. Gutowski et al. [92-93] defined an effective fibre bed stress $\bar{\sigma}$ (Pa) based on the experimental data obtained from running compaction tests using silicone oil. The compaction behaviour was due to fibre-fibre contact creating a wavy structure and was defined as:

$$\bar{\sigma}(V_f) = \frac{3\pi E_f}{\beta^4} \frac{\left(1 - \sqrt{\frac{V_f}{V_{f0}}}\right)}{\left(\sqrt{\frac{V_a}{V_{f0}}} - 1\right)^4} \qquad \text{Eq. 2-26}$$

where E_f is the flexural modulus (Pa) of the fibre, β is the ratio of arc length and arc height of the wavy fibres, V_a is the maximum fibre achievable volume fraction and V_{f0} is the initial

uncompressed fibre volume fraction. Typically to perform these tests, a universal testing machine is used, whose schematic is described in Figure 2-9. The fibre volume fraction and the compaction stress will be calculated from the force output, mass, and the sample geometry. Semi-empirical power models have been extensively used to model the compaction response [94-95]:

$$V_f = A' + B'\bar{\sigma}^{C'} \qquad \text{Eq. 2-27}$$

where A', B', and $C'$are the constants obtained from fitting the experimental data. For a process like the CRTM process, a portion of the preform can be wet before the onset on the compression. Therefore, compaction experiments need to be conducted at both dry and wet conditions. The following equation was used by Correia et al. [96] to consider both dry and wet conditions:

$$V_f = \frac{V_{f0}}{1-\epsilon} \qquad \epsilon = \begin{cases} a_{dry}\left(1 - e^{b_{dry}\bar{\sigma}}\right) & ,if\ fabric\ is\ dry \\ a_{wet} + b_{wet}\dfrac{\bar{\sigma}}{\bar{\sigma} + c_{wet}} & ,if\ fabric\ is\ wet \end{cases} \qquad \text{Eq. 2-28}$$

here ϵ is the engineering strain, and a_{dry}, b_{dry}, a_{wet}, b_{wet}, c_{wet} are the constants obtained from curve fitting. To capture the viscoelastic behaviour of the preform, Bickerton et al. [97] performed a set of dry and wet compaction tests and showed the stress relaxation behaviour of the preforms at constant volume fraction at the end of compaction. A generalized form of equation was developed by Bickerton and Kelly [98] to capture the viscoelastic nature of the preform:

$$\bar{\sigma} = \bar{\sigma}(V_f, \dot{V_f}) \qquad \text{Eq. 2-29}$$

here $\dot{V_f}$ indicates the dependence on the rate change of volume fraction which is a characteristic of a process like CRTM. The $\dot{V_f}$ term in Eq. 2-29 was replaced by compaction speed by Kelly [100] and the equation was rewritten as decomposition of the compaction stress as:

$$\bar{\sigma} = \bar{\sigma}\left(V_f, v\right) = f_\alpha(v).f_\beta(V_f) \qquad \text{Eq. 2-30}$$

where f_α, and f_β can be derived from the compaction responses for different compaction speeds as shown in Figure 2-10. Detailed explanations on the derivation can be found in the work by Kelly [100].

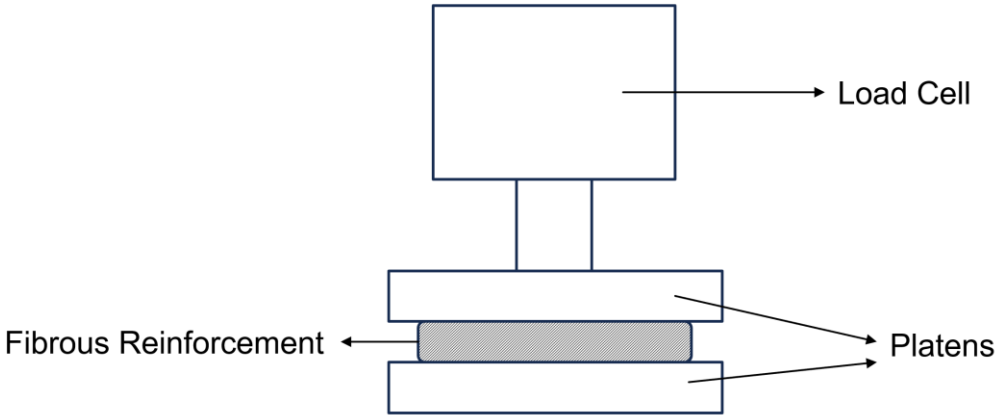

Figure 2-9: Schematic of a compaction testing jig showing fibrous reinforcement undergoing dry compaction. Adapted from [99] with permision.

$$\bar{\sigma} = \bar{\sigma}(V_f, \dot{V_f})$$

$$\bar{\sigma} = \bar{\sigma}\left(V_f, v\right) = f_\alpha(v).f_\beta(V_f)$$

Overall, in terms of tests carried out on compaction, there is still no industry standard available. Compared to the many benchmark studies carried out on permeability, only one benchmarking study has been conducted so far on compaction [101]. The coefficient of variation for the tests recorded showed a value ranging from 38-50 % which is very large. The results have shown the need to conduct more benchmarking exercise.

2.2 Compression resin transfer moulding models

Past three decades have seen significant number of researchers use process modelling to understand the CRTM process. The earliest work on the modelling of the CRTM process was conducted by Pham et al. [21] in which a 2D rectangular geometry was simulated. The upper part

of the mould displacement was introduced as a source term on the continuity equation based on Darcy's law as:

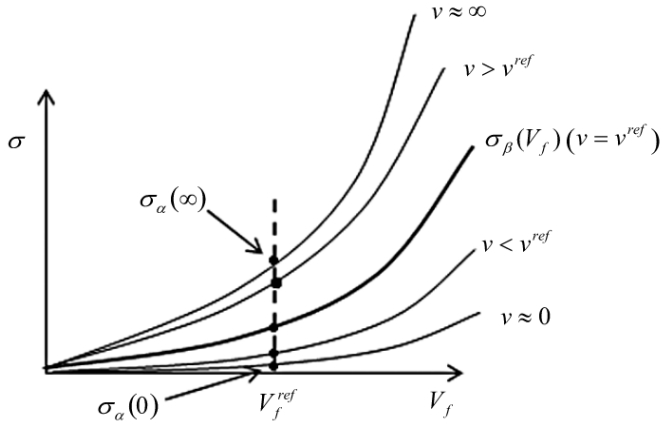

Figure 2-10: Compaction stress response at different compaction speeds [100].

$$\nabla \cdot \left(-\frac{K}{\eta}\nabla p\right) = -\frac{U}{h(t)} \qquad \text{Eq. 2-31}$$

where U is the upper mould closing velocity (m/s), and $h(t)$ is the preform thickness at time t. Finite element method (FEM) was used with non-conforming three node triangular elements. the model developed was validated with 1D analytical results with excellent agreement. The model however, only calculated resin pressure and did not include the reaction of the preform. Moreover, the model was limited to simple 2D structure. Pillai et al. [102-103] developed a 3D construction methodology for elements from a 2D shell mesh to replicate complex geometries. A finite element (FE) model was implemented to model the deformation of dry preforms and to simulate the gap between the mould and the preform. Shojaei [104] performed a 3D flow analysis of resin infiltration in CRTM process using Finite Element/Control Volume (FE/CV) method. Regular cubic and irregular hexahedral elements were used to include complex geometry and deformations. The study showed the effectiveness of the numerical simulation in predicting flow progression, pressure distribution, and mould clamping force during the CRTM process.

An in-depth analysis of the CRTM process was conducted at University of Delaware [12], [34] using a custom inhouse tool called Liquid Injection Moulding Simulation (LIMS). In this study, the process was divided into three steps: (i) resin injection into the gap between mould and preform, (ii) closure of the mould gap, and (iii) compression of preform to required thickness. FE/CV method was used for numerical simulation of resin flow. To simulate the gap, lubrication theory was applied with 2D shell elements. An automotive B-pillar was manufactured and using short-shot experiment, the simulation results were validated with reasonably good agreement. To improve the accuracy of the simulation, Merotte et al. [26] assumed the mould gap was entirely filled with the resin at the end of the injection phase and applied a pressure boundary on top of the preform as same as the compression force of the mould during the closure of the gap. The experimental results were in good agreement within the variability in permeability and compaction properties of the preform. At University of Auckland, significant work was carried out to capture the viscoelastic behaviour of the preform undergoing deformation during the compression sequence of the CRTM process [83], [98], [100], [105-106]. A Tekscan distributed pressure measurement system was used to compare experimental results on a circular mould mounted on a universal testing machine. The stress generated during the injection and compaction phases were compared with the numerical results with good agreement. Recently, Lee et al. [107-109] included hydrodynamic compaction effects for an entire series of transverse LCM process. The custom code built using python showed the gradient in volume fraction and stresses across the thickness because of hydrodynamic effects. To capture the interaction between the resin and the fibres, a different approach was proposed by Marquette et al. [110-111]. They developed a new fluid-solid coupled solver with a flexible data transfer between the fluid and solid mechanics solver, a latest feature of the tool PAM-RTM from ESI group. In this approach, the preform was considered as an equivalent orthotropic homogenous medium consisting of rigid fibres such that the strain at the macroscopic level was depicted at microscopic level through fibre rearrangements as shown in Figure 2-11. Therefore, this approach eliminates the requirement of using semi-empirical laws for preform compaction and showed that the porosity can be updated according to the following equation:

$$J(\vec{x}, t + \Delta t)\big(1 - \emptyset(\vec{x}, t + \Delta t)\big) = J(\vec{x}, t)(1 - \emptyset(\vec{x}, t)) \qquad \text{Eq. 2-32}$$

where $\vec{x}$ is the position vector, $\emptyset$ is the porosity of the fibre reinforcement and J is the Jacobian of the transformation. The coupling between the solid and fluid mechanics is done by Terzaghi's law [112]:

$$\bar{\bar{\sigma}}_{overall} = \bar{\bar{\sigma}}_f + P\bar{\bar{I}} \qquad \text{Eq. 2-33}$$

where $\bar{\bar{\sigma}}_{overall}$ is the overall stress exerted. $\bar{\bar{\sigma}}_f$ is the stress generated on the fibre, P is the hydrostatic resin pressure and $\bar{\bar{I}}$ is the unit tensor. Furthermore, an inter-penetrating mesh approach was also developed to capture the closing of the mould gap. Figure 2-12 shows the inter-penetrating mesh technology introduced along with the fluid-solid coupled solver. Dereims et al. [111] performed CRTM experiments on a truncated pyramid tool with a glass mould with high resolution cameras used to capture the flow front of the resin. Machine spindle oil was used to replicate the resin since its viscosity remains constant at room temperature and can replicate the infiltration behaviour of a thermosetting resin. The fluid-solid coupled approach showed good agreement between the simulation and experimental results.

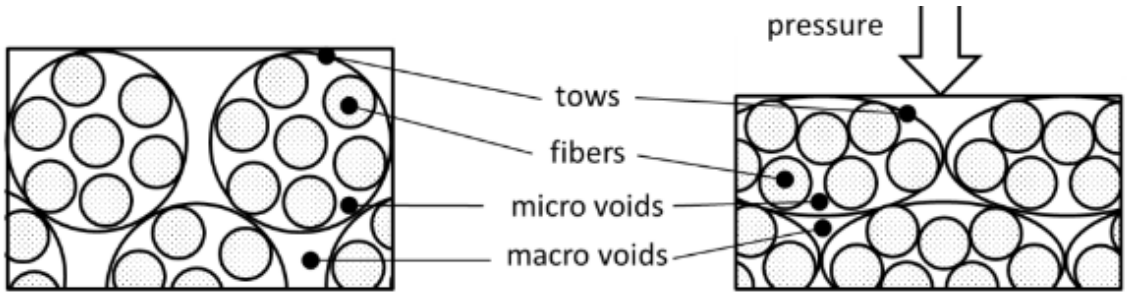

Figure 2-11: Fibre rearrangement post compression for unidirectional fibres. Reproduced from [113] with permission.

In LCM processes, modelling of heat transfer and cure has been extensively studied. However, most studies solve the mould filling process as an isothermal process and perform the heat transfer analysis post the complete filling of the resin (post compression for the CRTM process). With the recent development of fast curing resins, this assumption will not hold valid. Therefore, the process models need to consider the effects of heat transfer and cure right from the onset of injection of

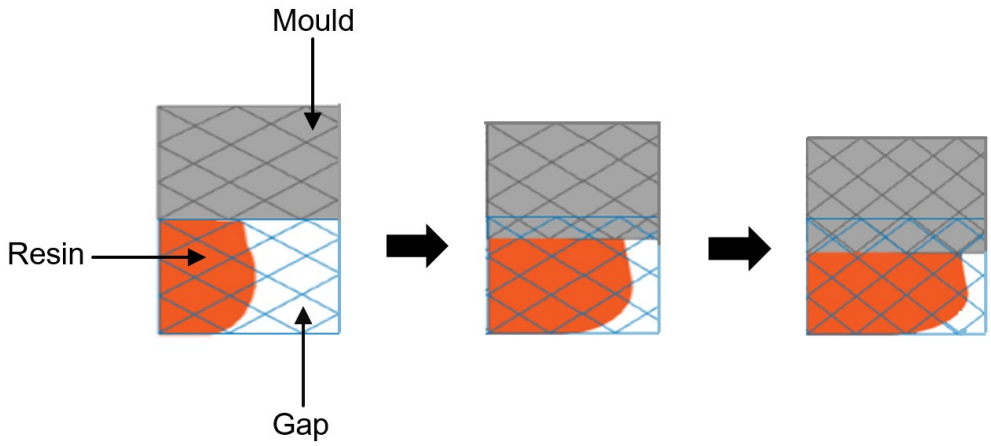

Figure 2-12: Inter-penetrating mesh method used in PAM-RTM showing the closure of the gap and pushing the resin (orange colour). Adapted from [35] with permission.

resin into the mould. Ruiz and Trochu [114] developed a Finite Element/Finite Difference (FE/FD) based numerical method to predict the non-isothermal mould filling in LCM processes. A local thermal equilibrium (LTE) was used to capture the energy transfer between the mould, resin and fibres. The approach used a lumped system were the temperature at any point between resin and fibres were considered same. The LTE equation for a transient temperature T was given as:

$$\rho_c C_{pc} \frac{\partial T}{\partial t} + \rho_r C_{pr} (\vec{v} \cdot \nabla T) = \nabla \cdot \left(\bar{\bar{k}} \nabla T\right) + \emptyset \rho_r H_{tot} \frac{\partial \alpha}{\partial t} \qquad \text{Eq. 2-34}$$

where ρ_c and ρ_r represent the composite and resin density respectively (kg/m^3), C_{pc} and C_{pr} are the heat capacity of composite and resin respectively (J/kg.K), T is the equilibrium temperature, H_{tot} is the total heat of reaction (J/g) and $\bar{\bar{k}}$ is the effective thermal conductivity tensor (W/m.K). The last term on the right-hand side of the equation takes into account the effect of the reaction kinetics of the resin The average material property was calculated using the following equations. Here *r* and *f* represent resin and fibre respectively:

$$\rho_c C_{pc} = \emptyset \rho_r C_{pr} + (1 - \emptyset) \rho_f C_{pf} \qquad \text{Eq. 2-35}$$

$$\frac{1}{k} = \frac{\emptyset}{k_r} + \frac{(1-\emptyset)}{k_f} \quad \text{Eq. 2-36}$$

To consider the transfer of cure gradient, chemical species transport equation (advection) equation was used:

$$\frac{\partial \alpha}{\partial t} + \vec{v} \cdot \nabla \alpha = R_\alpha \quad \text{Eq. 2-36}$$

here $R_\alpha = \frac{\partial \alpha}{\partial t}$ is the reaction rate. The equations presented in section 2.1.1.2 can be used to represent the reaction rate.

Very few studies have been conducted on the modelling of RTM and its variants using fast curing resins. Deleglise et al. [115] proposed a method to model high-speed RTM process with an online mixing of resin and hardener for a fast curing resin system. An automotive B-pillar was simulated, and short shorts experiment were conducted with good agreement. The resin cure kinetics and viscosity were implemented as a function of time based on the experimental results. Similar approach was used by Martin et al. [116] to simulate injection stage of the CRTM process with fast curing resin. In a different approach, Keller et al [28] developed a 2D multi-physics coupled model to simulate the CRTM process using COMSOL Multiphysics. Three injection strategies were considered: direct dosing, wet pressing, and gap injection. The simulations captured the development of exotherms of the fast curing resin which were then validated with the sensor readings for a simple flat plate structure.

2.2.1 Simulation tools review

Several commercial and open-source tools have been developed for LCM processes. However, only few tools are available that are particularly geared towards simulating a fully coupled CRTM simulation. LIMS developed by University of Delaware showed the capability to simulate 3D CRTM process with excellent validation using FE/CV method for tracking resin flow front [12], [34], [116]. Recently, they have expanded its capacity to run fully coupled model to include bubble transport and cure propagation [117]. University of Aukland also developed a tool to simulate the CRTM process called SimLCM which showed the ability to capture the viscoelastic behaviour of

the fibre during compression [118-119]. Additionally, the tool showed the ability to predict flow front using conforming (FE/CV) and non-conforming elements. Recently, PAM-RTM from ESI Group have developed a fluid-solid coupled solver particularly for the CRTM process with interpenetrating mesh technology to deal with the vanishing mould gap [110-111], [113]. This tool can capture the heat transfer and flow between the mould, preform and resin. Non-conforming triangular elements have been used to predict the resin flow front. A multipurpose state-of-the-art finite element tool, COMSOL Multiphysics has been used to model a fully coupled heat transfer and cure simulation of the CRTM process [28]. For tracking the flow front, either level set or phase field methods have been employed. Yang et al. [120] used ANSYS Fluent, another state-of-the-art package to solve 3D CRTM process using volume of fluid method. Open-source computational fluid dynamics (CFD) tool OpenFOAM has also been used to simulate the CRTM process using finite volume method [29-30].

2.2.2 Process optimization

Process optimization has been studied primarily to investigate the effects of process variables which govern the CRTM process. Chang et al. [121] investigated the effects of injection pressure, mould gap, resin temperature, compression pressure, pre-heated mould and cure temperature on the overall performance of the CRTM process. Experiments based on Taguchi's method and the L18 orthogonal array was conducted to look at the effect of process variables on the mechanical properties of the manufactured part. To tackle the issue of non-optimum processing setups, Achim and Ruiz [122] developed a software interface based on fuzzy logic to optimize the process and generated mouldability diagrams to help process engineers reduce process cycle time and cost. Figure 2-13 shows an example of the mouldability diagram for a non-isothermal RTM process. A surrogate model based game-theoretic approach was developed by Gupta et al. [31] to optimize non-isothermal CRTM processes. The framework used a bilevel multi-objective genetic algorithm (BMOGA) to generate optimized solutions for filling time and cure behaviour for a process engineer to choose from. Karger et al. [123] developed a continuous virtual process chain (the CAE chain) to transfer data between FE models using a neutral exchange format and mapping algorithms. The developed CAE chain was used to optimize the RTM process and manufacture a complex curved part.

Nondimensional analysis has also been used to investigate the effects of process variables on the CRTM process. Bhat et al. [34] derived five nondimensional numbers to investigate 1D through thickness flow in the CRTM process. With the help of these numbers, a parametric study was conducted to analyze the influence of these numbers on resin injection, gap closing and preform compaction and demonstrated how these nondimensional numbers simplified the complexity of

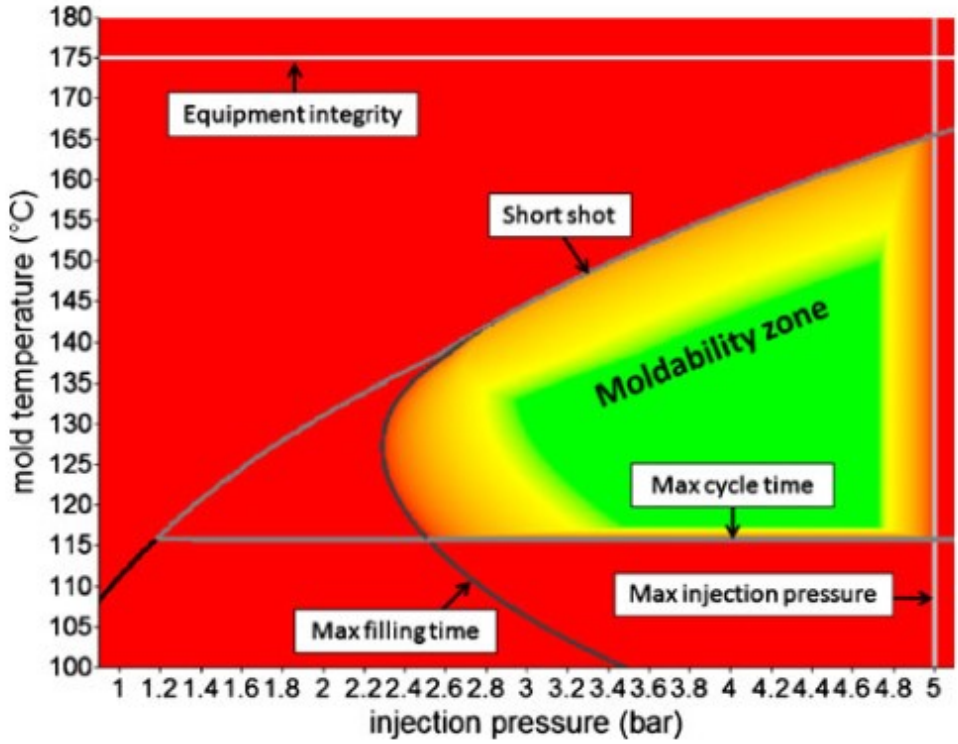

Figure 2-13: Mouldability diagram for a non-isothermal RTM process. Reproduced from [122] with permission.

the different coupling mechanisms in the CRTM process. Baskaran et al. [124] conducted parametric study on gap thickness and resin distribution using the ratio of gap permeability and

transverse permeability. Important conclusion from this study was that there is significant penetration of resin through the preform when it is injected into the mould gap. Recently, Di Fratta et al. [125-126] introduced a new dimensionless characteristic number called injectability number to assist composite fabrication. It is calculated by integrating the ratio of injection pressure and resin viscosity over the total injection time. The invariance of the number was tested on multiple cases involving different injection and moulding conditions with good validation for both RTM and CRTM cases.

2.3 Summary and research objectives

The CRTM process has been widely studied numerically and experimentally as presented in the previous section. The following conclusions can be drawn from the literature review:

1) There are only few papers available on the characterization and modelling of resin cure kinetics and viscosity of fast curing resins. Most of the work focuses on either resin chemistry or the mechanical properties of the manufactured part. Additionally, there is a notable lack of data regarding the application of fast curing resins in an industrial setting for parts manufactured in ground transportation.
2) Significant amount of work on the CRTM process are modelled as an isothermal process. However, the assumption does not hold true for fast curing resins. Moreover, many of these studies are limited to 2D or simple 3D geometries such as flat or angled structures.
3) Most simulation tools do not include the mould geometry to capture the compression sequence as a part of the simulation. The tool part interaction (heat transfer) is generally ignored for simplicity.
4) Many optimization techniques require extensive computation and experimentation which significantly raises the total cost of production.

Table 2-1 summarizes the important work conducted in the last two decades on the CRTM process. No single paper considered all the sub physics' (heat transfer, cure, flow and compaction) for the entire process from preform placement on the preheated mould until the demoulding of the part.

Table 2-1: Important references on the modelling of the CRTM process

Reference	Geometry	Resin/fluid type	Flow front tracking method	Experimental/Numerical		Simulation tool
				Isothermal	**Non-isothermal**	
Bhat et al. [34]	3D flat Structure	Constant viscosity fluid	FE/CV	Numerical		LIMS
Simacek et al. [12]	3D automotive B-pillar	slow curing resin	FE/CV	Experimental and numerical		LIMS
Kelly and Bickerton [118]	3D fireman's helmet	Constant viscosity fluid	FE/CV or Non-conforming elements	Numerical		LIMS
Keller et al. [28]	2D Simulation/3D flat structure experiment	Fast curing epoxy resin	Level set method		Experimental and numerical	COMSOL Multiphysics
Seuffert et al. [29]	3D floor panel	Constant viscosity fluid	Finite Volume Method	Numerical		OpenFOAM
Marquette et al. [35] and Dereims et al. [111]	3D truncated pyramid tool	Constant viscosity fluid (Machine spindle oil)	Non-conforming elements	Experimental and numerical		PAM-RTM

Therefore, the current thesis will investigate the CRTM process with fast curing thermoset resin with glass NCF. The following objectives were considered based on the literature review:

1) **Material characterization:** To measure the cure kinetics and viscosity of fast curing epoxy and polyester resin. To fit the experimental data into material models to be implemented in a simulation tool.

   Measure permeability and compaction of a glass NCF and fitting the experimental data to existing material models.
2) **Simulation and validation of the CRTM process:** Simulate a 3D flat plate structure using a commercial code PAM-RTM. Design experiments to validate the simulation at the lab scale.
3) **Manufacturing of a complex 3D demonstrator part:** Based on the data obtained from the manufacturing of a flat 3D part, simulate a complex seat base demonstrator part of a long-distance coach. Based on the simulation results, manufacture the part.
4) **CRTM process optimization:** Use of dimensionless characteristic number to generate process maps to help composite process and design engineers choose the optimal process variables.

CHAPTER 3

3. Characterization of Material Behaviour

The literature review showed the importance of material models in capturing the behaviour of the materials during the manufacturing process. The first part of the chapter involves the characterization and development of the material constitutive models of four epoxy resins and one polyester fast curing resin. The second part of the chapter focuses on the characterization and material model development of a glass non-crimp fibre (NCF).

3.1 Resin characterization: Epoxy resin

The important parameters during the infiltration of the preform are cure kinetics, viscosity and glass transition temperature. First, a thermogravimetric analyzer (TGA) was used to find the degradation temperature and thermal stability of the resins. A differential scanning calorimeter (DSC) was then used to determine the evolution of degree-of-cure as a function of temperature and time. Subsequently, a rheometer was used to measure the viscosity of the resin, which was described as a function of time, temperature, and degree-of-cure.

Based on the processability and reactivity of the resin, four different commercial resins were analyzed. All four resins studied in this work were two-part (one component resin and one component hardener) epoxies. These resins are generally characterized by a highly reactive epoxide group that opens and forms covalent bonds upon the addition of hardeners (curing agents). Three of the resins were fast curing in nature – one from Hexion and two from Gurit (Gurit standard and Gurit fast). The fourth resin, from Olin (Airstone), was a slower reactive resin compared to the rest of the three resins. This system was used as a reference resin system. The details and specifications of the resins are given in Table 3-1. The cure kinetics and viscosity characterization were divided between two research facilities, and hence two different instruments were used. At the National Research Council Canada (NRC), Hexion and Airstone resin systems were tested and the resins from Gurit were tested at the McGill Structures and Composite Materials Laboratory.

3.1.1 Thermal stability

The tests on the thermal stability were performed on a TGA Q500 from TA Instruments. The samples were ramped at a 20 ºC/min from room temperature (20 ºC) to 700 ºC under air condition. A weight percentage reduction of 5% was observed in the Airstone system between the range of processing temperatures of 100 ºC – 140 ºC. For the other resins, a reduction of less than 2% was observed over the same temperature range. This behaviour is typical of a thermoset resin due to the evaporation of volatiles and moisture present in the resins. The degradation temperature was higher than 300 ºC for all the resin systems. Therefore, all the characterization was performed below this temperature. Figure 3-1 shows the TGA results for all the epoxy resin systems.

Table 3-1: Epoxy thermoset resin specification

Resin		**Hardener**	**Mix ratio. Parts per weight**
Hexion	Epikote 50475	Epikure 05500	100:17
Airstone	780E	785H	100:31
Gurit Standard	Prime 130 SPX26528	Standard SPX26373	100:25
Gurit Fast	Prime 130 SPX26528	Fast SPX26180	100:27

3.1.2 Cure kinetics

3.1.2.1 Methodology

Two different pieces of equipment were used for the resin systems with different methodologies. The equipment at NRC was a modulated differential scanning calorimeter (MDSC) Q100 from TA instruments for the Hexion and Airstone resin systems. Dynamic scans were performed from 50 ºC to 250 ºC at a heating rate of 10 ºC/min. Isothermal tests were conducted at 80 ºC, 90 ºC, 100 ºC, and 110 ºC for both systems. For Gurit Standard and Gurit Fast resin systems, a second piece of equipment was used at McGill. It was a double-furnace DSC 8500 from Perkin Elmer and the dynamic scans were performed at a heating rate of 10 ºC/min under the same conditions from 50 ºC to 250 ºC. For Gurit Standard, isothermal scans were performed at 70 ºC, 80 ºC, 90 ºC. For Gurit Fast, isothermal scans were performed at 50 ºC, 60 ºC, 70 ºC, and 80 ºC. The tests at each temperature were repeated three times.

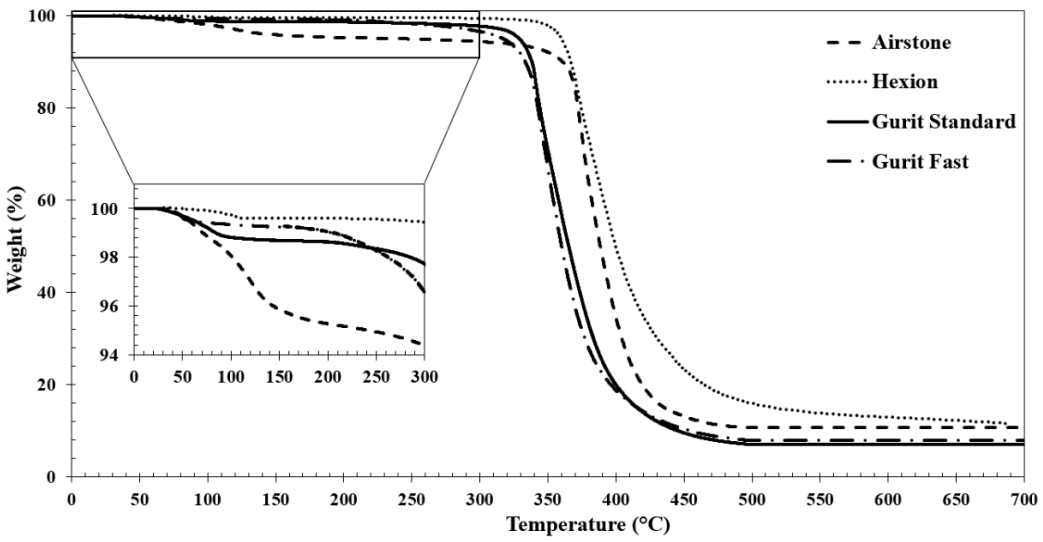

Figure 3-1: TGA analysis of the epoxy resin systems showing significant degradation beyond 300 ºC.

It was extremely difficult to characterize highly reactive thermosets at high temperatures (greater than 100 ºC). The methodology used on the Q100 DSC consisted of placing the pan with an uncured resin in the DSC cell at a given initial temperature. The following experimental steps were followed: opening of the cell, placement of the pan in the cell and closing of the cell. At this stage, the DSC started acquiring the data. However, due to the high reactivity of the resin, curing was initiated while the resin was placed inside the pan. The acquired data was not reliable as the initial reaction was not monitored. The rate of data loss increased with increasing temperature.

With the Perkin Elmer DSC, the pan was placed at room temperature. The cell was closed, and no reaction was expected at this stage. The cell was heated at the maximum capacity of the DSC to 300 ºC/min. With this method, the data were recorded at the beginning of the ramp and there was no loss of data. However, the acquired data during the ramp to reach isothermal temperature were not accurately measured. Moreover, the rapid increase in temperature (300 ºC/min) could result in thermal inertia or time lag due to the disparity between the furnace temperature and the sample temperature. This could lead to errors and uncertainty that increase with higher temperatures.

3.1.2.2 Modelling

The heat generated by the resin was measured and the results were converted into cure rate based on the assumption that the reaction rate, $d\alpha/dt$, is proportional to the heat flow rate, dH/dt:

$$\frac{d\alpha}{dt} = \frac{1}{H_T}\frac{dH}{dt} \qquad \text{Eq. 3-1}$$

where H_T is the total heat of reaction of the resin. The evolution of heat flow with respect to temperature is shown in Figure 3-2 for all four resin systems. The area under the curve normalized by the sample mass was calculated from the plot to obtain the total heat of reaction.

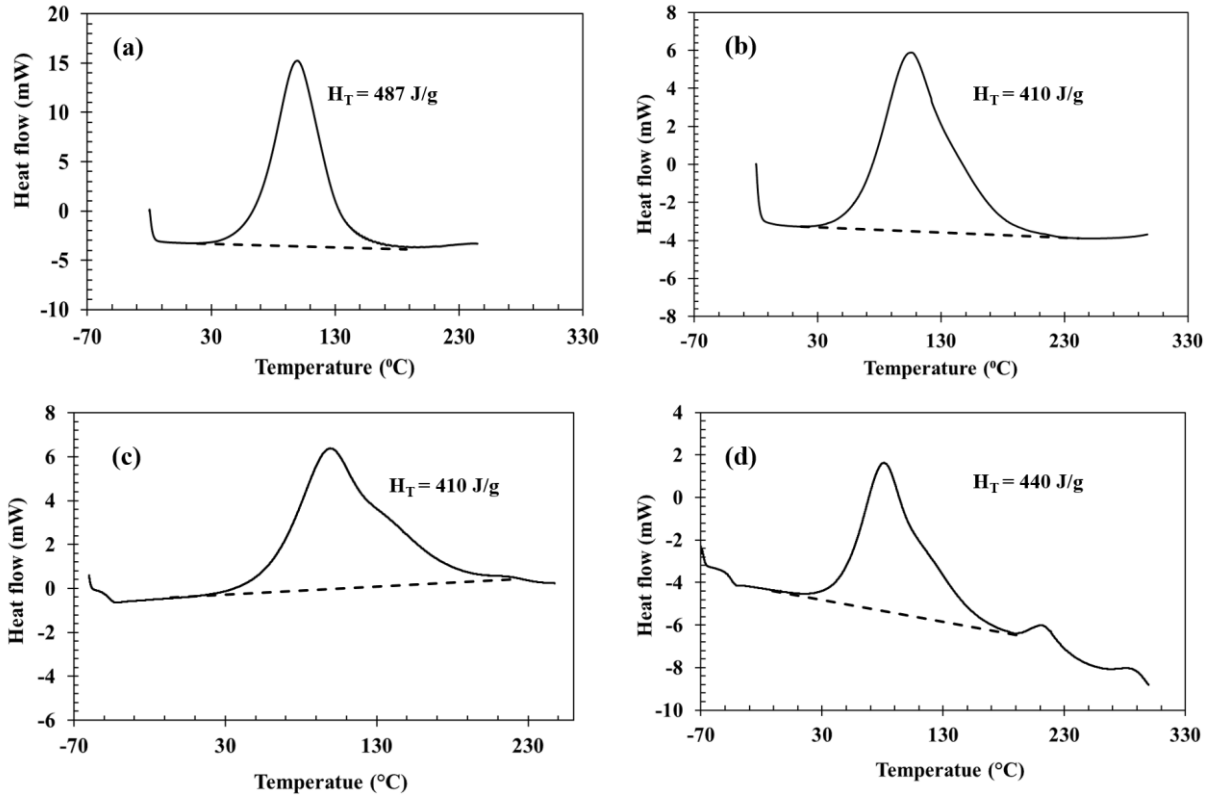

Figure 3-2: The results of heat flow for all four resin systems: (a) Hexion, (b) Airstone, (c) Gurit Standard, and (d) Gurit fast from DSC experiments for a ramp of 10 °C/min.

The degree-of-cure α, was calculated from the plot of cure rate vs time by integrating the area under the curve as shown by:

$$\alpha = \frac{1}{H_T}\int_0^t \left(\frac{dH}{dt}\right) dt \quad \text{Eq. 3-2}$$

Both mono-reactive and bi-reactive autocatalytic semi-empirical cure kinetic models were used in this work to model the cure rate as a function of degree-of-cure. Additionally, a diffusion term, $f(\alpha)$ was included to capture the diffusion driven low speed reaction. The equations can be summarized as:

$$\frac{d\alpha}{dt} = K_1\alpha^m(1-\alpha)^n f(\alpha) \quad \text{Eq. 3-3}$$

$$\frac{d\alpha}{dt} = (K_1 + K_2\alpha^m)(1-\alpha)^n f(\alpha) \quad \text{Eq. 3-4}$$

$$K_i = A_i\, exp\left(\frac{-E_{ai}}{RT}\right) \quad \text{Eq. 3-5}$$

$$f(\alpha) = \frac{K_e}{K_c} = \frac{1}{1 + exp\,[C(\alpha - (\alpha_{C0} + \alpha_{CT}T))]} \quad \text{Eq. 3-6}$$

where E_{ai} is the activation energy, R is the molar gas constant equal to 8.314 J/K.mol, T is the temperature, and A_i, m, n are the fitting constants. The experimental values of $\frac{d\alpha}{dt}$ are denoted by K_e and the corresponding cure kinetic model values are denoted by K_c. For non-diffusion-controlled cure kinetics reaction, the value of $f(\alpha)$ is 1 in Eq. 3-4. The terms C, α_{C0}, and α_{CT} are fitting constants used in Eq. 3-6 for the diffusion term in the denominator.

The initial step in the modelling process involved the determination of activation energy E_{ai} by calculating the slope of $\ln(\frac{d\alpha}{dt})$ versus $\frac{1}{T}$ at a low degree-of-cure of 0.1, 0.2 and 0.3. The average value of the activation energy for all the resin systems was found using this technique except for Gurit standard resin. Since Gurit standard resin consists of two activation energy terms, the second

E_{ai} was found by using the same technique, however at degree-of-cure of 0.6, 0.7, and 0.8. Figure 3-3 shows the plot for all resin systems.

The parameters $A_i, m, n,$ were found using the least squares non-linear regression between the cure rate and degree-of-cure for all the isothermal temperatures. For Gurit standard resin system an R^2 value of greater than 0.95 was obtained for the Eq. 3-4. For all the remaining resin systems an R^2 value of greater than 0.95 was achieved using Eq. 3-3.

The diffusion term was used to accurately capture the evolution of degree-of-cure using the cure kinetic model. The comparison between $\frac{K_e}{K_c}$ for the different isothermal temperatures are shown in Figure 3-4. Table 3-2 and Table 3-3 summarize the cure kinetic parameters for all the resin systems. There was no clear dependency on the temperature and hence the term α_{CT} was equal to 0. The term α_{CO} and C were determined using the average of the least squares nonlinear regression of independent isothermals. The comparison between the experiment and the cure kinetic model are shown in Figure 3-5 for all the resin systems.

The parameters A, m and n remain constant for temperatures between 50 ºC – 80 ºC for the Gurit Fast curing resin system. The parameters follow a linear behaviour while increasing the isothermal temperature starting from the critical temperature of 80 ºC (353.15 K) as shown in Figure 3-6. A logistic based function was used since the processing temperature was higher than the critical temperature for the constat value of the parameters A, m and n using a linear relationship as:

$$A = A_0 + \frac{A_m T + A_b}{1 + e^{-(T - T_c)(1/°C)}} \quad \text{Eq. 3-7}$$

$$m = m_0 + \frac{m_m T + m_b}{1 + e^{-(T - T_c)(1/°C)}} \quad \text{Eq. 3-8}$$

$$n = n_0 + \frac{n_m T + n_b}{1 + e^{-(T - T_c)(1/°C)}} \quad \text{Eq. 3-9}$$

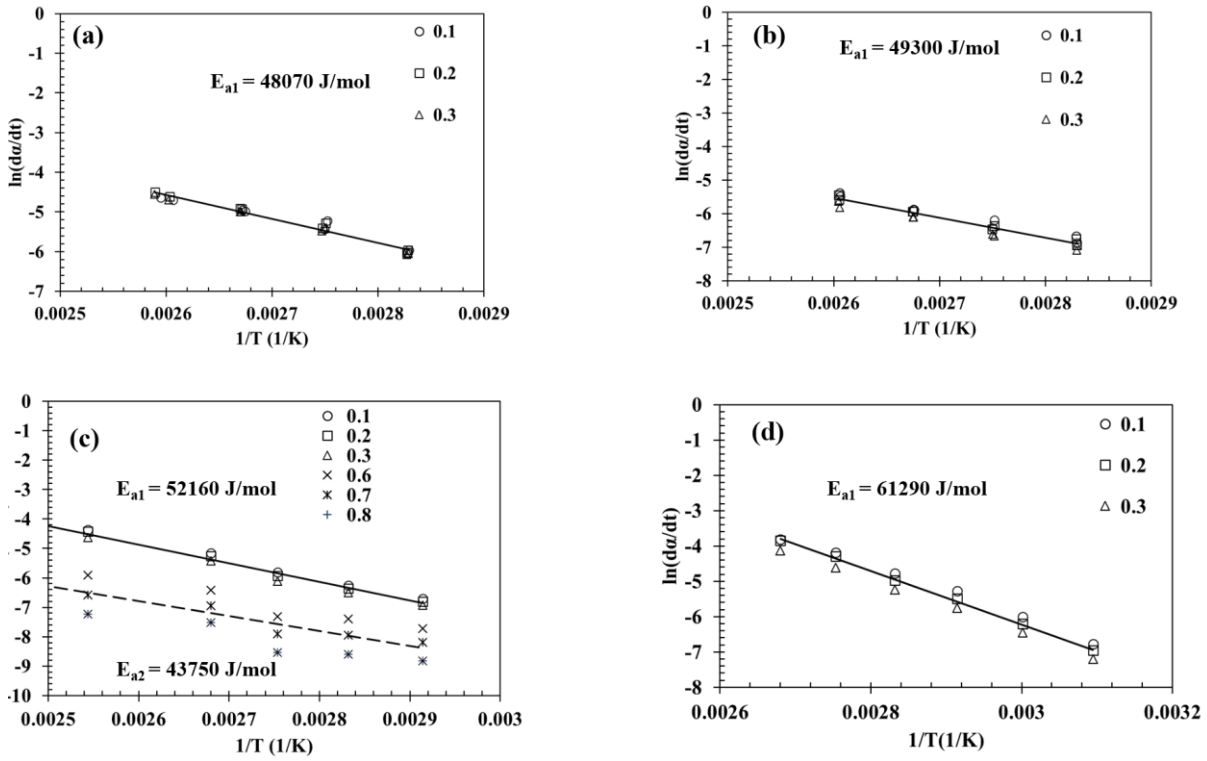

Figure 3-3: Logarithm of cure rate as a function of reciprocal of absolute temperature for (a) Hexion, (b) Airstone, (c) Gurit standard, and (d) Gurit fast. The activation energy was calculated using the slope the linear fit.

where $A, m,$ and n are defined as a function of temperature. A_0 , m_0,and n_0 are the values below the critical temperature T_c. Here $A_m, m_m$and n_m are slope of the linear increment defined as a function of temperature. A_b, m_b and n_b are the y-intercepts obtained from the linear function. The values are tabulated in Table 3-4.

3.1.3 Viscosity

3.1.3.1 Methodology

Like cure kinetics, the rheological behaviour of the resin was analysed using two types of rheometers. An AR2000 rheometer from TA Instruments was used for characterizing Hexion and Airstone resin systems. The Gurit Standard and Fast resin systems were characterized using the Anton Paar CTD 600 rheometer. An environmental test chamber was used by both machines and

the complex viscosity of the resin was measured in both dynamic and isothermal conditions. The experimental test matrix is shown in Table 3-5.

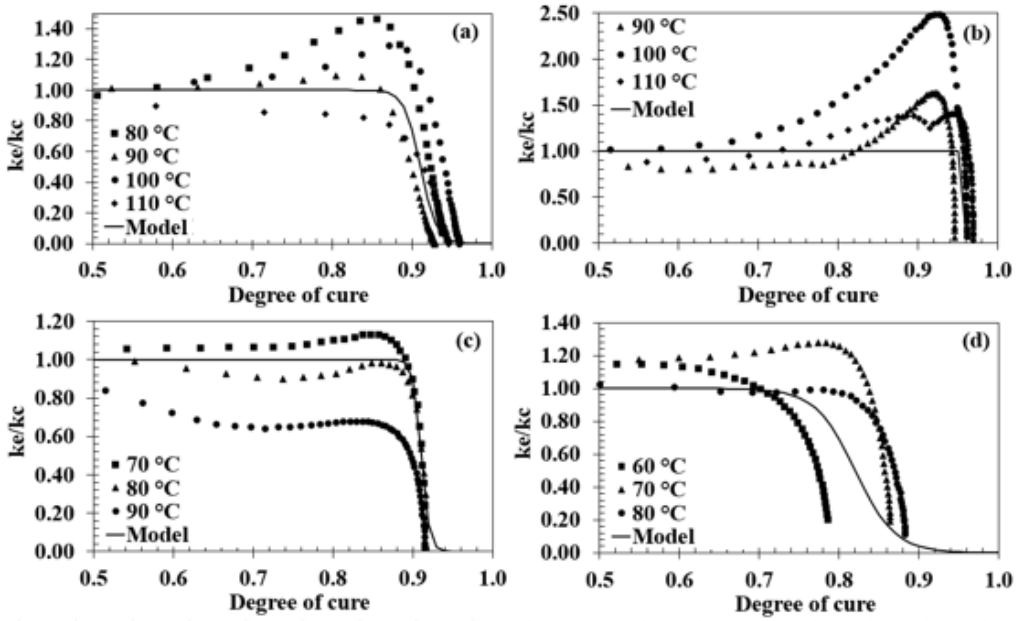

Figure 3-4: The relationship between experimental and cure kinetic model results, $\frac{K_e}{K_c}$, as a function of degree-of-cure for all four resin systems: (a) Hexion, (b) Airstone, (c) Gurit Standard, and (d) Gurit Fast.

Table 3-2: Parameters of the cure kinetic model for all four thermoset resins for all temperatures below the critical temperature T_C.

Resin	*Eqn.*	H_T (J/g)	A_1 (1/s)	E_{a1} (J/mol)	A_2 (1/s)	E_{a2} (J/mol)	m	n	Tc (°C)
Hexion	3	487	94100	48070	-	-	0.34	1.67	110
Airstone	3	410	56940	49300	-	-	0.28	2.32	110
Gurit Standard	4	410	-53090	52160	12280	43750	0.10	1.69	90
Gurit Fast	3	440	1.9e7	61290	-	-	0.15	2.63	80

Table 3-3: Parameters of diffusive term of the cure kinetic model.

Resin	C	α_{C0}	α_{CT}
Hexion	100	0.911	0
Airstone	1300	0.958	0
Gurit Standard	200	0.911	0
Gurit Fast	40	0.820	0

A volume of 0.5-1 ml was placed between aluminium parallel plates of dimensions 25 mm and trimmed to thickness between 0.5-1 mm. The strain sweep experiments were conducted to determine the linear viscoelastic range (LVR). For practical reasons, the tests for all the resin systems were conducted at 1Hz [129] and the percentage strains within the LVR range used are shown in Table 3-5. Three sets of data were collected for each trial.

3.1.3.2 Modelling

The viscosity of the resin was modelled using the methodology proposed by Khoun and Hubert[130]. The following equation developed by Castro and Macosko was used:

$$\eta = A_\eta \exp\left(\frac{E_\eta}{RT}\right)\left(\frac{\alpha_{gel}}{\alpha_{gel}-\alpha}\right)^{A+B\alpha} \quad \text{Eq. 3-10}$$

here α_{gel} is the degree-of-cure at gelation, and A_η, E_η, A and B are constants. The degree-of-cure was calculated using equations 3-3 – 3-6 using the temperature and time history from rheology tests. The gel point was determined by the intersection of the experimental data of storage moduli (G') and loss moduli (G''). Figure 3-7 shows the gel point for Gurit Standard resin at 80 ºC isothermal test. Eq. 3-10 was expressed as a linear relationship between the viscosity and inverse of temperature as:

$$\ln(\eta) = \ln(A_\eta) + \frac{E_\eta}{RT} \quad \text{Eq. 3-11}$$

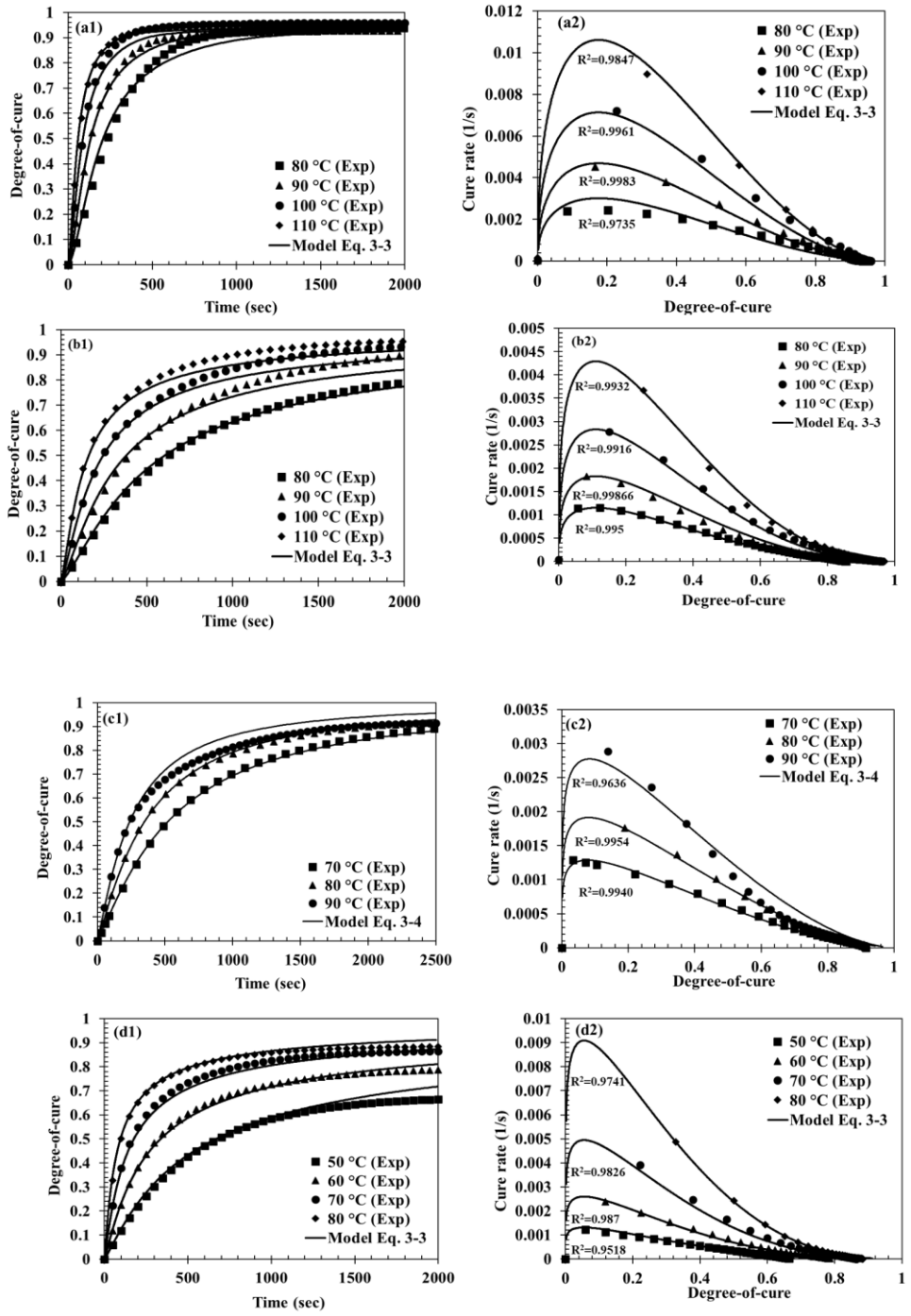

Figure 3-5: Comparison between experimental and model results for isothermal DSC tests on all four epoxy resins: (a) Hexion, (b) Airstone, (c) Gurit Standard, and (d) Gurit Fast.

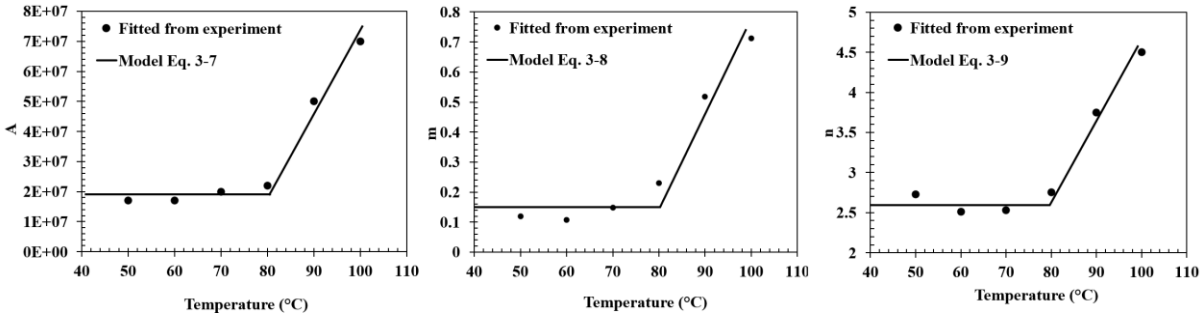

Figure 3-6: $A, m,$ and n as a function of the isothermal temperature as described in Eq. 3-7 – 3-9.

Table 3-4: Values of the fitting parameters for Gurit fast resin system

A_o (1/s)	A_m (1/sK)	A_b (1/s)	m_o	m_m (1/K)	m_b	n_o	n_m (1/K)	n_b
1.9e7	2.4e6	-8.46e8	0.15	0.02409	-8.413	2.63	0.08725	-30.77

Table 3-5: Experimental test matrix and percentage strain chosen from the linear viscoelastic range (LVR).

Material Resin	Dynamic Scan Ramp Rates (ºC/min)	Isothermal Scans Temperature (ºC)	% Strain
Hexion	5	80, 100, 110	1.0
Airstone	5	70, 100, 120	1.0
Gurit Standard	1,2,5	70,80,90	0.1
Gurit Fast	1,2,5	50,60	0.1

The constants A_η and E_η were calculated using linear regression from the viscosity data at the start of the isothermal scan. The parameters A and B were found using the least-squares nonlinear regression between viscosity and temperature with the generalized reduced gradient (GRG) solution method [131]. The parameters of the viscosity model for all four resin systems are listed in Table 3-6.

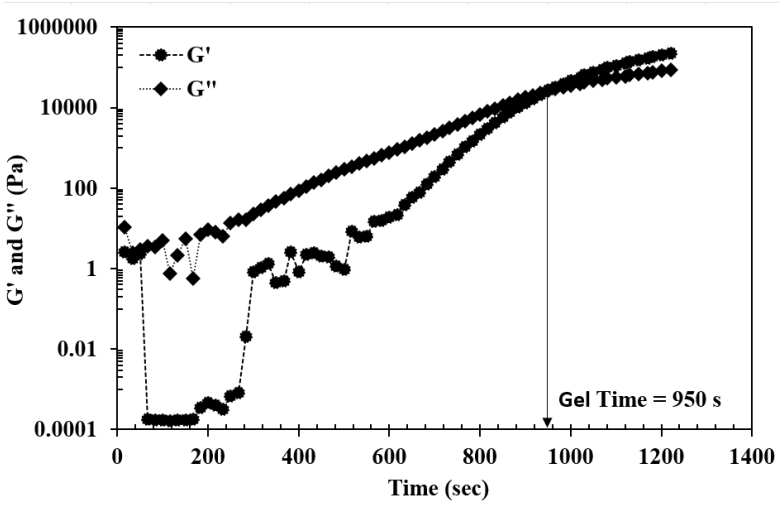

Figure 3-7: Storage and loss modulus of Gurit Standard resin at 80 ºC showing the time of gelation at the intersection point.

Table 3-6: Constant parameters of the viscosity model (Eq. 3-10).

Resin	E_μ (kJ/mol)	A_μ (Pa.s)	α_{gel}	A	B
Hexion	39.64	6.99e-07	0.65	-1.96	9.80
Airstone	23.67	2.23e-05	0.69	-1.77	5.07
Gurit Standard	31.78	1.68e-06	0.78	0.80	4.50
Gurit Fast	14.79	2.30e-03	0.67	1.00	4.40

The measured isothermal viscosity and the corresponding model results are shown in Figure 3-8. A good prediction of R^2 value greater than 0.80 was observed for all the resin systems. To achieve good impregnation in CRTM process, the viscosity of the resin should be below 1 Pas [132]. The model predicts with an R^2 value greater than 0.90 for viscosities less than 1 Pas. However, data capture at higher temperatures was difficult due to the extremely fast curing nature of the resins. By the time the resin was placed between the parallel plates and trimmed, a significant curing reaction had happened. Therefore, tests were performed only up to 120 ºC. These models were also extended to dynamic data as shown in Figure 3-9 for the Gurit Standard resin system.

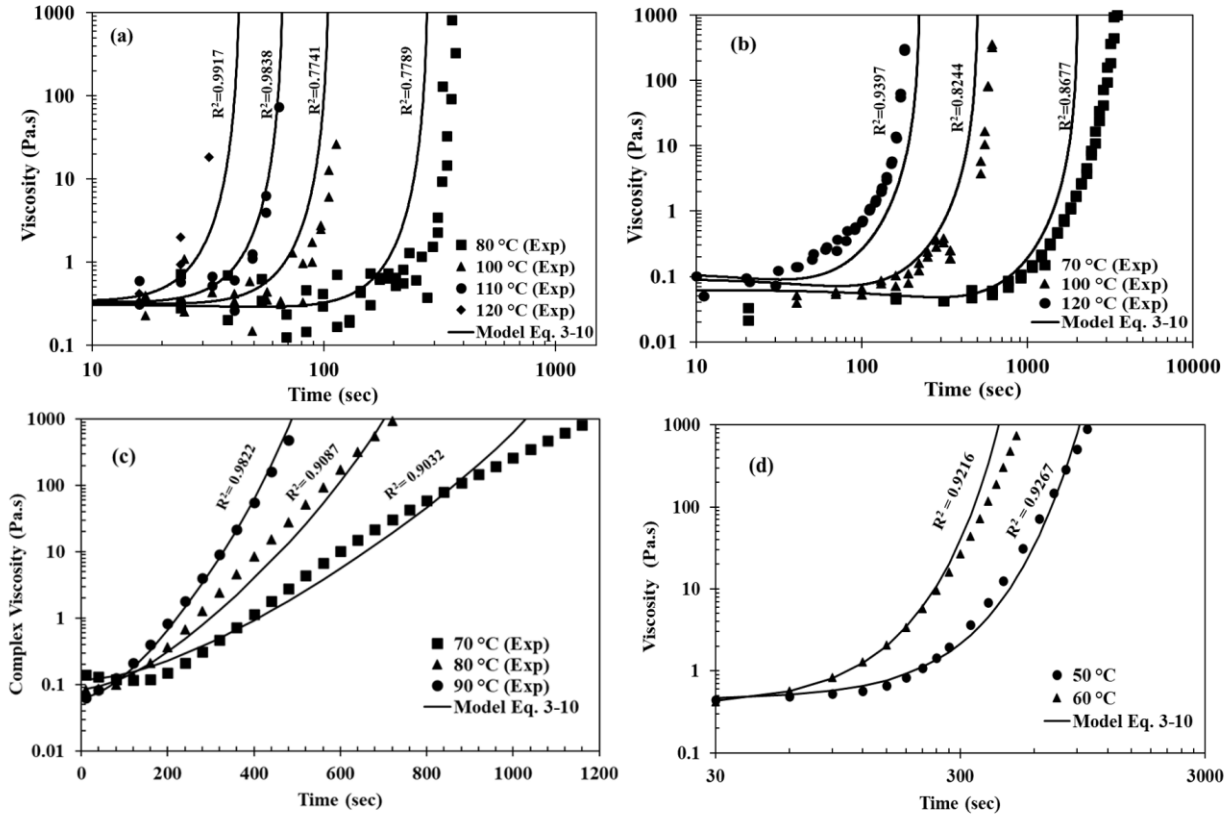

Figure 3-8: Experimental and viscosity model data at different isothermal temperatures: (a) Hexion, (b) Airstone, (c) Gurit Standard, and (d) Gurit Fast.

3.2 Resin characterization: Polyester resin

The highly reactive polyester resin system from AOC was analyzed to investigate the effect of inhibitor during processing conditions. The resin used here was an unsaturated polyester, which was mixed with Trigonox 93 (tert-Butyl peroxybenzoate, 80% solution with acetylacetone) curing agent and cobalt as a catalyst. Table 3-7 gives all the details on the resin system. All the experimental steps used for the epoxy resins were repeated.

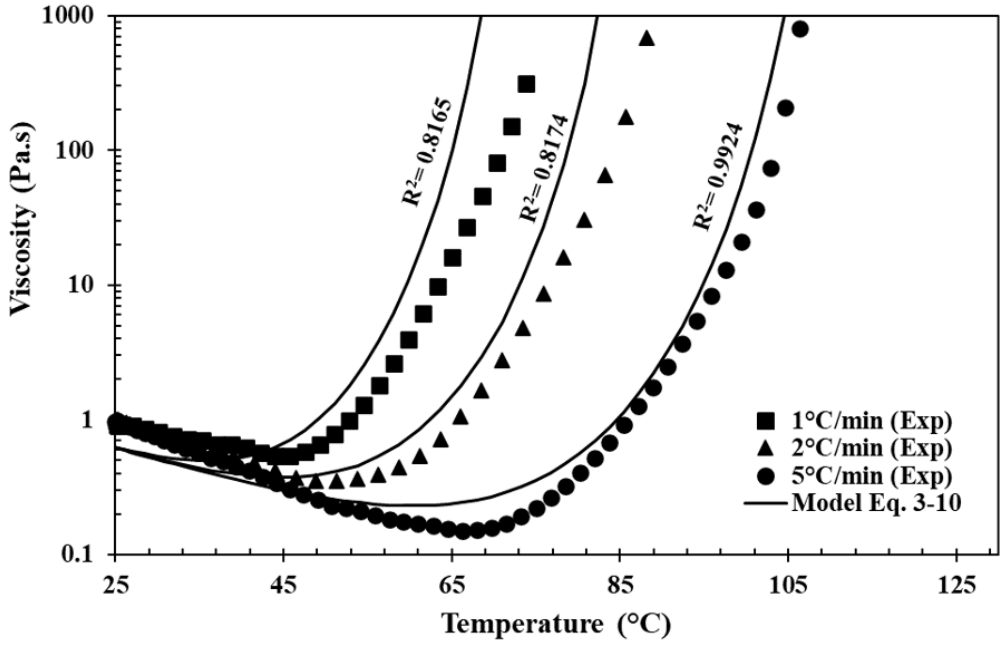

Figure 3-9: Experiment and model fit for dynamic data of Gurit standard resin

Table 3-7: Details and mixing ratio of polyester resin system.

Resin		Hardener	Mix ratio. Parts per weight
AOC	XG-2770	Trigonox 93	0.1% Cobalt 6% / 1.5% Trigonox 93

3.2.1 Thermal stability

The tests on thermal stability were performed on a TGA Q500 from TA Instruments. The samples were ramped at a 20ºC/min from room temperature (20ºC) to 700ºC under an air condition. The percentage weight reduction of AOC resin is shown in Figure 3-10. A 20% reduction in mass was observed below 100ºC, which is typical for polyester resin due to the significant release of moisture at this stage [133].

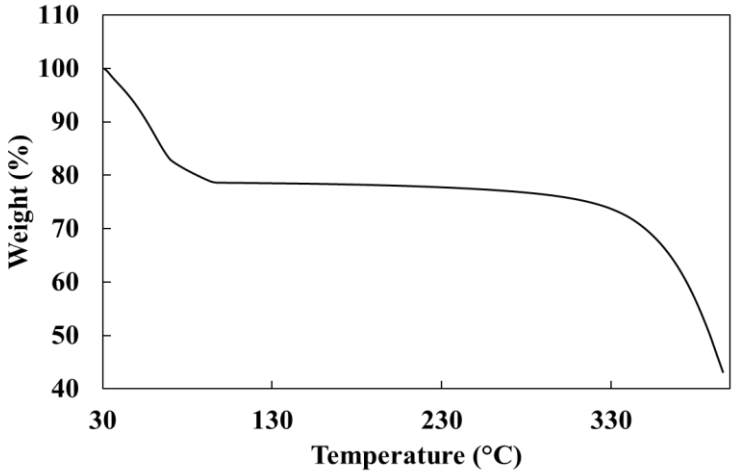

Figure 3-10: TGA curve of the AOC polyester resin.

3.2.2 Cure kinetics

3.2.2.1 Modelling: Effect of inhibitor

To include the effect of inhibitors, Eq. 3.3 was modified with an extra function $f_{inhibition}(T,t)$, to represent the time delay before the reaction begins to occur. The equations are given as:

$$\frac{d\alpha}{dt} = K\alpha^m(1-\alpha)^n f_{diffusion}(\alpha,T) f_{inhibition}(T,t) \quad \text{Eq. 3-13}$$

$$f_{inhibition}(T,t) = \frac{1}{1+exp\,[-(t-UT^w)]} \quad \text{Eq. 3-14}$$

where U= 1.55x10^{83} and w = -31.78 are the fitting parameters. t and T are the time and temperature in seconds and kelvin respectively. The inhibition term resembles a logistic function commonly used to model gradual transitions or delays. This function starts at a low value near zero at early times and gradually approaches 1 as t increases. This gradual transition is ideal for representing how an inhibitor slows the start of the reaction, allowing a smooth increase in the reaction rate over time as the inhibitor's effect diminishes. The inclusion of a temperature-dependent parameter

UT^w makes the inhibition function adaptable to different temperatures, reflecting the fact that inhibitors often have a temperature-dependent activity. The relationship between the isothermal temperature versus inhibition time is given by Figure 3-11. The reaction is restricted by the inhibition function until the inhibition time is reached using Eq. 3-14. Figure 3-12 shows the comparison between the experiment and simulation with an R^2 values greater than 0.89. The cure kinetic parameters are listed in Table 3-8.

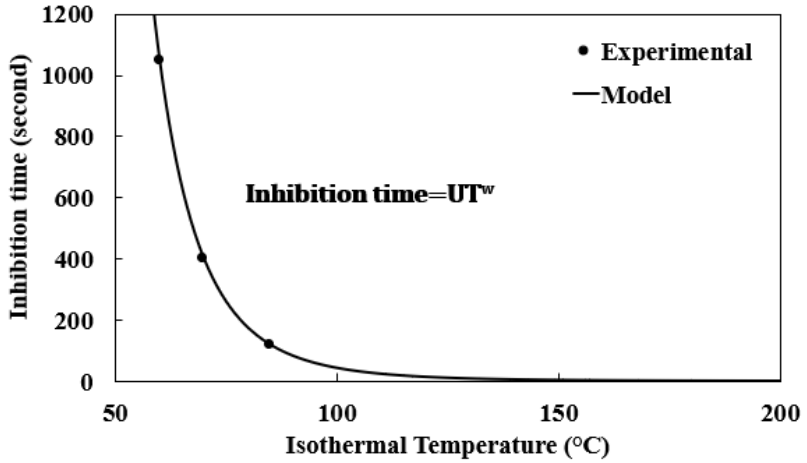

Figure 3-11: Comparison between isothermal experimental temperature and the inhibition time model for the AOC polyester resin system.

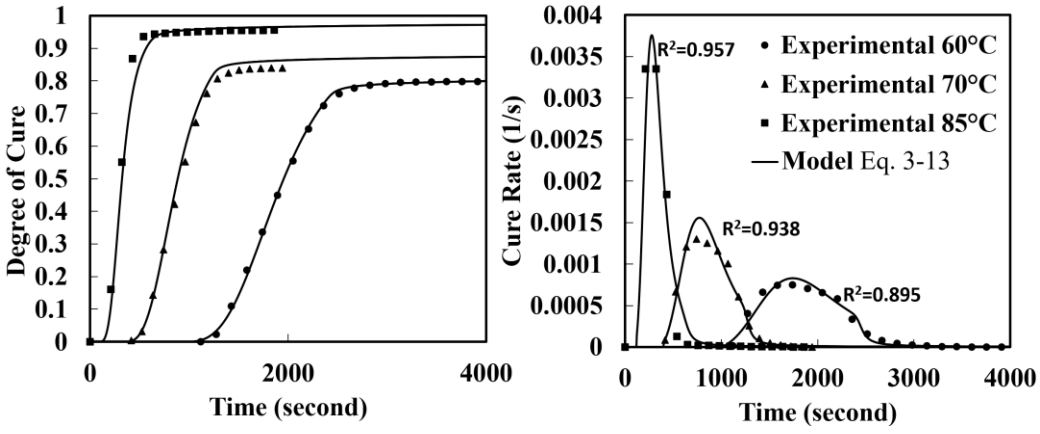

Figure 3-12: Comparison between experiment and cure kinetic model for isothermal DSC test results for AOC polyester resin.

Table 3-8: Cure kinetic model parameters for AOC polyester resin (Eq. 3-3)

Parameter	Value
H_T	374 J/g
A_1	8.62e08 s^{-1}
E_{a1}	60390 J/mol
m	0.66
n	1.34
T_c	85 ºC

3.2.3 Viscosity

3.2.3.1 Modelling

A simpler widely used model was used to capture the experimental results of the AOC polyester resin system [134]. The equation was given as follows:

$$\eta = A_\eta exp\left(\frac{E_\eta}{RT} + Z\alpha\right) \quad \text{Eq. 3-15}$$

here Z is a fitting parameter. The constant parameters of the models are listed in Table 3-9. The experimental and model results at isothermals 60ºC, 70ºC and 85ºC are shown in Figure 3-13. The model was also extended to a dynamic ramp as shown in Figure 3-14.

Table 3-9: Parameters for the viscosity model of AOC polyester resin.

Parameter	Value
A_η	1.15e-04
E_η	22.65 kJ/mol
α_{gel}	0.03
Z	250

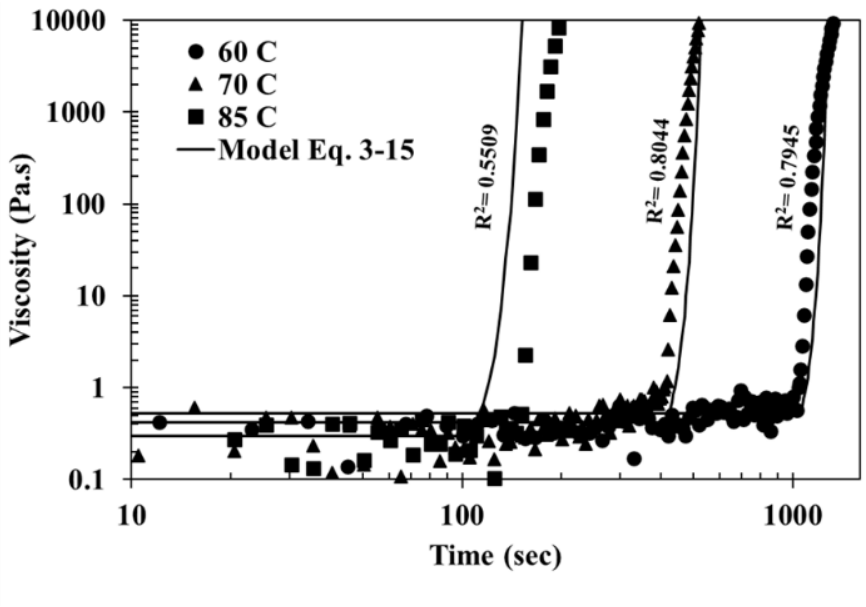

Figure 3-13: Experimental and viscosity model data at different isothermal temperatures for AOC polyester resin

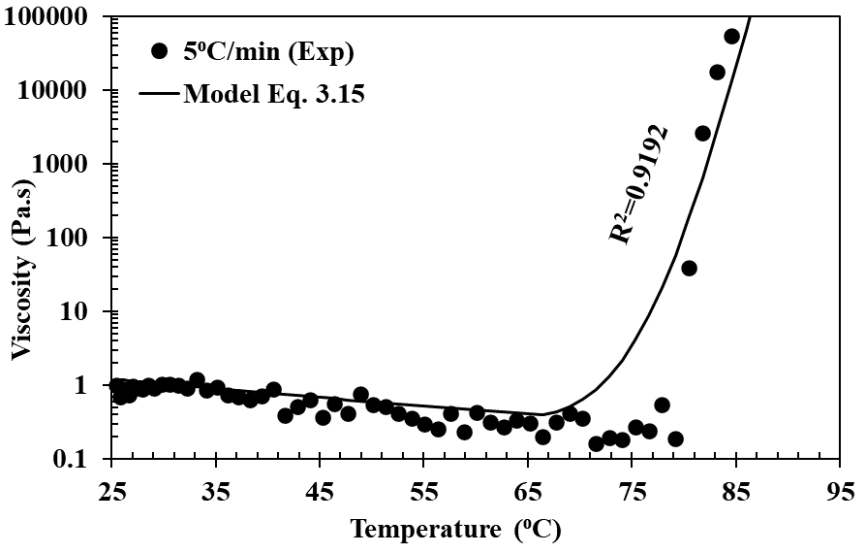

Figure 3-14: Experimental data and model fit for dynamic ramp for AOC polyester resin system including the effects of inhibitor.

3.3 Fibre characterization: permeability

3.3.1 Material description

The material used in this work was a glass fibre NCF called TG15N supplied by Texonic Inc. The details of the fibre are summarised in Table 3-10. The fibre architecture of a single sheet of fabric consists of a layer of unidirectional glass fibres in the warp direction placed between two layers of glass fibres in the weft direction held in place together by a thinly stitched polyester yarn. The direction of stitching was in the warp direction and the schematic of the structure is shown in Figure 3-15. The fabric used in this study was a biaxial warp knitted NCF which was designed particularly for high productivity and low-cost manufacturing processes [135].

3.3.2 In-plane permeability

The two main directions of the permeability in the in-plane or axial directions are K_1 and K_2 of the permeability tensor term in the Darcy's equation [136]. In the case of TG15N NCF, the warp direction permeability (stitching direction) was K_1 and the weft direction permeability was K_2.

Table 3-10: Information on TG15 N technical data sheet [135]

Parameter	Value
Infused thickness	0.45 mm
Warp/Weft weight ratio	44% - 56%
Warp material composition	735 tex Glass fibre
	16.7 tex Polyester
	0.031/ cm Ends count
Weft material composition	255 tex Glass fibre
	0.104/cm Ends count
Areal weight	518 g/m^2
Standard roll length	100 m

3.3.2.1 Experimental setup and procedure

The equipment was designed in-house to measure the permeability in the in-plane direction. The device consisted of a tabletop fixture fitted with pneumatic actuators, as shown in the Figure 3-16.

The inlet tube was connected to a pressure pot and silicone oil (XIAMETER® PMX-200 Silicone oil 100CS) with a viscosity 0.1 Pas was used as the testing fluid. The outlet was maintained at atmospheric pressure, which directed the pressurized fluid in a 1D direction. A schematic of the equipment is shown in Figure 3-17, showing all the important components. A glass plate was used to visually track the flow front using a video recording device. Linear line markings were drawn on the glass plate to indicate the live position of the flow front. The cavity thickness was controlled using shims. Vacuum sealant tape was used to provide good compaction pressure and prevent race tracking along the edges. The equipment was fitted with a data recording unit controlled by LabVIEW to measure inlet pressure and track the flow front.

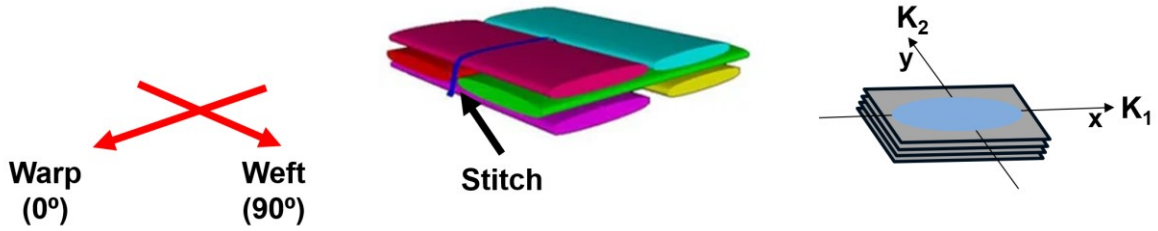

Figure 3-15: Fibre architecture of TG15N NCF showing the direction of K_1 and K_2. Reproduced from [135] with permission.

The first step in measuring the permeability was to get the fibres cut in specific directions. The schematic of the cutting angles is shown in Figure 3-18. The volume fraction V_f was determined using the following equation:

$$V_f = \frac{A_w . N}{\rho_f . h} \qquad \text{Eq. 3-16}$$

where A_w is the areal weight of the fibre (g/m^2), N is the number of plies, ρ_f is the density of the fibres (kg/m^3) and h is the cavity thickness (m). The cavity thickness was maintained constant

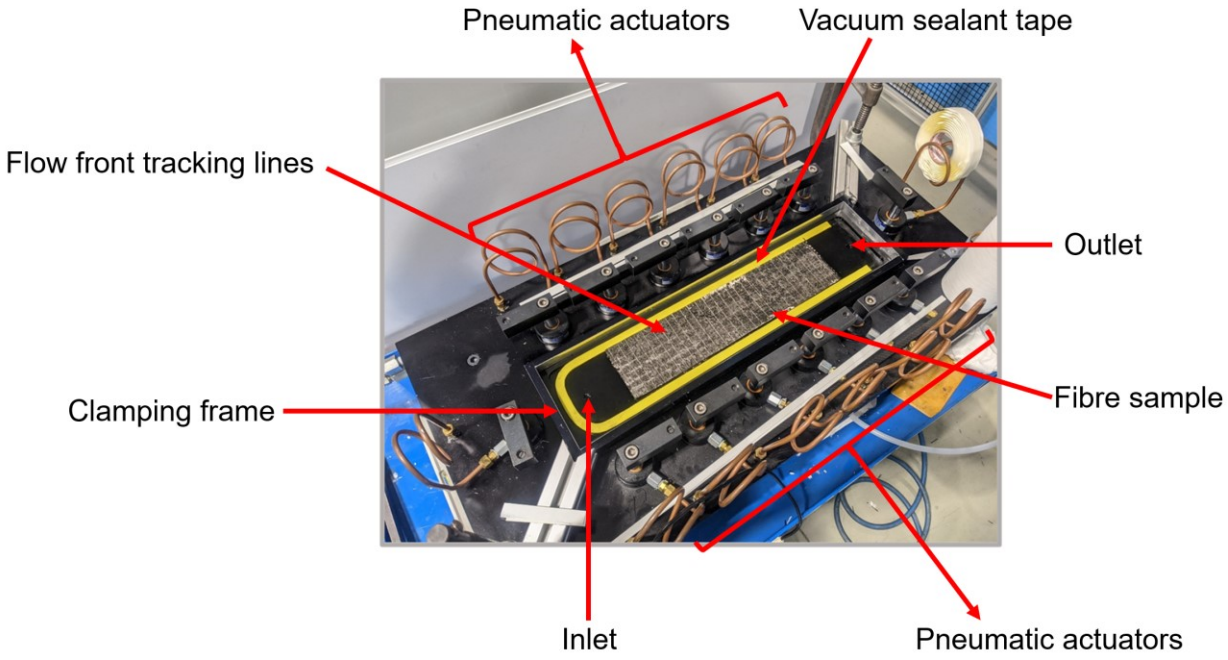

Figure 3-15: In-plane permeability measuring equipment.

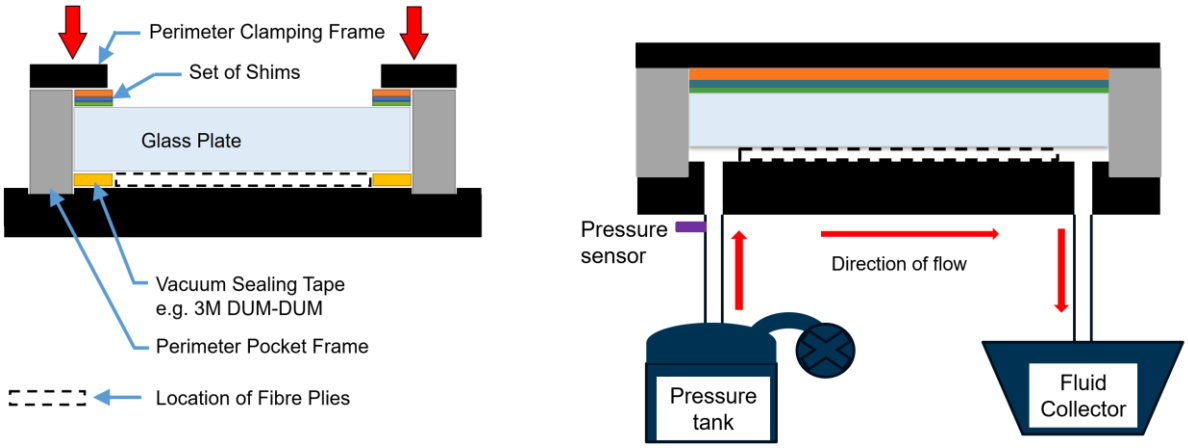

Figure 3-16: The schematic of the cross sectional view of the in-plane permeability measuring equipment (Left). The side view of schematic showing the pressure tank, flow direction of the test fluid and the fluid collector (Right).

throughout the tests and the number of plies was varied to perform tests at different fibre volume fractions. The values used in Eq. 3-16 are listed in Table 3-11. At this stage the sample area was lined with the vacuum sealant tape and the fibres were placed in the channel. The glass plate was placed on top of the fibres and the clamping mechanism was activated using the pneumatic actuators. Finally, silicone oil was pressurised in a pressure pot and injected at low pressure into the cavity with fibres. The flow front data and time were recorded at every tracking line on the glass. Since the measured permeability is an unsaturated permeability, the following equation was used to calculate the permeability [137]:

$$K = \frac{x_{ff}^2.\left(1 - V_f\right).\eta}{2.P_{inj}.t_{ff}} = \frac{m_{ff}.\left(1 - V_f\right).\eta}{2.P_{inj}} \qquad \text{Eq. 3-17}$$

where x_{ff} refers to the position of the flow front at time t_{ff}, P_{inj} is the injection pressure and m_{ff} is the slope of the curve x_{ff}^2 versus t_{ff}. Three repetitions were done for every volume fraction chosen for the test. First set of experiments were carried out to measure permeability in the cutting directions as described in the schematic shown in Figure 3-18. The tests at three cutting directions were conducted at a constant volume fraction of 44.47%. The injection pressure was maintained below 70kPa for all the trials. Figure 3-19 shows the experiment in progress.

3.3.2.2 Results

The plot of permeability versus the cutting angle is shown in Figure 3-20. The permeability in 90º direction is slightly higher than in 0º consistent with the results obtained by Karaki et al. [138] for TG15N NCF. However, the permeability in 45º was found to be the lower than at 0º, contrary to the results obtained by Karaki et al. [138], where the values were slightly higher than 0º. Moreover, the principal permeability values K_1 and K_2 (0º and 90º respectively) were considered close enough to carry out the remaining tests in 0º orientation.

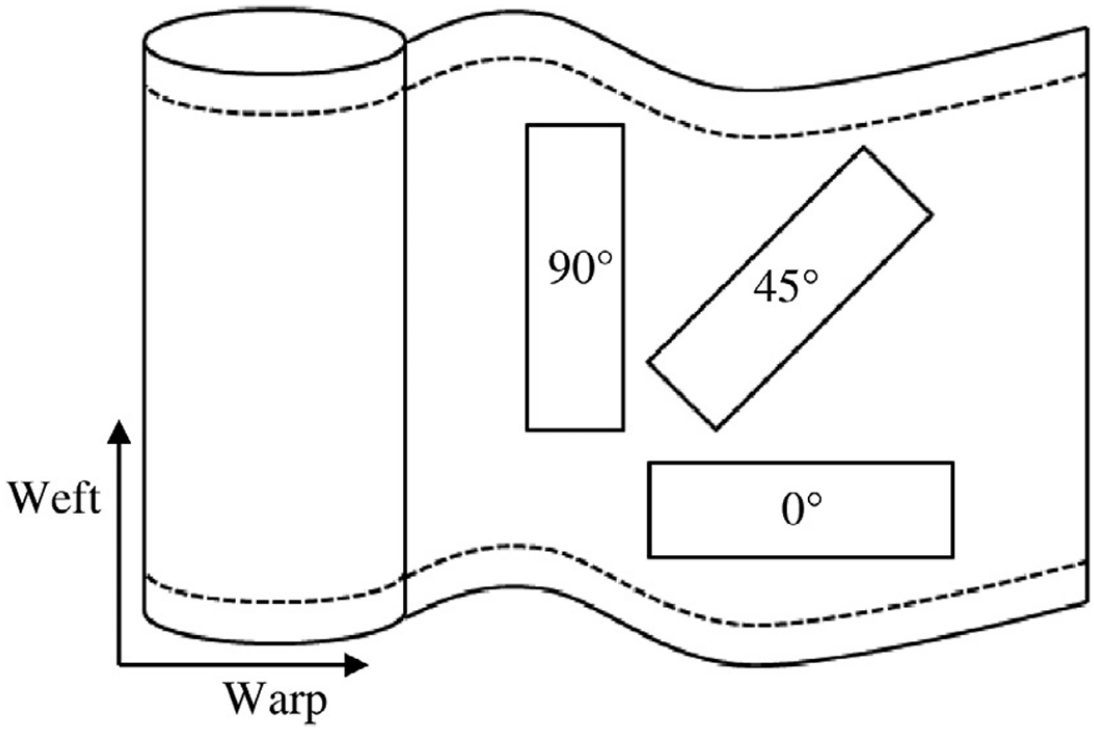

Figure 3-17: The schematic of the cutting directions used in the calculation of in-plane permeability [137].

Table 3-11: Tool setup details for TG15N permeability measurement in in-plane direction.

Sample size (mmx mm)	Length/width ratio	Cavity thickness (mm)	Number of layers	Tool material
400 x 95	4.21	2.24	5	Steel (bottom) Glass (top)

To develop the material model, tests were carried out for two more volume fractions to obtain a total of three data points. The permeability versus fibre volume fraction plot is shown in Figure 3-21. The results show a decrease in permeability with an increase in volume fraction which is typical for glass NCF.

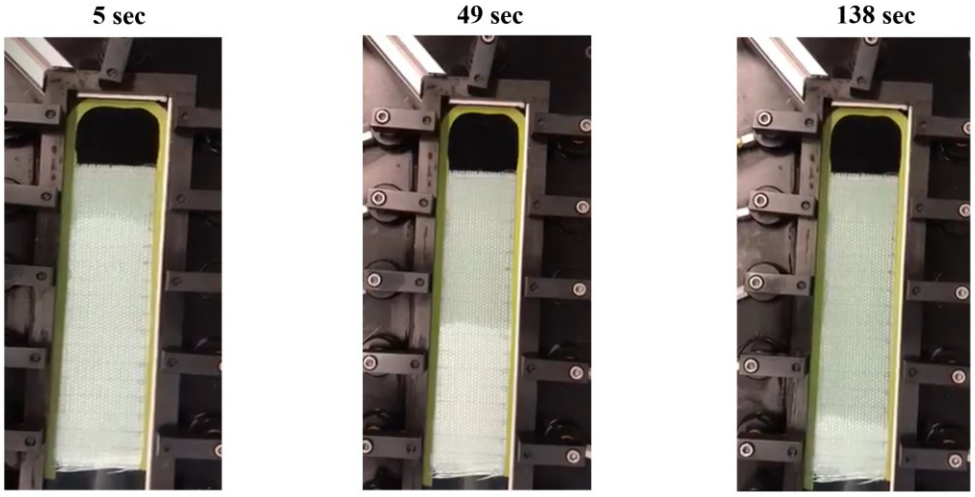

Figure 3-18: Silicone oil flow front progression as recorded by the camera for measuring fibres in 90 degree direction (K_2) with a volume fraction of 44.47%.

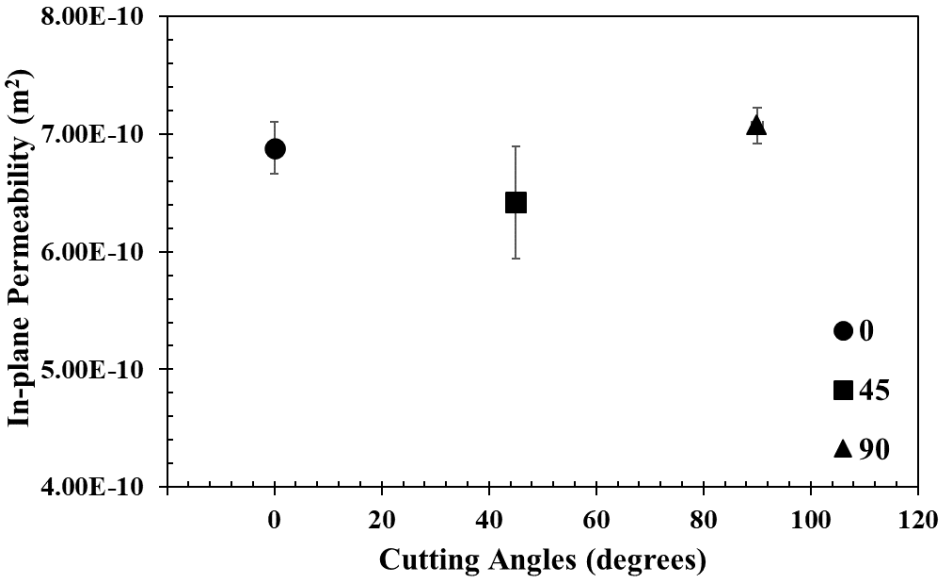

Figure 3-19: Variation of in-plane permeability with respect to cutting direction (0º, 45º, and 90º) for TG15N NCF.

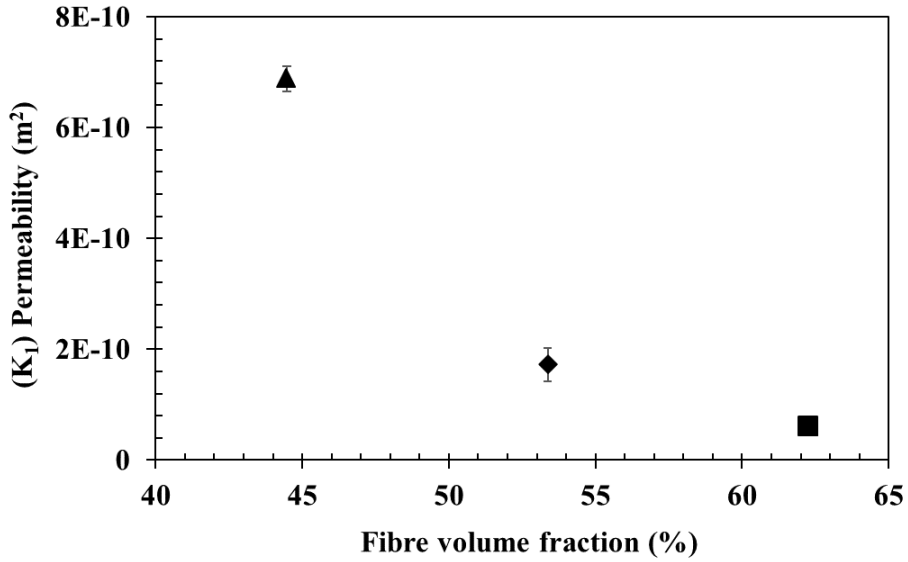

Figure 3-20: Permeability vs fibre volume fraction for three different volume fractions in in-plane direction for TG15N NCF.

3.3.3 Transverse permeability

The term K_3 in the permeability tensor of Darcy's equation is referred to as transverse or out-of-plane permeability. The schematic of the TG15N fabric and the transverse direction are shown in Figure 3-22.

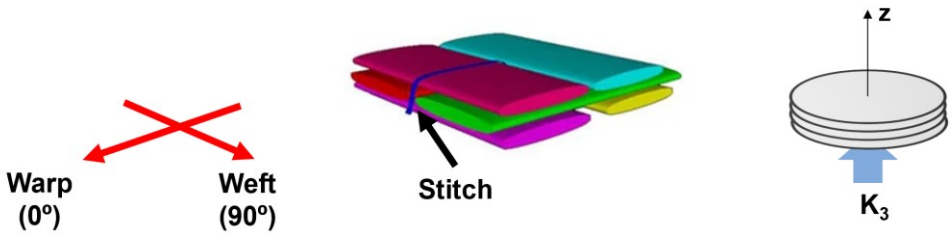

Figure 3-21: Fibre architecture of TG15N NCF showing the direction of K_3. Adapted from [135] with permisson.

3.3.3.1 Experimental setup and procedure

In-house equipment was designed to measure the permeability in the transverse direction. The components of the fixture are shown in Figure 3-23. The equipment consisted of a hollow cylinder through which a perforated airtight circular plate structure was inserted. This was connected to a stepper motor by means of a shaft couple, which transferred the rotations from the stepper motor to the acme rod which was used to control the thickness of the cavity in which the sample was placed. The bottom perforated plate was connected to a small hollow cylinder to which the inlet tube was connected. The outlet was kept at atmospheric pressure and the testing fluid (XIAMETER® PMX-200 Silicone oil 100CS) was pressurised using a pressure pot. The stepper motor, pressure sensor and the weighing scale were all controlled and calibrated using LabVIEW. The schematic of the setup is shown in Figure 3-24.

The first step involved the cutting the fibres using a circular die of diameter 76 mm with the aid of a handheld press, as shown in Figure 3-25. The silicone oil was injected into the equipment from the pressure pot into the resin injection gate. The silicone oil coming out from the outlet tube was collected on a measuring jar placed on the weighing scale, as shown in the Figure 3-24. Care was taken to ensure steady state was achieved (constant injection pressure) by only starting to record the data after the reading from the pressure sensor showed a constant value. The inlet pressure, time and weight of the resin collected were recorded for the entire process using LabVIEW. The permeability measured in this case was the saturated permeability as it gives more consistent and repeatable data [82]. In the CRTM process, when resin is injected into the preform, the preform becomes fully saturated once the resin contacts the top mould in through-thickness direction. Therefore, using saturated permeability in this context is more appropriate and relevant for accurate analysis. The following equation was used to measure the permeability:

$$K = \frac{Q\eta h}{\mathrm{A}P_{inj}} \qquad \text{Eq. 3-18}$$

A is the area of the cross-sectional area, and h is the cavity thickness. The volumetric flow rate Q was calculated using the following equation:

$$Q = \frac{Total\ volume\ of\ silicone\ oil\ collected}{Total\ time} \qquad \text{Eq. 3-19}$$

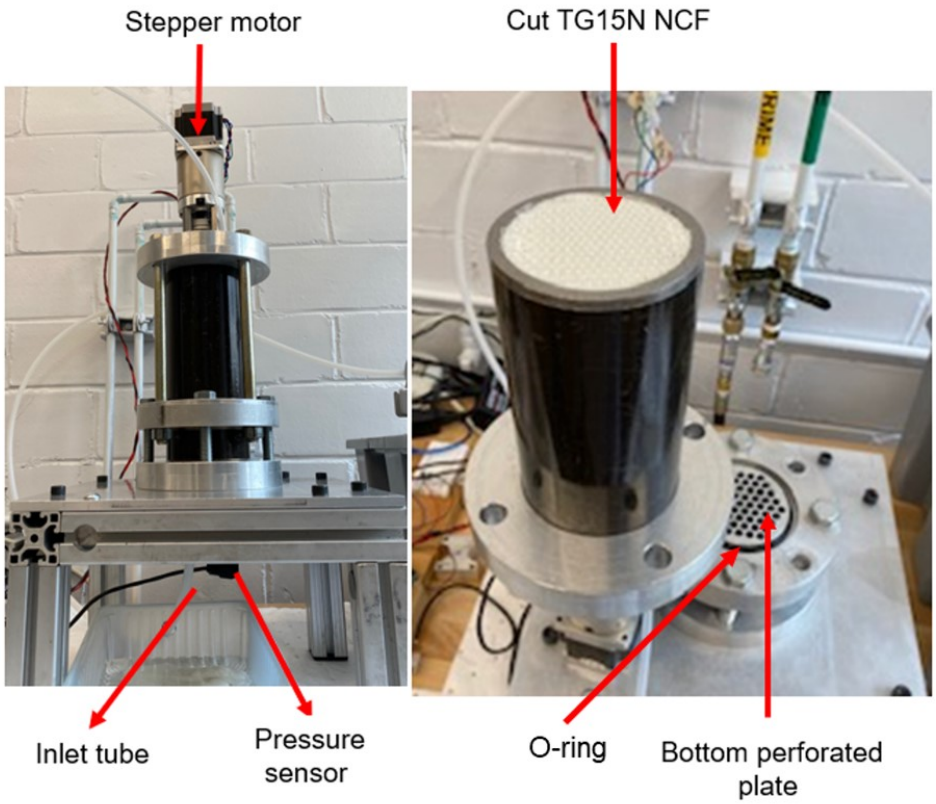

Figure 3-22: Pictures showing different components of the transverse permeability setup.

Three repetitions were conducted for each volume fractions chosen for this experiment. Four plies of circular fibre stacks were placed in the zero direction for all the tests. The injection pressure was maintained between 100 kPa and 200 kPa.

3.3.3.2 Results

The measured permeability for three different fibre volume fraction is shown in Figure 3-26. A decrease in permeability was observed with increasing fibre volume fraction, similar to in-plane permeability. Standard deviation of each individual tests also reduced with increasing fibre volume

fraction as a result of reduced thickness causing nesting between the layers, a result consistent with the latest benchmarking exercise on transverse permeability [82].

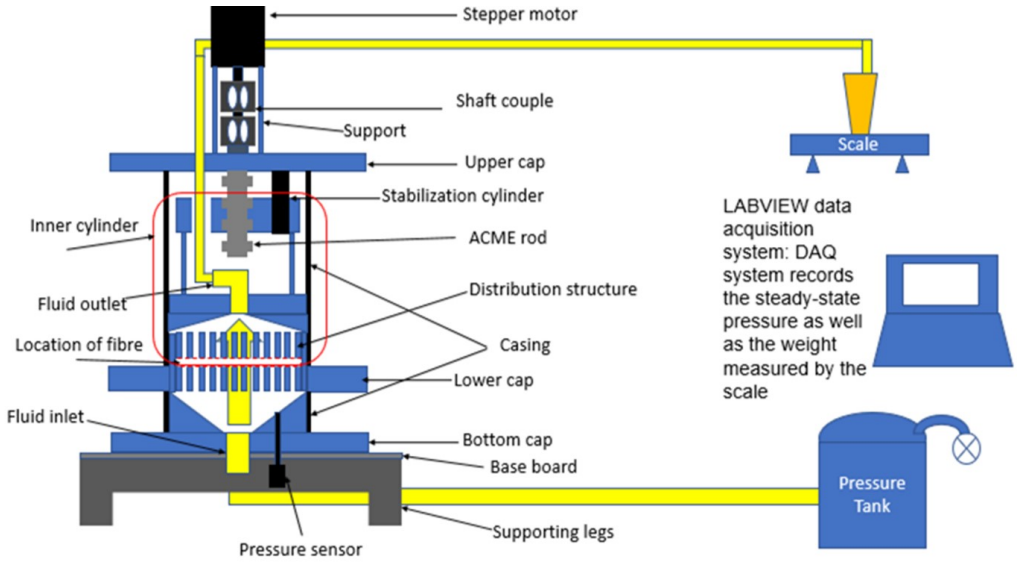

Figure 3-23: Schematic of the transverse permeability measuring setup.

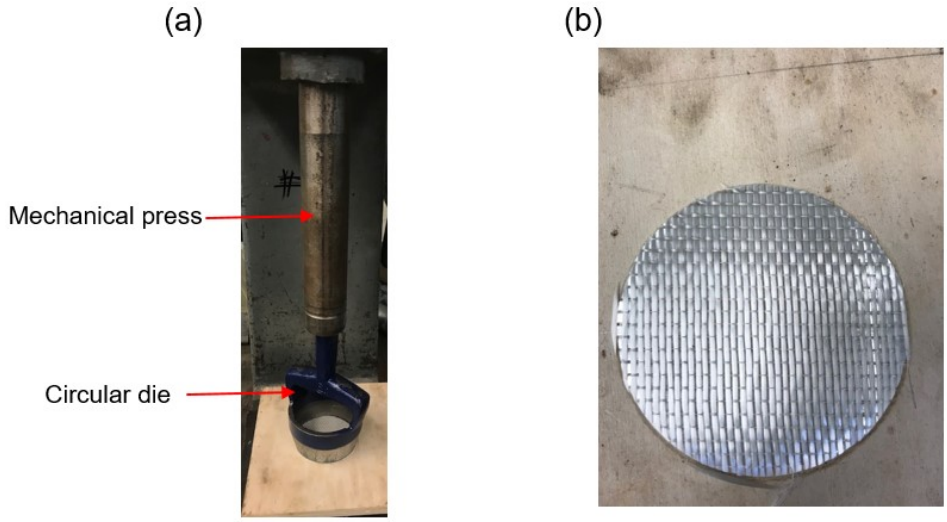

Figure 3-24: (a) The mechanical press used to cut TG15N NCF with a circular die (76 mm diameter), and (b) a single cut ply.

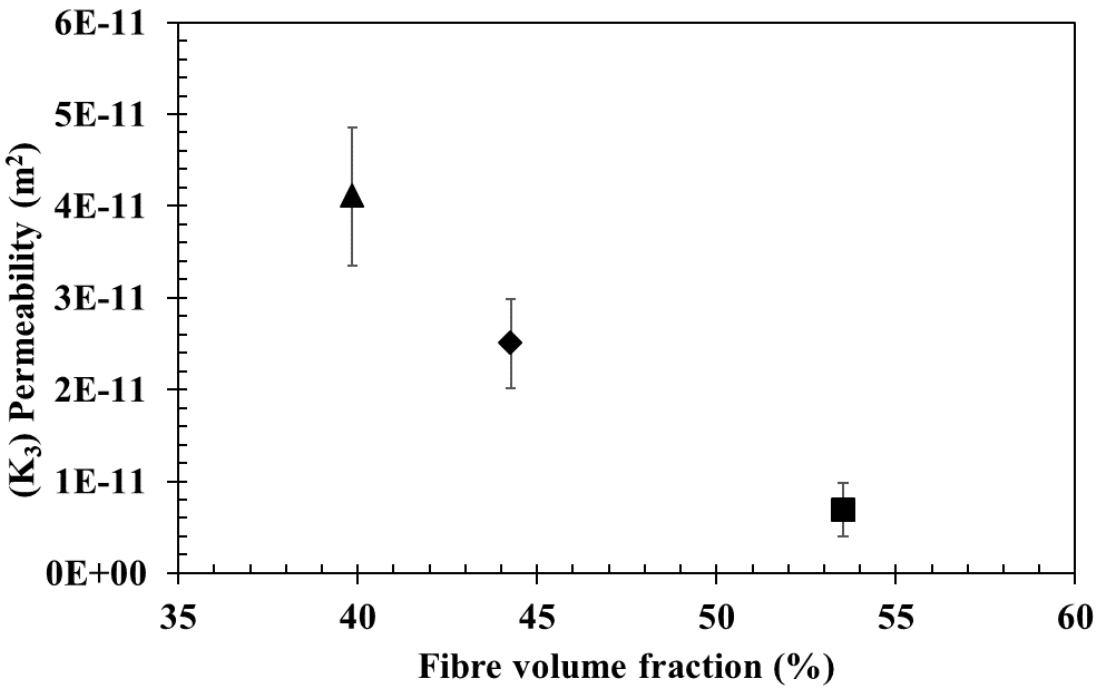

Figure 3-25: Permeability versus fibre volume fraction in transverse direction for TG15N NCF.

3.3.4 Modelling

Power law (Eq. 2-23) and modified Kozeny-Carman (Eq. 2-25) equations were used to model both in-plane and transverse permeability. The fitting parameters and the Kozeny-Carman constant were calculated from the experimental data. Figure 3-27 shows the comparison between model and experimental data for both in-plane and transverse directions. Table 3-12 shows all the fitting constants for both the power law and modified Kozeny-Carman equations.

3.4 Fibre characterization: compaction

As discussed in Section 2.1.2.2, characterization of the compaction behaviour of the fibres is a necessary material model input for the flow and compaction model of the CRTM process. In this section, the details of the characterization techniques used to understand the compaction behaviour of fibres under dry and wet conditions are presented.

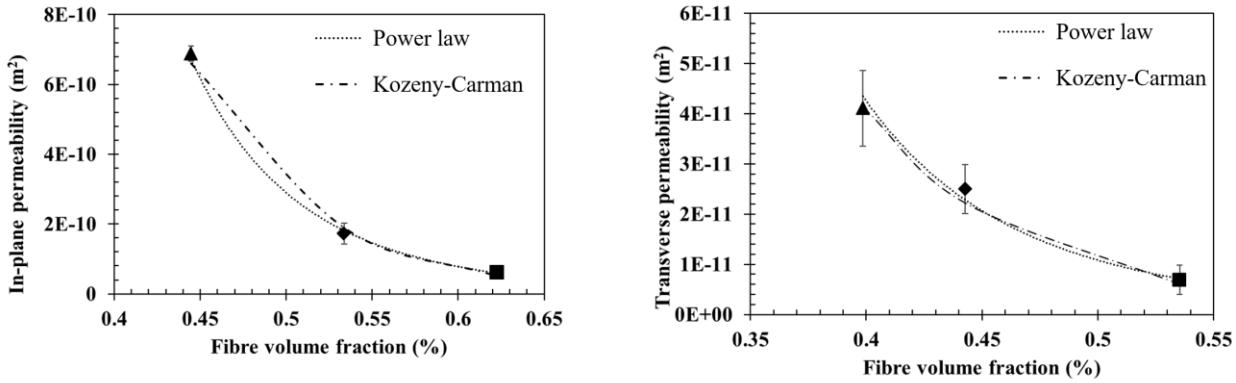

Figure 3-26: Power law and Kozeny-Carman fit for both in-plane (Left) and transverse (Right) permeability.

Table 3-12: Power law and modified Kozeny-Carman fitting constants

Permeability	a (m^2)	b	C (m^2)	n
In-plane	2E-12	-7.178	6.10E-10	3
Transverse	2E-13	-6.131	2.00E-11	3

3.4.1 Dry compaction

3.4.1.1 Experimental setup and procedure

The experimental setup developed to capture the compaction response of the fibre is shown in Figure 3-28, similar to the apparatus used by Hubert [139]. The equipment was mounted on an MTS Insight universal testing machine (UTM) with a 5 kN load cell. Even though the UTM has an inbuilt displacement measuring sensor, the equipment was fitted with an LVDT linear position sensor, as shown in Figure 3-28. The fibre samples were cut into 50 mm x 80 mm rectangular shape and a layup sequence of $[(0/90)_{4s}]$ was chosen.

The load-unload method was used to obtain the compaction curve [139]. The tests were conducted at a displacement rate of 0.5 mm/min up to a maximum load of 1 kN. Before each trial, a machine compliance test was performed without the sample. At this stage, the fibre samples were placed in

the mould, and the top mould was moved down until it just touched the sample as shown in Figure 3-28. This was considered as initial thickness of the sample, and the initial volume fraction was calculated using Eq. 3-16. The samples were compacted to a load of 1 kN and unloaded again at the speed of 0.5 mm/min. The load and displacement data from the UTM and the LVDT were recorded.

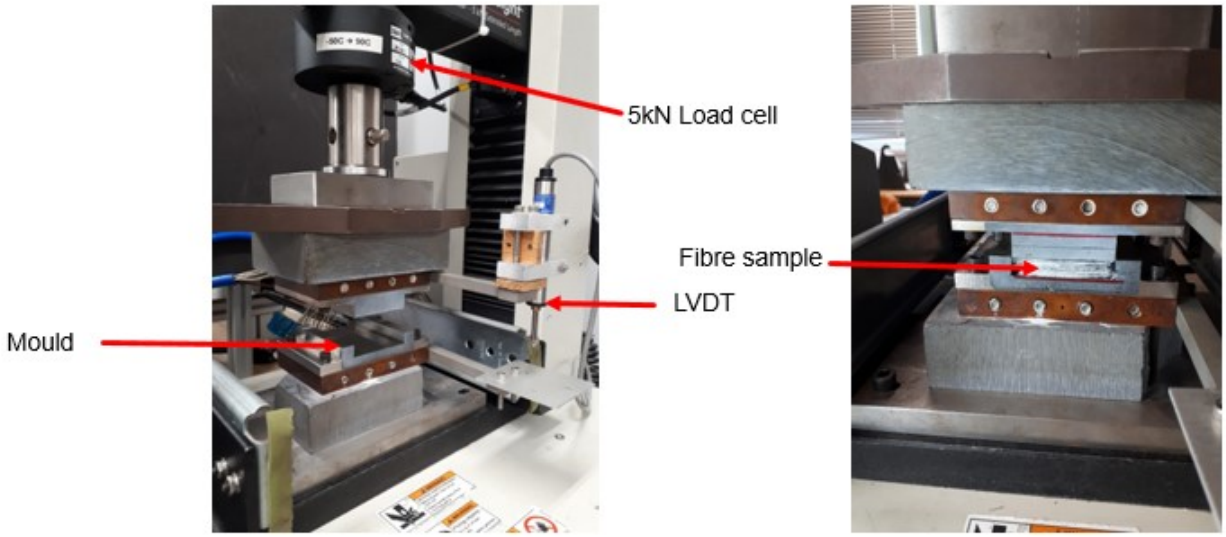

Figure 3-27: Compaction testing jig attached to the UTM fitted with LVDT (Left) and the fibre sample place between the mould platens (Right).

3.4.1.2 Results

The load-displacement curve obtained from the LVDT for the compaction test is shown in Figure 3-29. The volume fraction at each data point was calculated using Eq. 3-16. The compaction stress ($\bar{\sigma}$) was calculated using the equation:

$$\bar{\sigma} = \frac{F}{A} \qquad \text{Eq. 3-20}$$

here F is the applied load and A is the cross sectional area of the fibre specimen. A simple power law model was used to develop a relationship between compaction stress and volume fraction:

$$\bar{\sigma} = a' {V_f}^{b'} \quad \text{Eq. 3-21}$$

where $a'$and b' are the fitting constants. Strain (ϵ) experienced by the fibres were also calculated as a function of compaction stress. The following equation was used to compute the strain from the fibre volume fraction as follows:

$$\epsilon = 1 - \frac{V_{f0}}{V_f} \quad \text{Eq. 3-22}$$

where V_{f0} is the initial fibre volume fraction at the onset of compression. The power law model fit for the compaction stress as a function of volume fraction is shown in Figure 3-30a. The corresponding relationship between the compaction stress and strain is shown in Figure 3-30b.

3.4.2 Wet compaction

3.4.2.1 Experimental setup and procedure

For wet compaction analysis, the fibres were cut and stacked in the same sequence as used for dry compaction tests. The wet samples were prepared by placing the fibres on metallic mesh and soaking the fibre stacks in Xiameter PMX-200 Silicone oil 100 CS testing fluid for 15 minutes. Care was taken to make sure the fibres were fully immersed. The fabric stack was removed from the oil bath and drained horizontally on the grid for 20 minutes. At this stage, the fibres were placed in the mould and the same procedure was followed as in the case of dry compaction. Sealant tape and an oil absorbing cloth were attached on the sides of the mould to contain and absorb any overflowing of silicone oil during compaction. Load-unload method was again used, and the load displacement data were recorded.

3.4.2.2 Results

The steps mentioned in the previous section for dry compaction were followed to calculate the compaction pressure and the volume fraction from the recorded load displacement curve. Volume fraction was calculated using Eq. 3-16 and the compaction pressure was calculated using Eq. 3-18. A power law model was again used to fit the experimental data and the plot of compaction pressure and volume fraction is shown in Figure 3-31a. The strain was calculated using Eq. 3-20

and the plot of compaction pressure and strain is shown in Figure 3-31b. The power law fitting constants are listed in Table 3-13. A comparison between both dry and wet compaction result is shown in Figure 3-32.

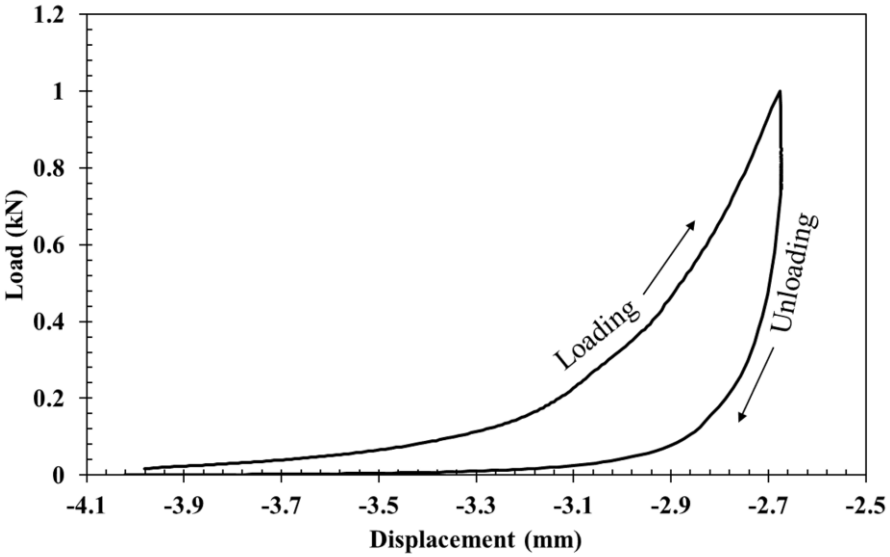

Figure 3-28: Load-unload displacement curve for dry NCF.

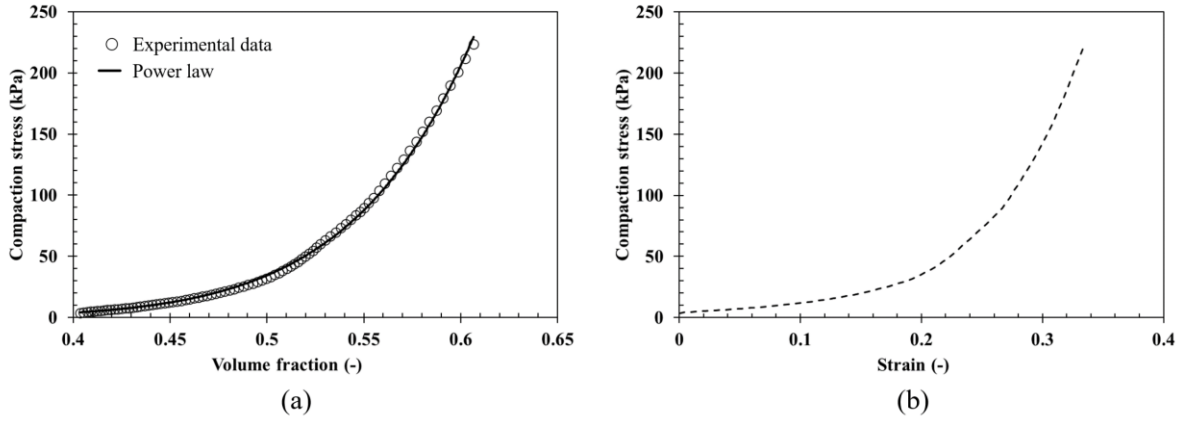

Figure 3-30: a) Compaction stress versus the volume fraction experimental data and the power law model fit for dry compaction. (b) Compaction stress as function of strain.

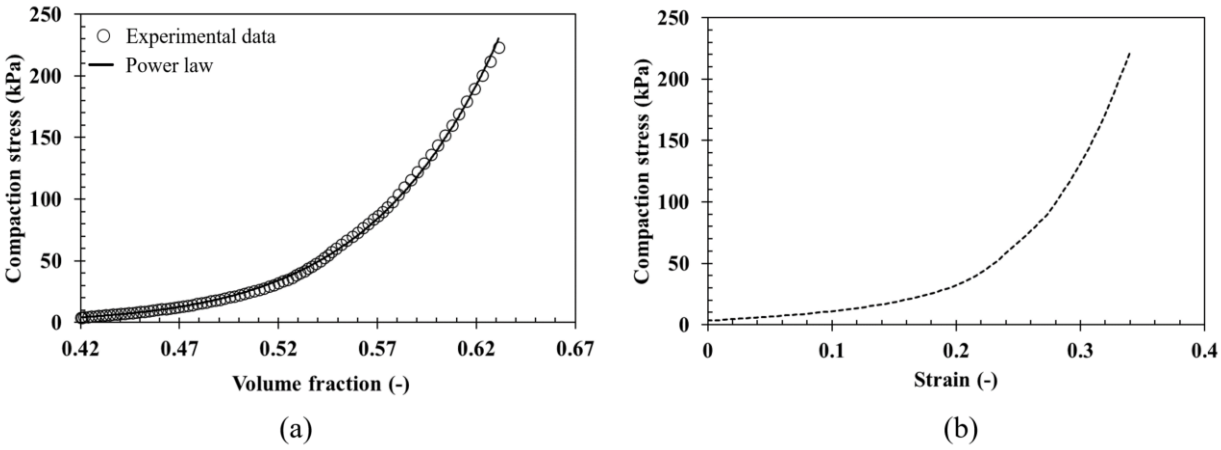

Figure 3-29: a) Compaction stress versus the volume fraction experimental data and the power law model fit for wet compaction. (b) Compaction stress as function of strain.

Table 3-13: Power law fitting parameters for both dry and wet compaction models.

Compaction	a'(MPa)	b'
Dry	31.00	9.81
Wet	21.32	9.85

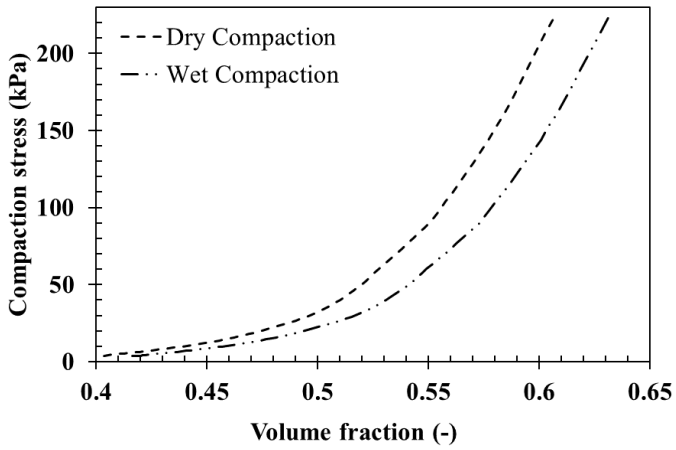

Figure 3-30: Comparison of dry and wet compaction versus volume fraction showing the effect of lubrication.

3.4 Summary and discussion

This chapter presents a comprehensive methodology to characterize the thermochemical properties of fast curing thermosetting resins and the physical properties of a glass NCF. Five commercial thermosetting resins were studied in this work and material models were developed using semi-empirical equations with an average R^2 value of greater than 0.80. The characterization techniques used for the measurement of permeability and compaction of TG15N glass NCF was explained, and a material model fit was developed reported.

***Cure kinetics*:** Arrhenius based models were developed for all five fast curing resins studied in this work. A critical temperature was defined for all the epoxy resin systems beyond which the fitting parameters increased linearly. Therefore, a logistic function was defined to consider this behaviour. For the polyester resin, the effect of inhibitor was considered by introducing an inhibition term to accurately capture this effect. The evolution of the glass transition temperature was also captured with a sequence of dynamic and isothermal temperature cycles and a good fit for the experimental data was obtained using the Di-Benedetto equation.

***Viscosity*:** A temperature and degree of cure dependent model was developed to capture the evolution of viscosity for all the resins studied in this work. The model is very simple with a minimum number of fitting constants. Furthermore, the model used for polyester resin was able to capture the effect of inhibitor successfully.

Permeability: In-plane (K_1, K_2) and transverse (K_3) permeability of TG15N glass NCF was measured for three volume fractions ranging between 0.39 and 0.63. The equipment used for measuring the permeability was designed in-house in the laboratory and the techniques used for measuring were based on the well-established benchmarking exercises for both in-plane and transverse permeability measurement. The results indicated a decrease in permeability with an increase in fibre volume fraction, a typical behaviour for fibre reinforcements showing consistency of the material behaviour in different orientations. Furthermore, K_2 was slightly higher than K_1 due to the additional presence of the stitch being in the warp direction causing additional resistance to flow. Power law and modified Kozeny-Carman equations provided similar fit for the experimental permeability data.

Compaction: Dry and wet compaction experiments were performed on TG15N glass NCF using a custom-built testing jig attached to a testing machine. A power law model was applied to both sets of experimental data. The results revealed that the final volume fraction for the same compaction pressure in wet compaction tests was approximately 0.03 higher than in dry compaction tests, a typical observation for the fibre reinforcement due to the lubrication effect. Wet compaction data will be preferred over dry compaction while modelling the CRTM process since it reflects the conditions of the infusion of resin and compression stages of the process.

The material models developed in this chapter are a prerequisite for the modelling of liquid injection moulding processes like CRTM. Extremely simple models were developed for highly complex materials with minimum number of fitting constants. These models can be easily implemented in state-of-the-art finite element tools like PAM-RTM, COMSOL Multiphysics and OPENFOAM. The models developed in this chapter can be implemented to solve fully coupled heat transfer, cure, flow, and compaction problems or optimize processing parameters.

CHAPTER 4

4. CRTM Simulation and Experimental Setup

This chapter discusses the details of the numerical and experimental setup of the CRTM process using fast curing resins. First, the numerical methodology and framework used in PAM-RTM are presented. Second, the experimental setup used to manufacture a simple 3D flat plaque geometry is discussed. Third, the experimental setup was analyzed using the Finite Element based tool PAM-RTM to solve the 3D CRTM process, and the results are validated.

4.1 Methodology

4.1.1 Governing equations used in PAM-RTM

PAM-RTM uses Darcy's law combined with conservation of mass to govern the flow of resin through fibrous reinforcement. The equation was given as follows:

$$\nabla \cdot \left(-\frac{\overline{\overline{K}}}{\eta} \cdot \nabla \mathrm{P} \right) = 0 \qquad \text{Eq. 4-1}$$

PAM-RTM uses non-conforming FE formulation and the fill factor associated with each element was used to track the flow front of the resin. The fill factor F associated with each element was given by the following equation [140]:

$$F = \frac{V_r}{V_e . \emptyset} \qquad \text{Eq. 4-2}$$

here V_r and V_e represent the volume of the resin and individual element respectively. The value of F ranges from 0 to 1, indicating the level of saturation in each element.

When fast curing resins are used, a significant amount of heat transfer takes place between mould, resin, and the fibre in the form of conduction, convection, and exothermic chemical reactions. This problem was solved using the local thermal equilibrium (LTE) equation based on the first law of thermodynamics [9]:

$$\rho_c C_{pc} \frac{\partial T}{\partial t} + \rho_r C_{pr}(\vec{v} \cdot \nabla T) = \nabla \cdot \left(\bar{\bar{k}} \nabla T\right) + \emptyset \rho_r H_{tot} \frac{\partial \alpha}{\partial t} \quad \text{Eq. 4-3}$$

The conservation of mass of the highly reactive resin is governed by chemical species transport equation or the advection equation expressed as:

$$\frac{\partial \alpha}{\partial t} + \vec{v} \cdot \nabla \alpha = R_\alpha \quad \text{Eq. 4-4}$$

The fibre reinforcement was considered a deformable medium. A significant change in porosity is caused due to the large stresses and strains experienced by the reinforcement during injection and compression phase. This was described using conservation of momentum [111]:

$$\nabla \cdot \bar{\bar{\sigma}}(\vec{u}) = \overrightarrow{f_B} \quad \text{Eq. 4-5}$$

where $\bar{\bar{\sigma}}$ is the Cauchy's stress tensor, $\vec{u}$ is the displacement vector and $\overrightarrow{f_B}$ is the body force vector. The porous domain was represented as an orthotropic homogenous medium composed of rigid fibres. A Lagrangian Formulation was used [141]:

$$J(\vec{x}, t + \Delta t)\big(1 - \emptyset(\vec{x}, t + \Delta t)\big) = J(\vec{x}, t)(1 - \emptyset(\vec{x}, t)) \quad \text{Eq. 4-6}$$

Terzaghi's effective stress theory used in soil mechanics was used for coupling fibre compaction pressure and resin pressure:

$$\bar{\bar{\sigma}}_{overall} = \bar{\bar{\sigma}}_f + P\bar{\bar{I}} \quad \text{Eq. 4-7}$$

where $\bar{\bar{\sigma}}_{overall}$ is the overall stress exerted (Pa), $\bar{\bar{\sigma}}_f$ is the stress generated on the fibre (Pa) and $\bar{\bar{I}}$ is the unit tensor.

4.1.2 Numerical framework

PAM-RTM version 2020.5 was chosen to be used for this study [142]. A new approach called the fluid-solid coupled approach was introduced into this solver [113]. The resin flow (Eq. 4-1 and Eq. 4-2), heat transfer (Eq. 4-3) and chemical species transport (Eq. 4-4) are solved in the fluid mechanics solver of PAM-RTM on a fixed grid. The pressure output from the fluid solver is

transferred to the solid mechanics solver to solve the non-linear solid problem (Eq. 4-5) that follows the concept of Terzaghi's relationship (Eq. 4-7). The displacement results are transferred back to the fluid mechanics solver with the permeability and the deformed geometry being updated for the next time step. The time interval for the data transfer between the two solvers can be chosen and it is referred to as coupling frequency.

PAM-RTM software package comes with a graphical user interface (GUI) called Visual Environment. For the solver version 2020.5, Visual Environment 16.0 was used as the GUI. The solver also allows the use of user-defined function (UDF) subroutines to implement custom resin material models. The UDF was only compatible with C language and the C compiler had to be compatible with Visual Environment. Therefore, the resin cure kinetics and viscosity models were written in Visual Studio version 2017 which was compatible with Visual Environment 16.0. The fibre permeability was implemented as a function of volume fraction in the form of a table graph. Similarly, compaction stress response of the fibre was implemented as a function of strain in the form of a table graph. The working of the process model is shown in Figure 4-1.

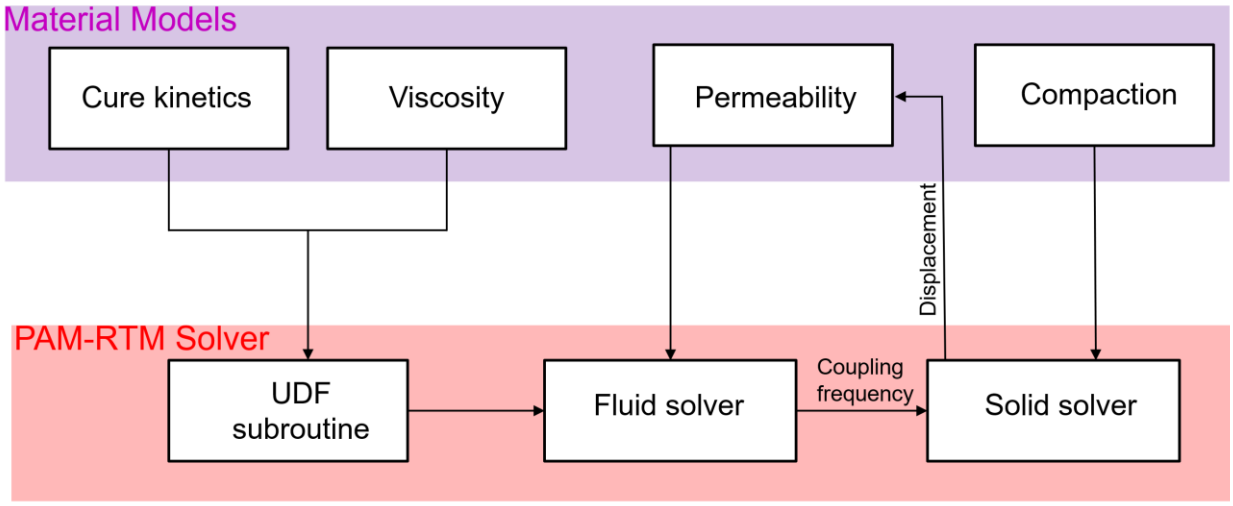

Figure 4-1: The fluid-solid coupling approach used in PAM-RTM to solve resin injection-compression phase along with user-defined function subroutines to implement resin material models.

In this study, a multistage computational approach was used to link preheating, resin injection-compression, and curing simulations. The material properties and initial and boundary conditions were initialized, and the first step involved the preheating simulation. The results from the preheating simulation were used as an initial condition to perform the injection-compression simulation subsequently. Similarly, the results obtained form this step were used as an initial condition to perform curing simulation. The link between the steps was made in PAM-RTM using the extract/mapping feature, which maps the values of the corresponding nodes to the next simulation step. The flow chart describing this approach is shown in Figure 4-2.

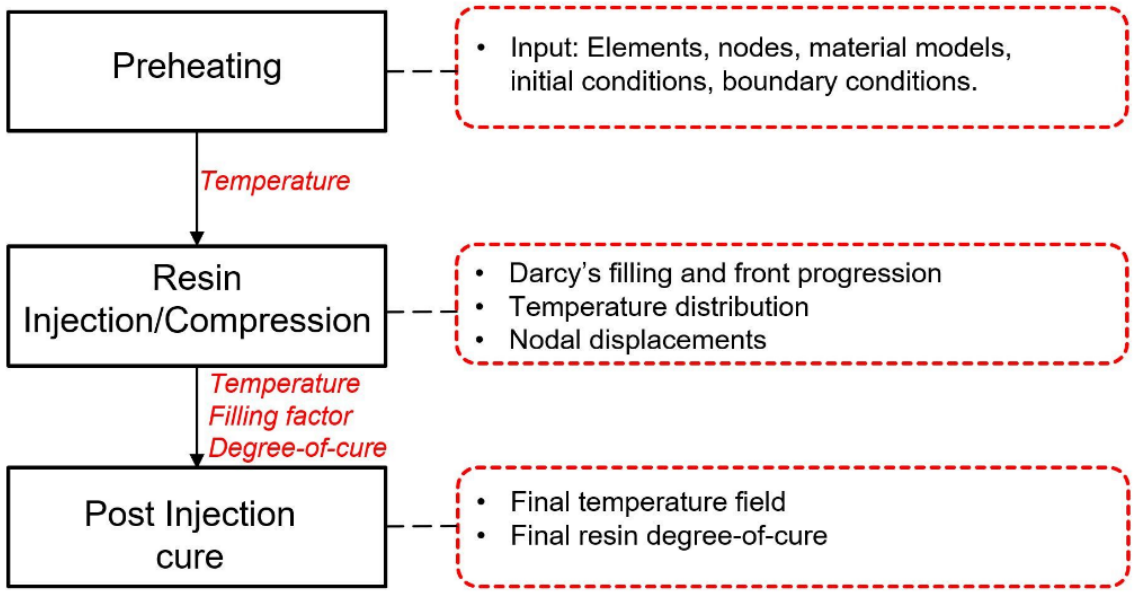

Figure 4-2: Multistage CRTM process simulation flow diagram.

4.2 Experimental setup and materials

4.2.1 Equipment description

The experimental setup was made from a P20 steel plaque tool as shown in Figure 4-3. The flat plate tool was installed on a 1250-ton press from Pinette Emidecau Industries (PEI). The National Research Council Canada (NRC) designed the tool to make parts with dimensions of 350 mm x 350 mm and a range of 1-10 mm thickness. The perimeter of the bottom mould was elevated by a

thickness of 0.65 mm (shown using black lines in Figure 4-3) to help keep the preform in place during the injection-compression phases of the CRTM process. This region is called the pinch area and has a width of 20 mm. The resin injection gate was located at the centre of the bottom mould.

Two GEFRAM WE26-M-P03M pressure and temperature transducers with built-in thermocouple were placed within the tool bottom surface at strategic locations as shown in Figure 4-4. Sensor 1 was located close to the injection gate, and sensor 2 was located near the vent. Online data monitoring was developed using NI DAQ system and a LabVIEW code was developed to capture the entire temperature and pressure history of the CRTM process from preheating to demoulding of the part.

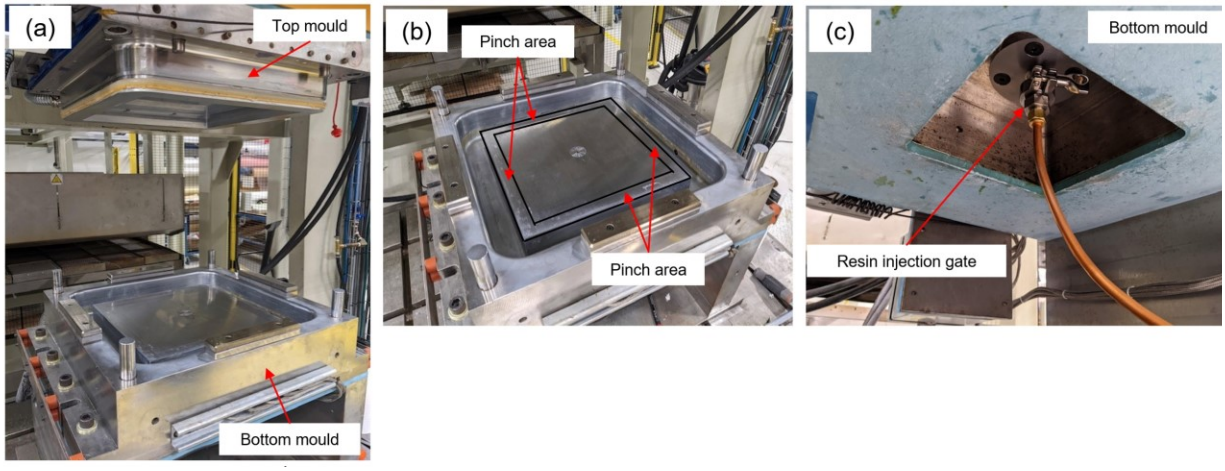

Figure 4-3: (a) The CRTM mould setup installed in the 1250 ton press, (b) The bottom mould showing slightly elevated perimeter designed for holding the preform in place with a width of 20 mm as highlighted using black line, and (c) bottom gate resin injection setup (Right).

4.2.2 Material description

Due to the large quantity of resin readily available for further analysis and experimental work, Gurit standard resin was chosen to make parts and validation experiments. The resin system used in this study consisted of one part epoxy and one part hardener, mixed in the ratio 100:25 by weight. Glass NCF from Texonic Inc. was used in this study. Each layer of fabric had a thickness of 0.45 mm and an areal density of 518 g/m^2. Eight layers of fibres were stacked on top of each other with a layup sequence $[(0/90)]_{4S}$, where S stands for symmetric. A template was drawn with

the dimensions 350 mm x 350 mm using a marker. A utility blade was used to cut to the required dimension and the final part obtained is shown in Figure 4-5. An Epikote 06720 thermoplastic polyester binder was applied between the plies. The preform was vacuum bagged and placed in an oven for 15 minutes at 100 ºC to activate the binder.

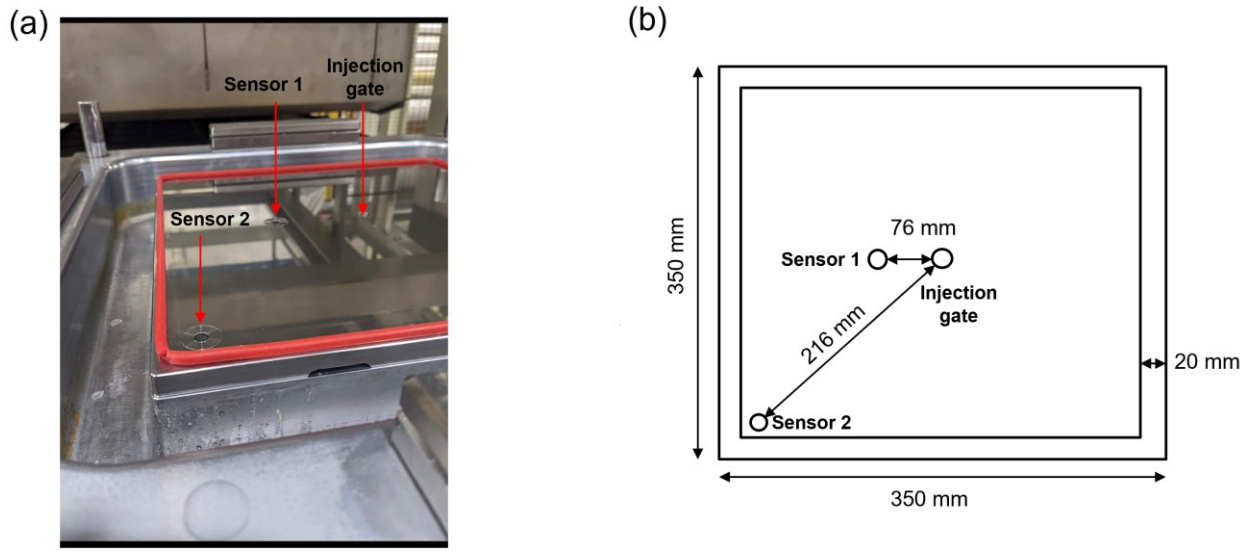

Figure 4-4: (a) Location of sensors on the bottom mould, and (b) the schematic of the top view showing the exact location of the sensors (Right).

4.2.3 Procedure

The initial step involved the preheating of the mould to a temperature of 100ºC. The preform was placed on the preheated mould, and the top mould was moved until there was a gap of 4 mm between the surface of the bottom mould and the top mould. The thickness of the preform was 3.35 mm, and therefore, an air gap of 0.65 mm was present between the top surface of the preform and the top mould surface. A premixed resin and hardener mixture was pressurised in a pressure pot and injected through the injection gate. The injection gate was closed when 350 g of resin was injected, and the compression sequence was initiated. The top mould moved in the downward

direction at a rate of 0.5 mm/s, compressing the preform to a final thickness of 3mm and achieving full impregnation.

Figure 4-5: TG15N glass NCF after the activation of binder.

CRTM is a closed mould process and hence in situ visualization of resin flow front is not possible. To overcome this issue, interrupted filling tests (short shots) were performed. The inherently fast curing nature of the resin caused the flow front to cease within a minute of discontinuing the resin injection due to a sharp rise in viscosity. Eventually, a clearly defined flow front was obtained. The following test matrix was defined for interrupted filling tests as shown in Table 4-1.

Table 4-1: Interrupted filling test matrix

Test No.	**Time (sec)**
1	5
2	30
3	60 (End of injection)
4	61.23 (End of compression)

4.3 Simulation setup

4.3.1 Geometry definition

The dimensions of the geometry based on the CRTM equipment are shown in Figure 4-6. Since the injection gate is located at the centre of the bottom mould of a square geometry, symmetry allowed us to simulate only one-eighth of the geometry as shown in Figure 4-6. In the model, the transition from the central main surface to the tool pinch area, which typically is an inclined surface, was simplified to a step transition on an already deformed reinforcement.

The CAD features available in PAM-RTM were used to build the 3D model of the one-eighth section as shown in Figure 4-7. The top and the bottom mould were 10 mm thick, and the were made slightly wider to accommodate possible deformations because of the compression sequence. The preform was divided into two regions: (i) the central region (orange), and (ii) the pinch region (light green).

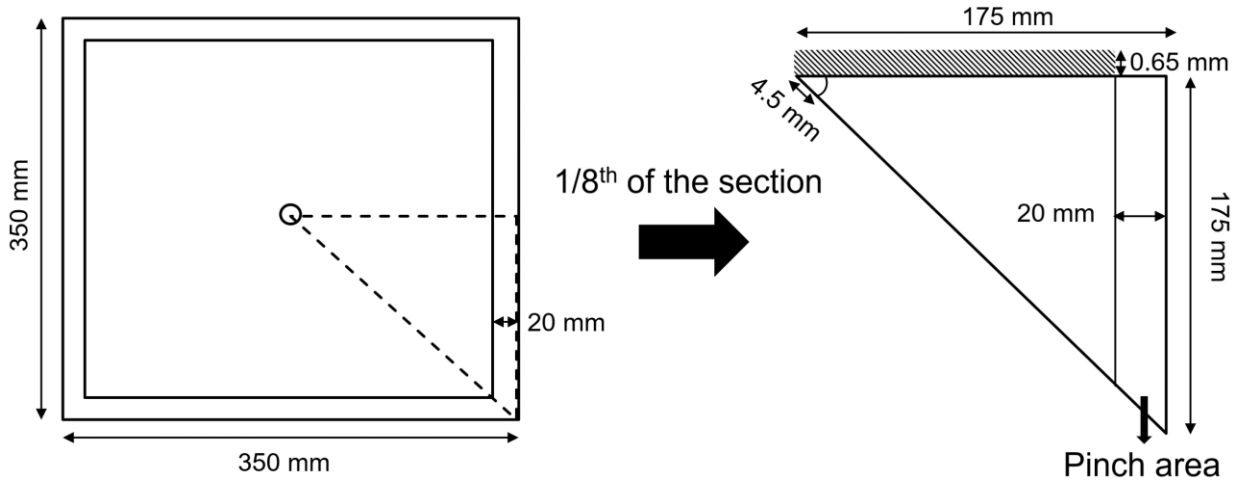

Figure 4-6: Schematic of the full geometry form top view and the corresponding 1/8th section of the geometry.

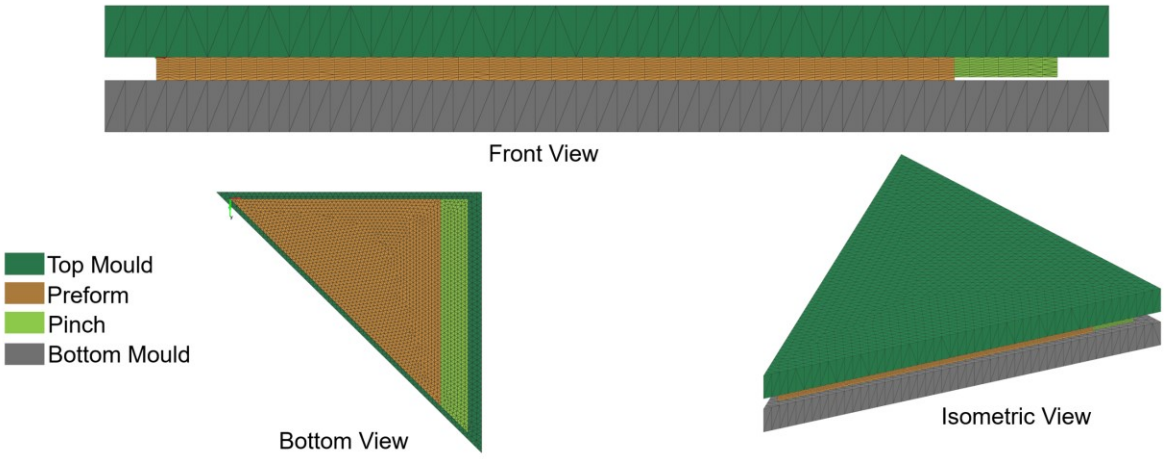

Figure 4-7: Meshed geometry as seen in PAM-RTM with three different views showing the 1/8th geometry of the mould and preform including the pinch area.

A 3D tetrahedral mesh was used to model the preform, pinch and mould sections. A total of 160,357 linear elements were used in the model. The PC used in this work had an Intel® Core™ i7-4770 CPU with four cores. The initial and boundary conditions used in the simulation are mentioned in Table 4-2. The injection, vent, and initial mould temperature boundary conditions are shown in Figure 4-8.

4.3.2 Model assumption

In this work, we used the CRTM-2 setup (as shown in Figure 1-3 in Chapter 1) where the resin was injected directly into the preform rather than into the gap like the CRTM-1 setup. As the resin is injected into the preform, the decompression effect [91] can cause the thickening of the preform which makes the modelling process complicated. To streamline the modelling process, an assumption was made that the preform occupied the entire cavity inside the mould during resin injection. Therefore, the initial thickness of the preform was considered as 4 mm (fully occupying the cavity) instead of 3.35 mm (actual preform thickness), and the initial volume fraction was adjusted to 0.41 from 0.47 respectively. A schematic illustration of the assumption made is shown

in Figure 4-9. To check for the effect of decompression, a model was defined in PAM-RTM to include the gap with zero porosity. The front view of the model is described in Figure 4-10.

Table 4-2: Material properties of Gurit standard resin and TG15N NCF and process parameters

Cure kinetics	
$A_1 = -53090\ s^{-1}$	Pre-exponential factor 1
$E_1 = 52160\ J/mol$	Activation energy 1
$A_2 = 12280\ s^{-1}$	Pre-exponential factor 2
$E_2 = 43750\ J/mol$	Activation energy 2
$H_T = 440\ J/g$	Total heat of reaction
$m, n = 0.10, 1.69$	Exponents
$C, \alpha_{co} = 200, 0.911$	Diffusion parameters
Rheology	
$A_{\boldsymbol{\mu}} = 1.68 * 10^{-6}\ Pa.s$	Pre-exponential factor
$E_\mu = 31780\ J/mol$	Activation energy
$\alpha_g = 0.78$	Degree-of-cure at gel point
$a, b = 0.8, 4.50$	Exponents
Heat transfer properties	
$\rho_r, \rho_f, \rho_m = 1180, 2600, 7800\ kg/m^3$	Density
$C_{pr}, C_{pf}, C_{pm} = 1500, 800, 515\ J/(kg.K)$	Specific heat
$k_r, k_f, k_m = 0.2, 1.2, 50\ W/(m.K)$	Thermal conductivity
Process parameters	
$V_{\boldsymbol{f01}} = 0.402$	Initial preform volume fraction
$V_{\boldsymbol{f02}} = 0.482$	Initial pinch volume fraction
$U = 1\ mm/s$	Mould closing speed
$T_{inj} = 20\ °C$	Resin injection temperature
$T_{um}, T_{lm} = 100, 100\ °C$	Upper and lower mould temperatures
$T_{amb} = 22\ °C$	Ambient room temperature
$P_{inj}, P_{vent} = 550, -100\ kPa$	Resin injection and vent pressure
$HTC = 480\ W/(m^2.K)$	Heat transfer coefficient
$e = 2 * 10^{-4}\ m$	Interface thickness

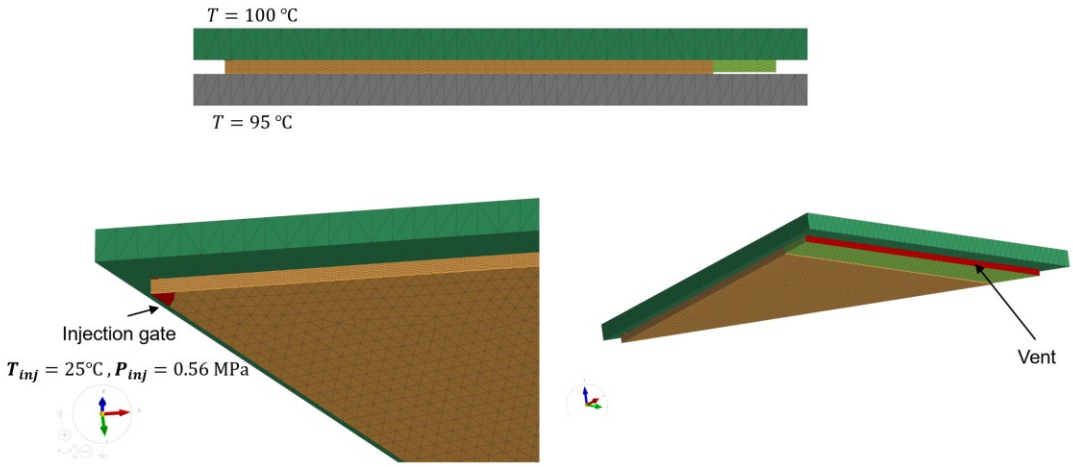

Figure 4-8: An overview of the initial and boundary conditions implemented in PAM-RTM.

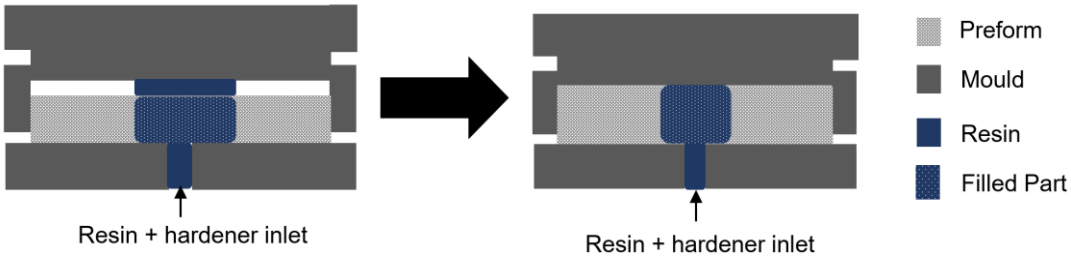

Figure 4-9: Schematic of the assumption made during the modelling of the CRTM process: (i) Resin injection with the inclusion of the gap (Left), and (ii) resin injection considering preform expansion with the elimination of the gap (right).

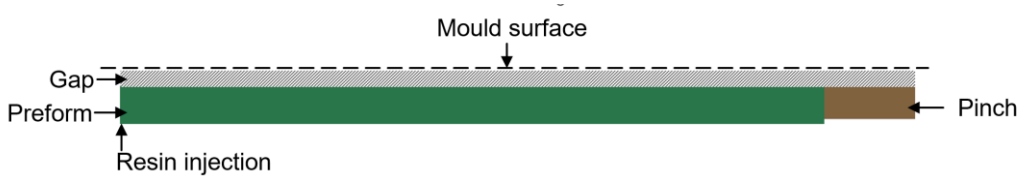

Figure 4-10: Front view of the geometry of the 1/8th section the model with the inclusion of the gap to check for preform decompression

The heat transfer between the mould and the preform was defined by a heat transfer coefficient (HTC). The assumption was made that the contact between the preform and the mould was never perfect, and a small layer of air was present in this gap. Therefore, an HTC (W/m^{2}K) was defined as:

$$HTC = \frac{k_a}{e} \qquad \text{Eq. 4-8}$$

where k_a is the thermal conductivity of the air in W/mK, e is the interface thickness in m, T_1 and T_2 are the mould and preform temperature respectively in ºC. The schematic representation of the heat transfer is shown in Figure 4-11.

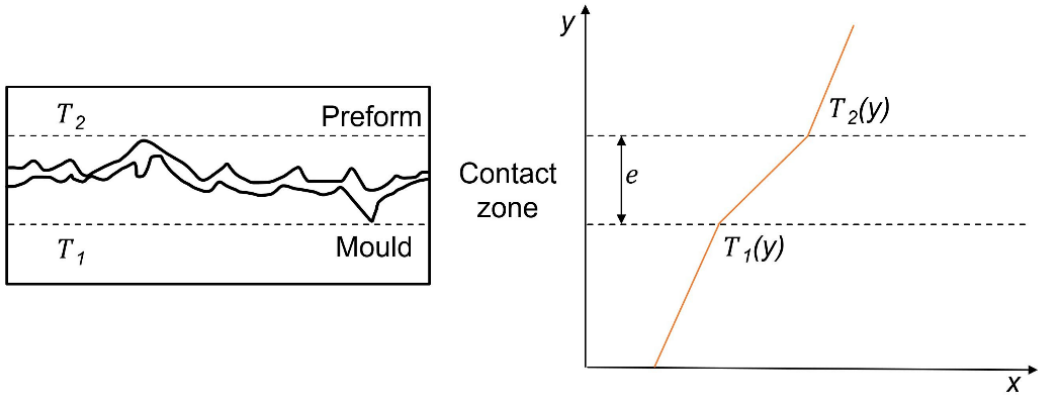

Figure 4-11: HTC assumption between the mould and the preform surface.

4.4 Simulation and experimental results

4.4.1 Preform Decompression

The first step involved the confirmation of the assumption's validity shown in Figure 4-9. The fluid-solid coupled flow simulation demonstrated the progressive decompression of the preform as the flow front of the resin progressed. The progression of the resin eliminated the predefined gap as shown in Figure 4-12. Unfortunately, full convergence of the simulation was not achieved as a result of gap elements' intrusion into the preform as the resin was injected [110]. This showed the expansion of the preform as the resin progressed covering the entire gap section. Therefore, by

proceeding with the simplified assumption made in Figure 4-9, the model still captures the key dynamics of the resin flow and preform compaction, The assumption enables us to proceed with the simulation, albeit with a simplified representation..

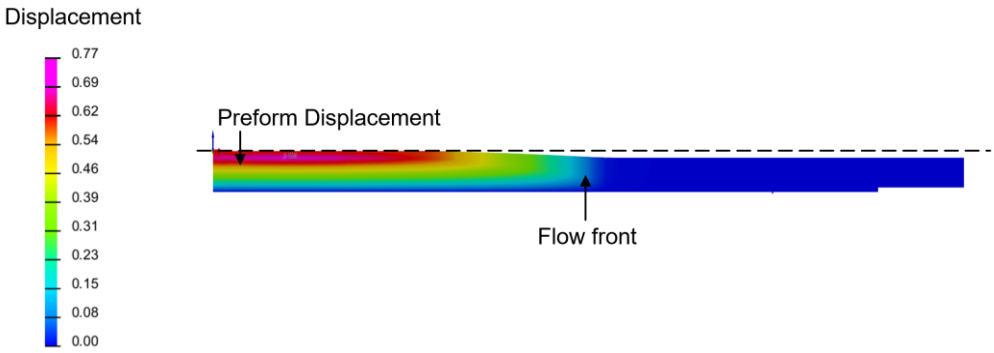

Figure 4-12: The results showing the effect of decompression of the preform (displacement in mm) with the progression of the resin flow front.

4.4.2 Interrupted flow analysis

The experiments and simulations were performed based on the test matrix defined in Table 4-1. The first shot of the resin was injected for five seconds, and the injection gate was closed. The stopped flow front distance from the injection gate was measured and compared with the corresponding simulation results, as shown in Figure 4-13a. A comparison was made for the distance traveled by the flow front from the injection point along both the x-direction and the diagonal of the x-y plane. The experimental flow front was stopped at 71 mm from the injection gate. A distance of 67 mm was predicted using the simulation showing 95% accuracy. Similarly, the results were compared for 30 and 60 seconds and accuracies of 91% and 94% were obtained, respectively. All the results of the comparison between experiment and simulation with fill factor are shown in Figure 4-13a-c. The simulation results are in good agreement (greater than 90% match between the flow front distance) with the experimental results. Furthermore, the deviation of the flow front direction from the preform to the pinch section was accurately captured by the simulation, as shown in Figure 4-14. The deviation of the flow front was caused by a sudden increase in volume fraction of the pinch area (lower thickness) compared to the rest of the preform

area. To represent the comparison between experiment and simulation, the diagonal flow front distance was plotted against time highlighting the close agreement, as shown in Figure 4-15. Similarly, the amount of resin injected was also compared with the simulation results showing excellent validation in Figure 4-16.

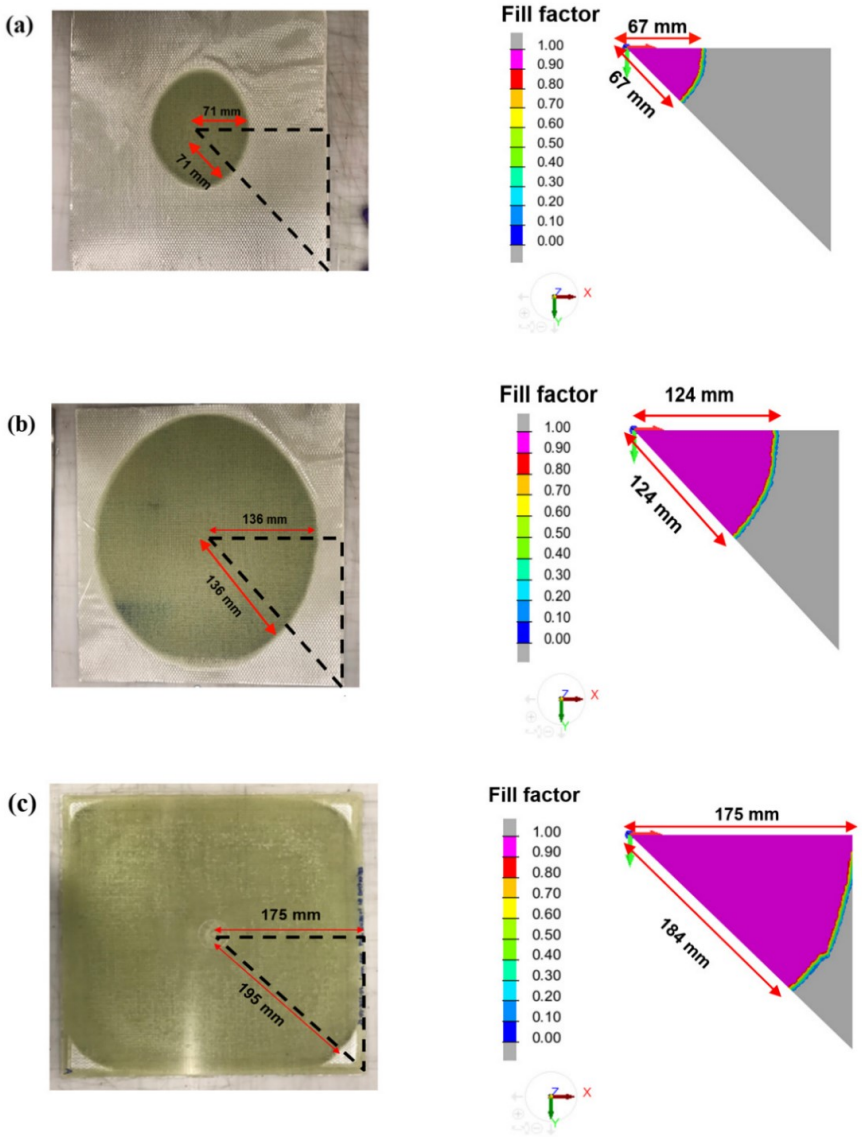

Figure 4-13: Interrupted flow experiment and the corresponding simulation results at different time intervals with fill factor: (a) 5 seconds, (b) 30 seconds, and (c) 60 seconds (end of injection).

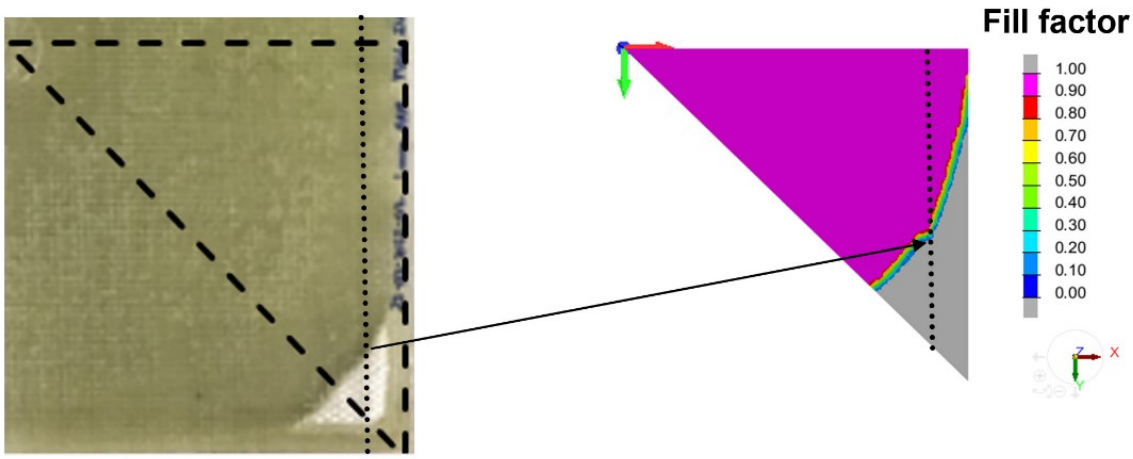

Figure 4-14: The deviation observed at the transition between the preform and the pinch section at the end of the injection phase captured successfully by simulation.

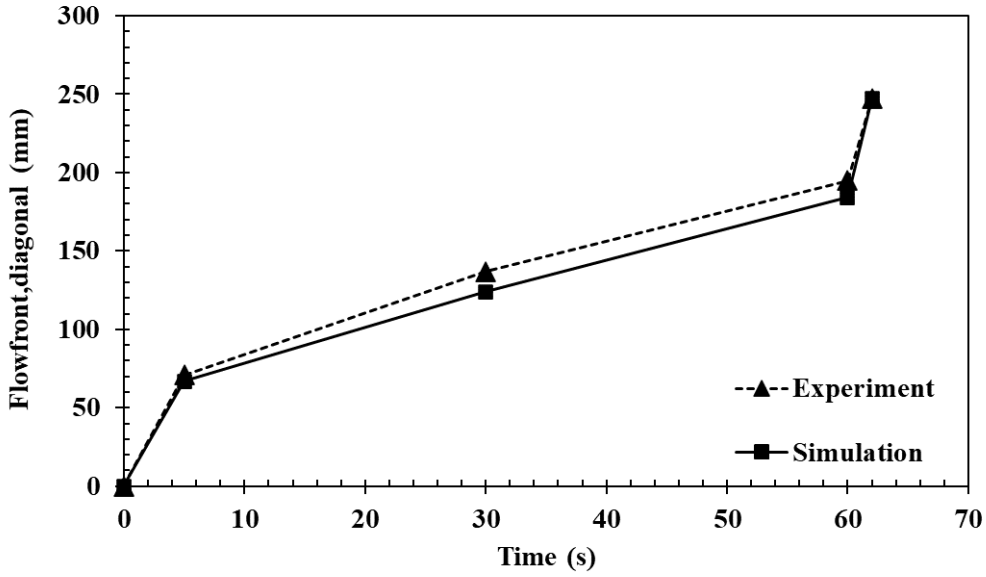

Figure 4-14: Flow front distance comparison in the diagonal of the x-y plane.

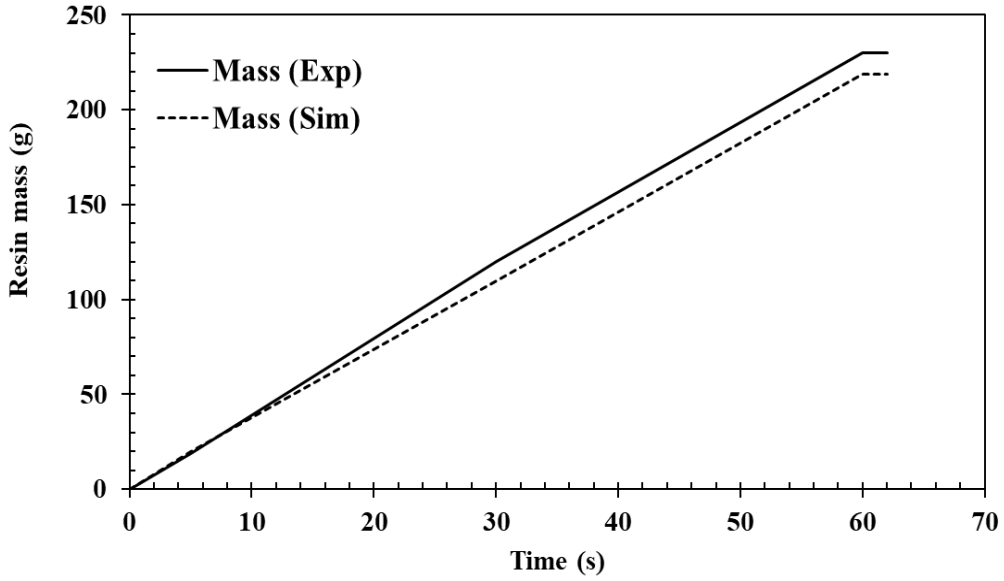

Figure 4-15: Comparison between experiment and simulation of resin injected into the mould.

4.4.3 Sensor analysis

The data for the entire process was captured, from preform placement until the demoulding step. Figure 4-17 shows the recorded temperature and pressure histories for the entire process. The initial placement of the cold preform on the preheated mould caused a slight decrease in temperature reading on both sensors by approximately 2 ºC, as observed at point 2 on the plot. When the vacuum was turned on, a decrease in pressure was seen at point 2 from 0 to -100 kPa. Once the desired temperature was achieved by the mould, the premixed resin and hardener mixture (20 ºC) was injected through the injection gate at point 3. A noticeable drop in temperature was captured by sensor 1, which was observed at point 4 as the resin front passed through it. At the end of the injection phase, the compression of the top mould was activated, resulting in a huge spike in pressure readings on both sensors. An approximate reading of 9000 kPa was recorded by both sensors, as shown in point 5. At this point, the mould was closed for ten minutes, allowing the resin to cure. An increase in temperature was observed in the readings of both sensors as illustrated in region 6, owing to the heat released by the exothermic reaction of the resin.

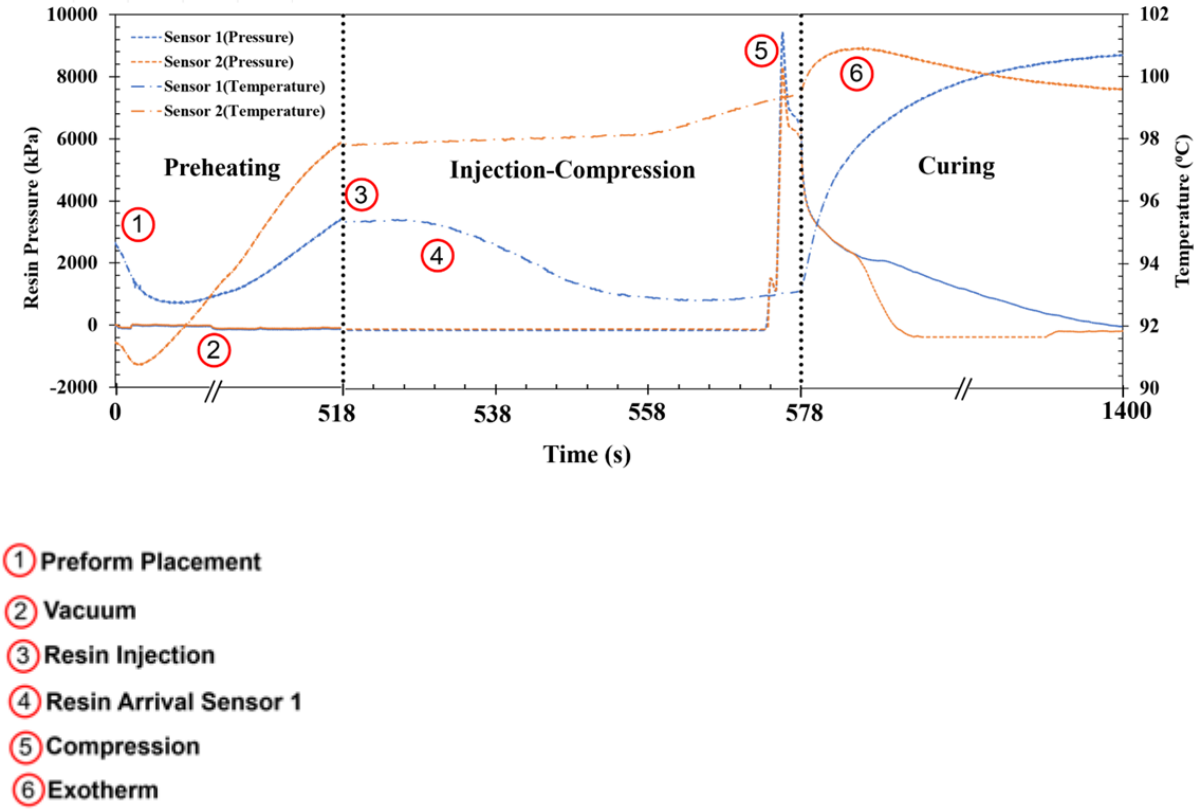

Figure 4-16: Temperature and pressure profile recording by the sensors for the entire CRTM process. The scale of the x-axis has been segmented to show the injection-compression phase.

To validate the temperature and pressure data obtained from the sensors, virtual sensor functionality available in PAM-RTM was used. These sensors were positioned at the same locations as the actual sensors, as illustrated in Figure 4-18. A greater emphasis was placed on the injection-compression phase and post-compression curing phase as the preform attained the set temperature of the mould. Firstly, the measured temperature data at the injection-compression region was compared with the virtual sensor simulation data. The results are shown in Figure 4-19, showing the decrease in temperature at sensor location 1. The temperature at the sensor 2 remained constant since the resin had already gathered the heat from the mould and the preform, which was captured by the virtual sensor. Similarly, the sensor results from the curing phase were also analyzed. The nodal temperatures obtained at the end of the injection-compression phase were

set as initial values for the curing phase. The rise in temperature due to the exothermic reaction of the resin was successfully captured by the simulation as shown in Figure 4-20.

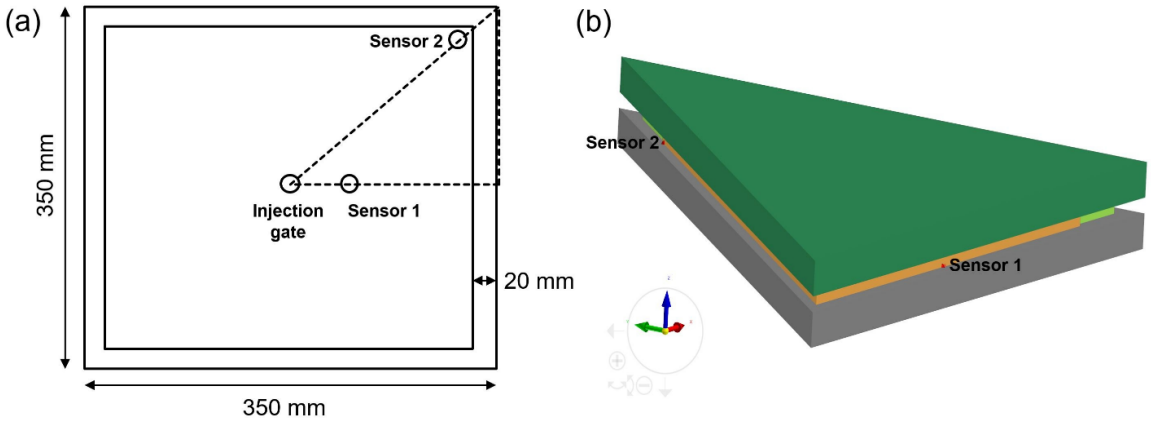

Figure 4-17: (a) Top view of the schematic showing the location of the two sensors. (b) Corresponding locations of the virtual sensor on the model geometry in PAM-RTM.

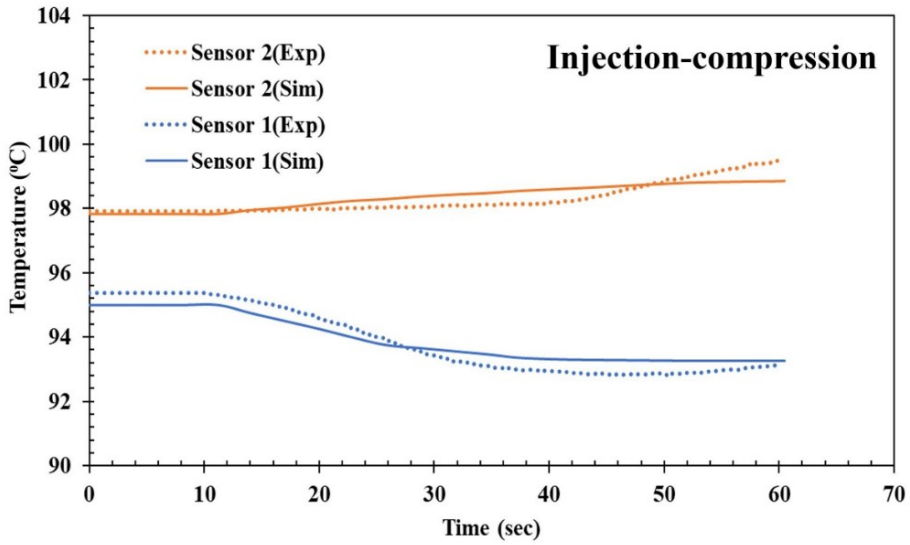

Figure 4-18: Comparison between the experimental and simulation data of temperature for both sensors during injection-compression phase.

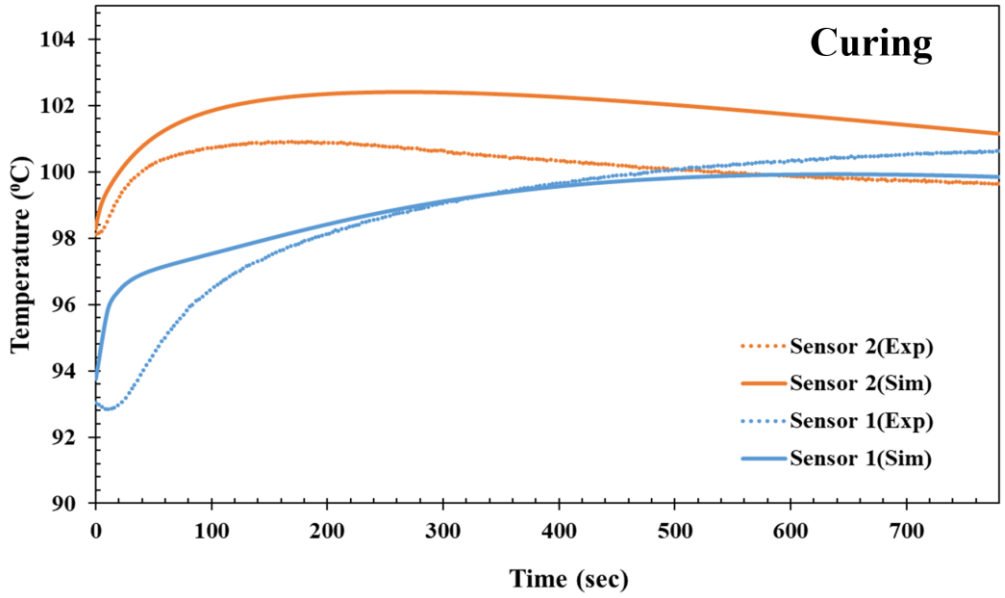

Figure 4-19: Comparison of temperature for both sensors between the experimental and simulation data during curing phase.

The pressure data were also compared between the experimental and simulation results. Figure 4-21 shows the comparison between the experimental and simulation results. A difference of approximately 1400 kPa was seen between the two sensors. However, this difference was consistent for both experimental and simulation results.

4.5 Summary and discussion

In this chapter, a 3D flat plaque geometry was simulated using a fluid-solid coupled approach using PAM-RTM considering all the physical and thermal phenomena: heat transfer, resin flow, resin cure, and fibre compaction during the entire process cycle. The following important conclusions can be drawn:

1) A user-defined subroutine was used to successfully implement the curing kinetics and viscosity material model of a fast-curing Gurit Standard resin on PAM-RTM.
2) A modelling approach was used here, where the preform was assumed to be fully occupying the mould cavity. By calculating an equivalent lower volume fraction than the actual volume fraction of the preform, the experimental results of the flow front

development of resin were successfully captured by the simulation through a series of interrupted flow tests with an agreement of greater than 90%.

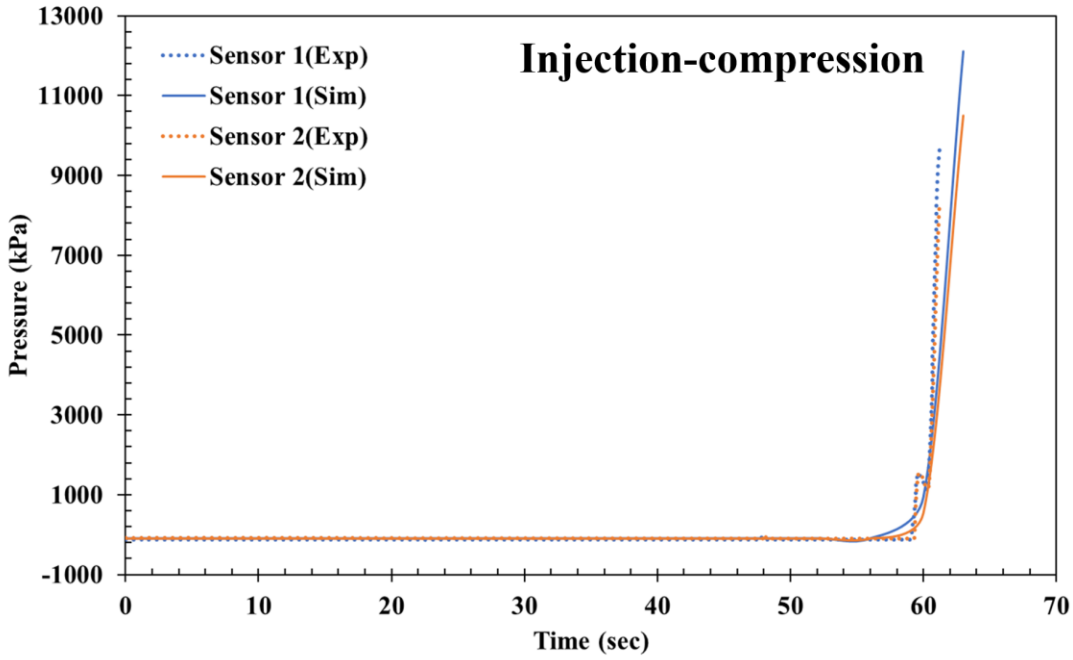

Figure 4-20: Comparison between simulation and experimental data of pressure during the injection-compression phase.

3) The pinch area of the mould was modelled as a separate domain with a higher volume fraction and lesser thickness compared to the rest of the preform. This approach helped to successfully capture the deviation of the flow front as the resin entered the pinch area.
4) Using the approach of defining a heat transfer coefficient between the mould and the preform, the nodal temperature results from the simulation were able to predict the readings from the sensors with good agreement. The simulations were also able to capture the evolution of resin pressure during compression of the mould which was validated with the same sensor results.

A potential reason for the difference between the experimental and simulation results can be attributed to the use of the binder powder in the preforming process. Binder activation at processing temperature (100 ºC) causes its dissolution into the fibre tows, resulting in shrinkage of the fibres

leading to an increase in permeability [143]. Another potential reason for the increase in permeability in the in-plane direction is the interaction between the binder powder and the epoxy resin [144].

Overall, this approach has shown sufficient confidence in manufacturing a simple 3D part using a fast curing resin with the help of simulation.

CHAPTER 5

5. Application: Manufacturing a Complex 3D Demonstrator Part

Vast possibilities exist for replacing parts of long-distance vehicles in the ground transportation industry with composites, as many parts are still made using steel. One such part is passenger-carrying seat in a long-distance coach and replacing this part with composite material can have huge weight savings. Therefore, the objective of this chapter was to simulate the CRTM process for manufacturing a new seat base concept designed by the National Research Council Canada (NRC). In this chapter, the methodology described in the previous chapter (CHAPTER 4) was utilized to manufacture a complex 3D seat base of a long-distance coach. Same fast curing resin and glass NCF models are implemented in PAM-RTM to simulate the CRTM process to manufacture the part. The effectiveness of the simulation is validated using an interrupted flow test. Avenues for faster manufacturing of the part are also investigated.

5.1 Model setup

The manufacture of complex aluminum or steel parts is relatively easy. However, when replacing the corresponding parts with glass or carbon reinforced composites, design and manufacturing can be problematic. One such case studied in this work was the seat base of a long-distance coach. This part was chosen because a normal intercity coach consists of 40 seats (on average) and replacing these seats would considerably reduce the overall weight of the vehicle. The original design consisted of a welded steel assembly. A new design was developed to replicate this welded steel assembly using glass fibre reinforced composite material after finite element analysis. The welded steel assembly and its corresponding composite counterpart are shown in Figure 5.1. Weight analysis was performed on both designs and an approximate 34% weight reduction was obtained. The details are tabulated in Table 5-1.

5.1.1 Model geometry and process conditions

A CAD model of the seat base design was imported to PAM-RTM. A 3D top mould was created using the CAD features available in PAM-RTM. The bottom mould was excluded to significantly reduce computation time. The mould and preform geometry were modelled used 1081518 3D

tetrahedral elements with each face of the tetrahedron being a triangular non-conforming element. The model geometry is as shown in Figure 5-2. The injection gate locations were strategically chosen to reduce the time required for complete infiltration, and the vacuum was applied to the entire perimeter of the part, as shown in Figure 5-3.

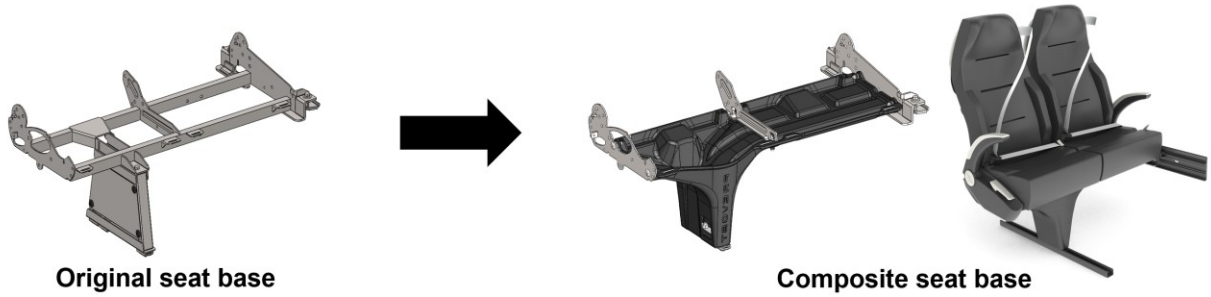

Figure 5-1: Original welded steel assembly design and the corresponding composite design.

Table 5-1: Mass details of the seat base part

Part	Mass (kg)
Welded steel assembly	15.28
Glass fibre reinforced par	10.07

The important initial and boundary conditions are shown in Table 5-2. The cure kinetics and rheology model parameters listed in chapter 4 (Table 4-2) were used as input. A heat transfer coefficient was defined between the two interfaces assuming the contact between the surfaces was not uniform (Section 4.3.2). To obtain more accuracy, constraints were added to the nodes. The mechanical movements of the nodes were restricted in the x and y directions and only allowed in the z direction. The nodal mechanical movements of the bottom surface of the preform were locked in x, y, and z directions. The rest of the nodes of the preform were locked in the in-plane direction. The mechanical locking of the nodes is shown in Figure 5-4. With the assumption used in section 4.3.2, the initial thickness of the preform was kept at 5.4 mm and compressed to 3mm instead of simulating with a gap of 2 mm.

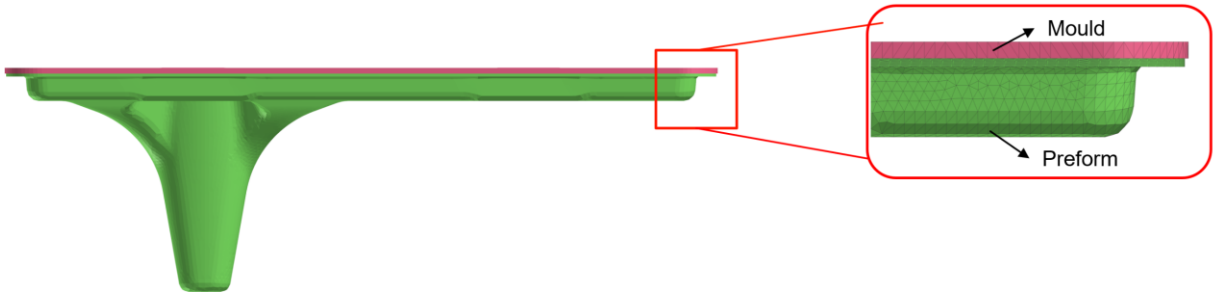

Figure 5-2: 3D model of the mesh mould and preform geometry.

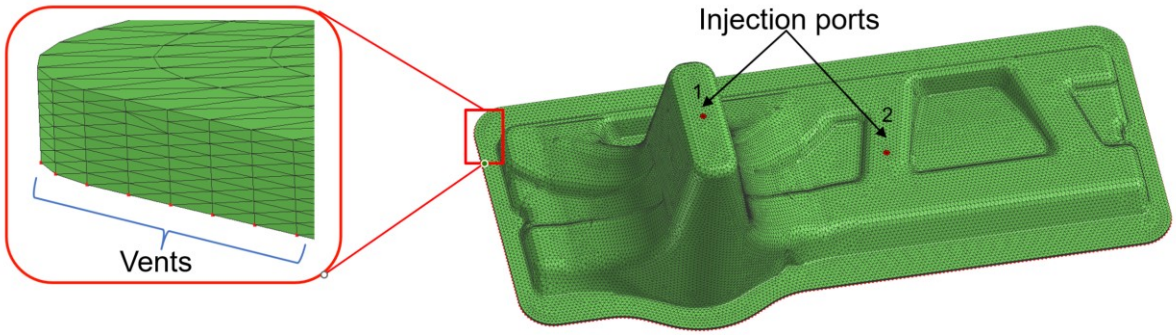

Figure 5-3: The locations of Injection port 1 on the foot of the seat base and port 2 on the horizontal section. The vent shown in the enlarged section (left) covering the entire perimeter of the horizontal section.

Table 5-2: Material and process parameters

Process Parameters	
$V_{f01} = 0.37$	Initial preform volume fraction
$U = 1\ mm/s$	Mould closing speed
$T_{inj} = 25\ °C$	Resin injection temperature
$T_{um}, T_{lm} = 70, 70\ °C$	Upper and lower mould temperatures
$T_{amb} = 22\ °C$	Ambient room temperature
$P_{inj}, P_{vent} = 0.62\ MPa, -0.1\ MPa$	Resin injection and vent pressure

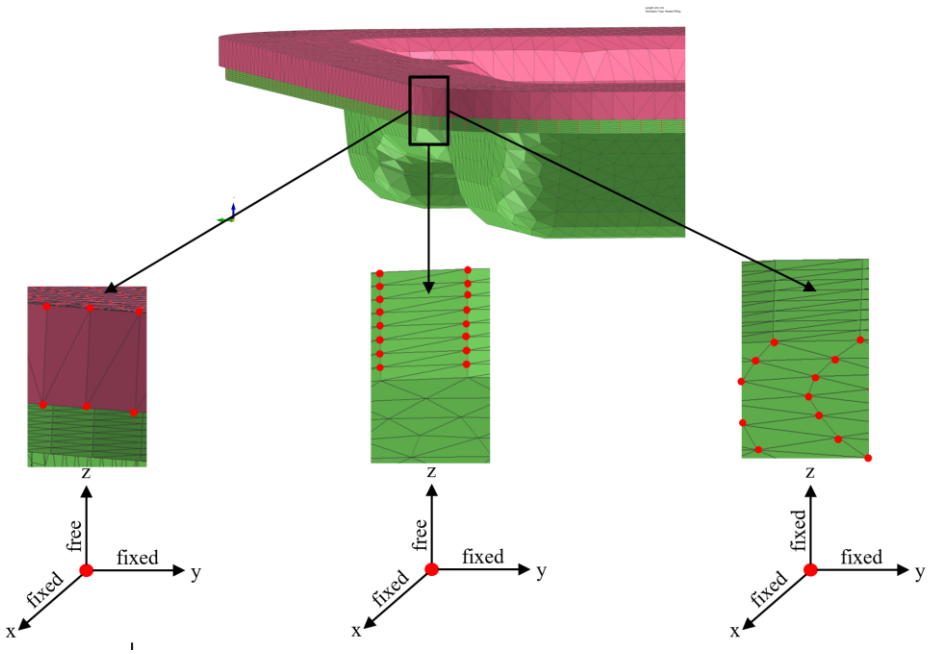

Figure 5-4: Illustration of the mechanical locking applied to all the nodes prior to simulation. (a) The displacement of the nodes of the mould are restricted in the in-plane directions (x and y) and allowed to move in only transverse direction (z). (b) All the nodes of the preform are assigned same conditions as the mould except for the nodes on the bottom surface. (c) The bottom surface nodal displacements are restricted in all directions. The nodes are highlighted as red dots.

5.2 Preforming

The seat base design is complex and intricate; thus, special strategies need to be considered to address multiple concave and convex structures. An innovative three piece preform strategy was developed to aid the preforming of the complex seat base structure. Figure 5-5 illustrates the split design used to make the preform. TG15N glass NCF with a layup sequence of $[(0/90)]_{4S}$ was used. Like the flat plaque structure, Epikote 06720 epoxy thermoplastic binder was applied between each layer of fabric. The fibre stack was vacuum bagged and placed in an oven at 100 ºC for 15 minutes as shown in Figure 5-6. The binder stabilized preform is shown in Figure 5-7. Here, the foot structure was joined in a horizontal manner to reduce wastage during cutting of fibres. For better forming results, a 3D printed seat base preforming plug was designed. Initially the binder stabilized horizontal part was draped on the plug. Next, the horizontally connected foot structure

was cut, and each half was draped vertically on the foot part of the plug. The final draping steps are shown in Figure 5-8.

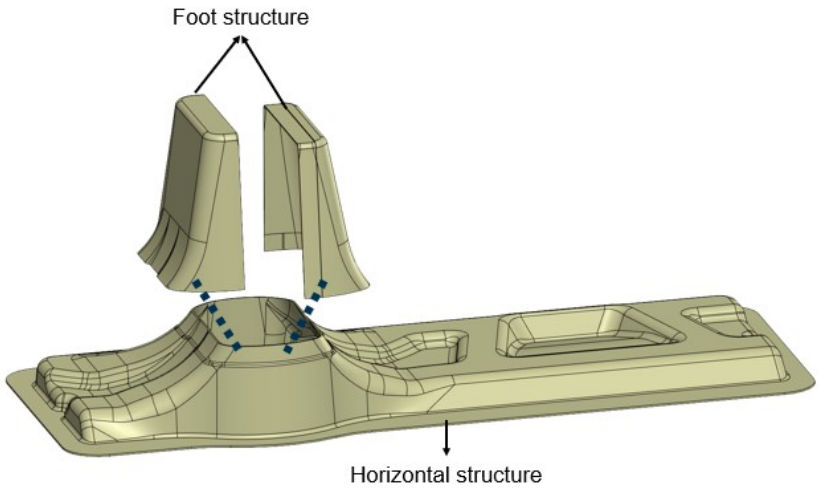

Figure 5-5: The CAD design of the three-piece strategy used for making preforms.

Figure 5-6: Vacuum bagged preform pieces in an oven at 100 ºC for binder stabilization.

Figure 5-7: Stabilized preform of the horizontal structure (Left) and stabilized preform of the foot structure joined horizontally (Right).

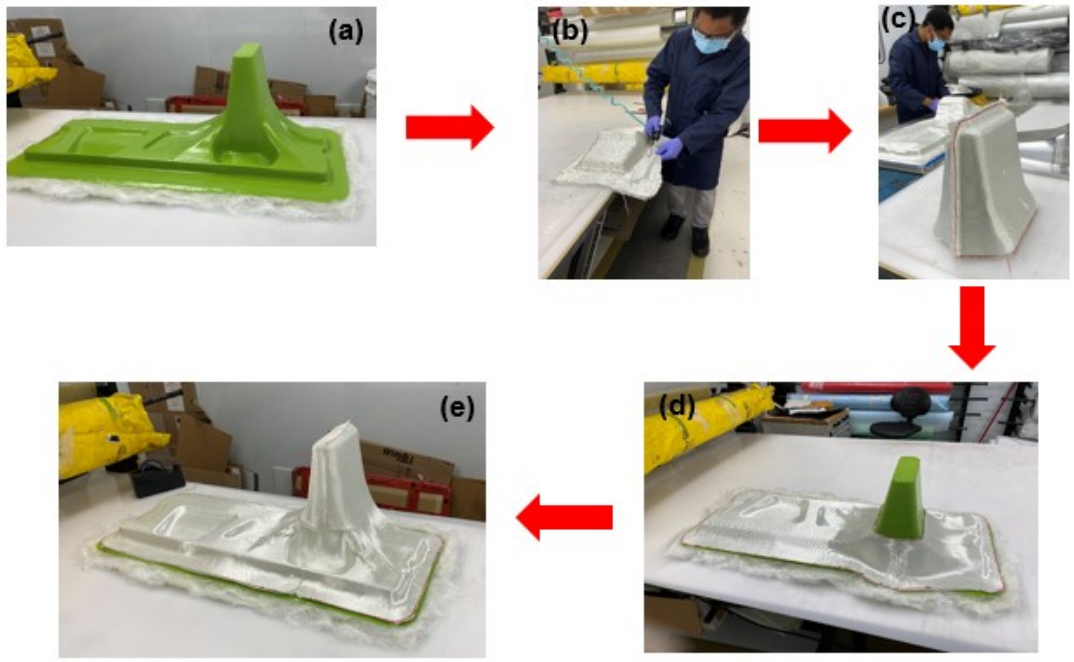

Figure 5-8: (a) 3D printed seat base plug placed on a layup table, (b) the horizontally joined foot structure being cut using an electric fibre cutter, (c) each half of the foot structure being joined together and placed vertically on the layup table, (d) the horizontal preform part draped on the plug, and (e) the remaining preform draped on the foot structure, thus finishing the preforming process.

5.3 Simulation and experimental results

5.3.1 Part 1: Simulation and experiment with one port injection

Injection port 1 (Figure 5-3) was selected as the injection gate. The CRTM process for the complete filling simulation of the part took 12 hours with four cores on an Intel® Core™ i-7 4770 CPU. The results of filling time, evolution of the degree-of-cure, and viscosity at the end of compression are shown in Figure 5-9. The results showed that the total time taken for the entire filling was 280 seconds. The experiment was conducted under the processing conditions defined in Table 5-2, and the total time required to completely infiltrate the part was 205 seconds followed by compression at 0.5 mm/s. The simulation results of the degree-of-cure and viscosity of the resin at the end of the compression phase were important to ensure the closeness of the resin to the gel point. As shown in Figure 5-9, the maximum degree-of-cure was 0.401 at the end of compression sequence (281 seconds), which was well below the gel point of 0.78 for the Gurit standard resin.

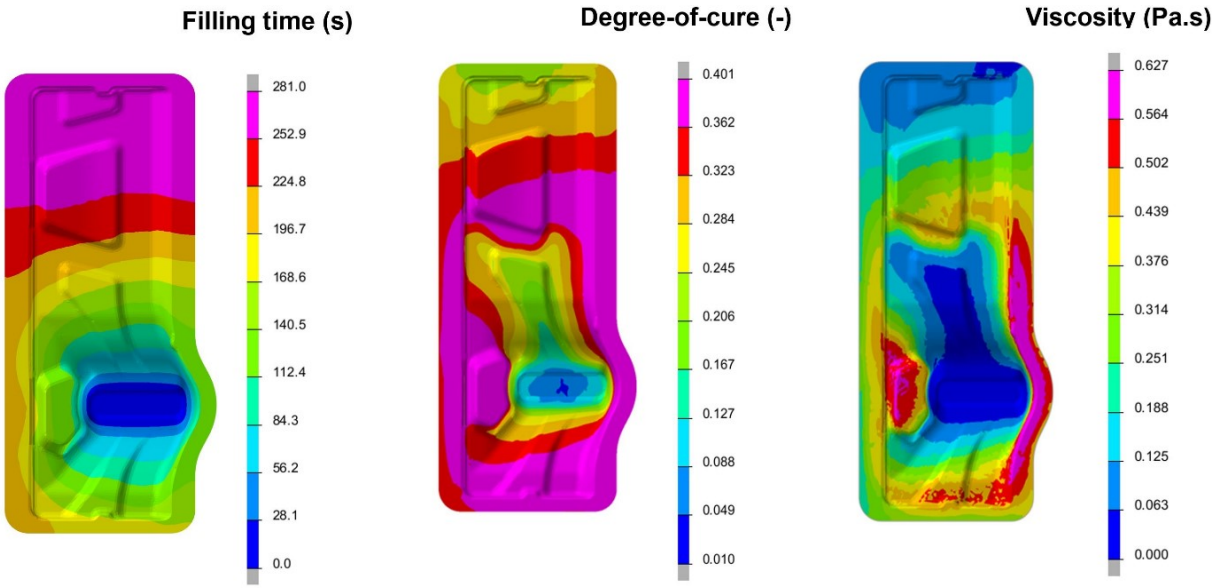

Figure 5-9: Simulation results of showing filling time, degree-of-cure, and viscosity development for a resin injected using port 1 at the end of compression sequence (281 s).

5.3.2 Part 2: Simulation and experiment with two port injection

To reduce the cycle time further, the resin was injected simultaneously using two ports. The simulation results show a total time of 90 seconds. The corresponding experiments showed a filling time of 71 seconds, showing close agreement. Figure 5-10 shows the different stages of the evolution of the flow front along with an image of the manufactured part. A major concern was the possible formation of voids in a fast curing resin system when the two flow fronts meet. The manufactured part appeared transparent to the naked eye indicating, good impregnation.

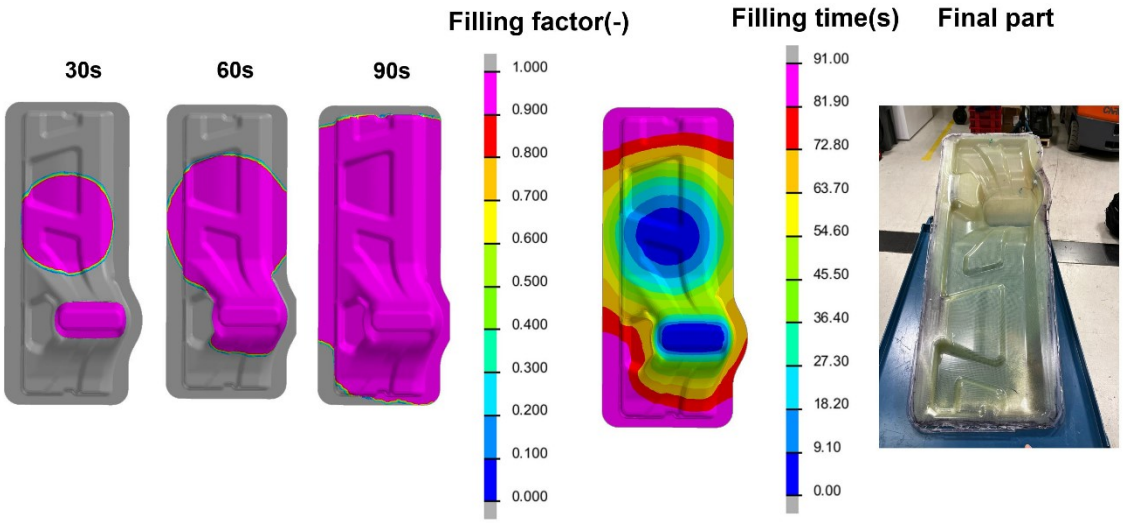

Figure 5-10: Simulation results showing the progression of resin for injection using two ports and the final part produced.

5.3.3 Part 3: Interrupted filling test: Simulation and experiment with one port injection

Unlike the flat plate in the previous chapter, the fabricated mould for the seat base did not include the sensors as it was difficult to machine considering the complexity of the mould. Therefore, the simulation results were validated using only an interrupted filling test. The resin was injected for 60 seconds, and the compression sequence was initiated. With similar processing conditions, simulation was performed, and the results are shown in Figure 5-11. The results showed that the final flow front after the compression stage extended past the injection port 2, whereas the simulation results showed a slight lag in the horizontal structure. The primary reason for this discrepancy was due to the way the preform was modelled in PAM-RTM. The local variations caused by the complex 3-piece strategy were not accounted for in the modelling. Therefore, the

reason for the formation of the dry spot was due to the overlapping of the preform at the joining region of the horizontal and the foot structure, creating an increase in local volume fraction. The Figure 5-12a shows the reason for the formation of the dry spot. Furthermore, to quantify the difference in flow front, three locations were chosen as shown in Figure 5-12b. The lag in the flow front between the two locations is listed in Table 5-3. At point A, the simulation predicts without any error. However, the predictive accuracy decreases as you move towards points B and C. This error increase was due to the structure being unsymmetric with respect to the location of injection port 1. Moreover, the thickening of the preform shown in Figure 5-12a was followed by a tiny pocket which further caused the lag at point C.

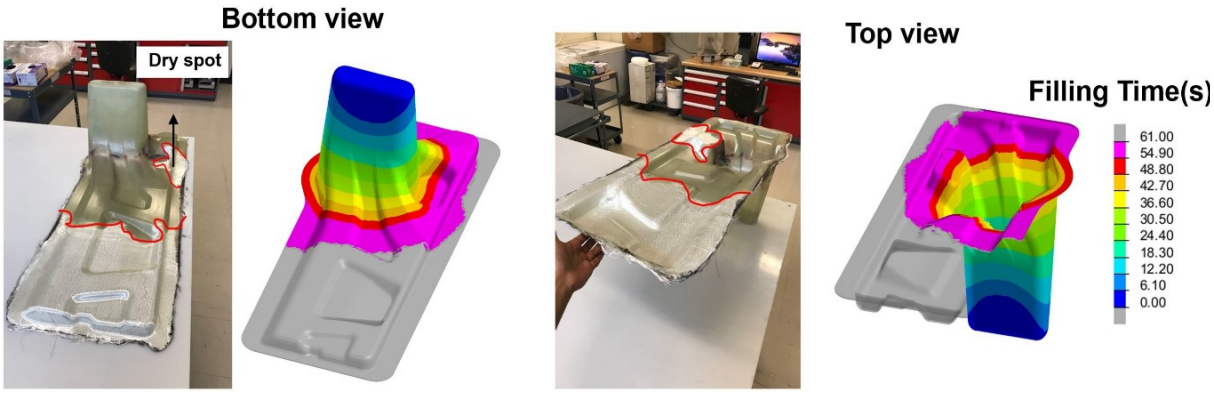

Figure 5-11: Interrupted fill test showing the comparison between experimental and simulation results for an injection time of 60 seconds followed by compression.

Table 5-3: Difference between the horizontal distance of flow front location from injection port 1.

Flow front location	Error (mm)
A	-
B	60
C	175

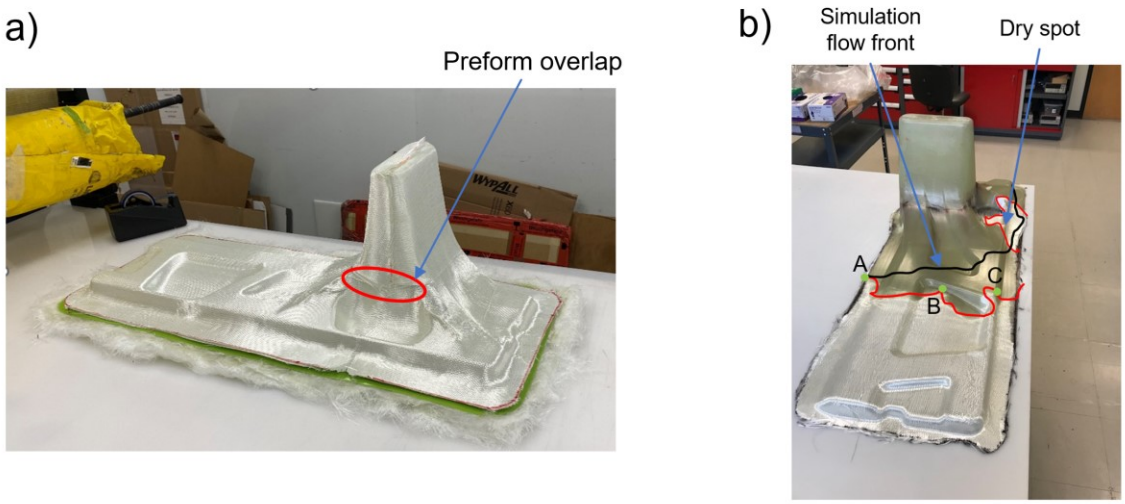

Figure 5-12: (a) Seat base preform showing the overlap at the joining of the horizontal and foot structure, and (b) showing the dry spot and the difference between the simulation and experimental results of the flow front.

5.4 Summary and discussion

In this chapter, a large complex 3D seat base demonstrator part was manufactured using the methodology described in Chapter 4. A composite equivalent of the welded steel assembly was designed and manufactured successfully. A new three-piece preforming strategy was used to make the complex and intricate preform geometry. Finally, the simulation results were validated with experimental results with reasonable agreement considering the length of the part (greater than 1 m). The comparison of the results is tabulated in the Table 5-4.

Table 5-4: Comparison of resin injection time between simulation and experiment

Part	Injection time (simulation) [s]	Injection time (experiment) [s]	% Error
Seat base (1 injection port)	280	205	26.79
Seat base (2 injection port)	90	71	21.22

The following important conclusions were drawn from this chapter:

1) The degree-of-cure and viscosity data from the simulation were extremely important for predicting the proximity of resin to gelation. Ideally, for better flow of the resin, it is extremely important to ensure that the resin viscosity does not to exceed beyond 1 Pas. Theoretically, the resin can flow if the degree-of-cure is below the gel point. However, the viscosity can exceed 1 Pa.s and still be below the gel point. Under these circumstances, it is always good to check the viscosity simulation data and choose process variables that maintain the viscosity below 1 Pa.s at the end of compression. For example, the final viscosity at the end of the compression phase was 0.627 Pa.s, which is well below 1 Pas.
2) Preforming data were not included in the simulation. As a result, the dry spot formation in the interrupted filling test was not captured in the simulation. The results showed the need for a preforming draping simulation to be included because of the complexity of the seat base geometry. While there's room for improvement, a 73% accuracy for fill time in a large industrial part simulation can be considered a good starting point, especially considering the complexity and scale of the part being modelled. At current level, model provides significant value in reducing trial and error approaches and support faster decision making.
3) The use of two injection ports resulted in a significant reduction in the resin injection time of 190 seconds. Choosing more ports would further reduce the injection time; however, this would result in an increase in machining costs. Furthermore, processing modelling significantly reduced the need for trial and error as the simulation results helped choosing ideal processing conditions, thereby significantly reducing cycle time and cost.

CHAPTER 6

6. Process Optimization

This chapter discusses the dimensionless characteristic number used to optimize the process parameters for the CRTM process. The details of the generation of process maps or mouldability diagrams created based on the dimensionless characteristic number are explained for a fully coupled non-isothermal process. The generated map aims to identify the operational window for a given material and tool geometry.

6.1 Dimensionless characteristic number: Injectability number

When dealing with complex materials like fast curing resins and complex manufacturing processes like the CRTM process, the engineers must deal with many process variables to create optimal manufacturing solutions. To ease the burden of the manufacturing engineers, Di Fratta et al. [125], [126] introduced a new dimensionless characteristic number called the Injectability Number (In). This number connects the main process parameters involved in the CRTM process, as illustrated in Figure 6-1. It is characterized by the integral over time of the injection pressure divided by the resin viscosity:

$$In = \int_0^{t_{inj}} \frac{P_{inj}(t)}{\eta(\alpha(t), T(t))} dt \qquad \text{Eq. 6-1}$$

where P_{inj} is the relative injection pressure, η is the viscosity as a function of cure (α) and temperature (T), and t_{inj} is the filling time. Di Fratta et al. proved the invariance of this number with respect to the process parameters, meaning that for a given part geometry, mould configuration and material property, the Injectability Number remains constant.

6.2 Optimization technique

The Injectability Number relates the important process parameters like injection pressure and temperature to the fill time. With the help of this number, a simple optimization tool could be developed which can give you a set of optimized times for a given injection and mould condition.

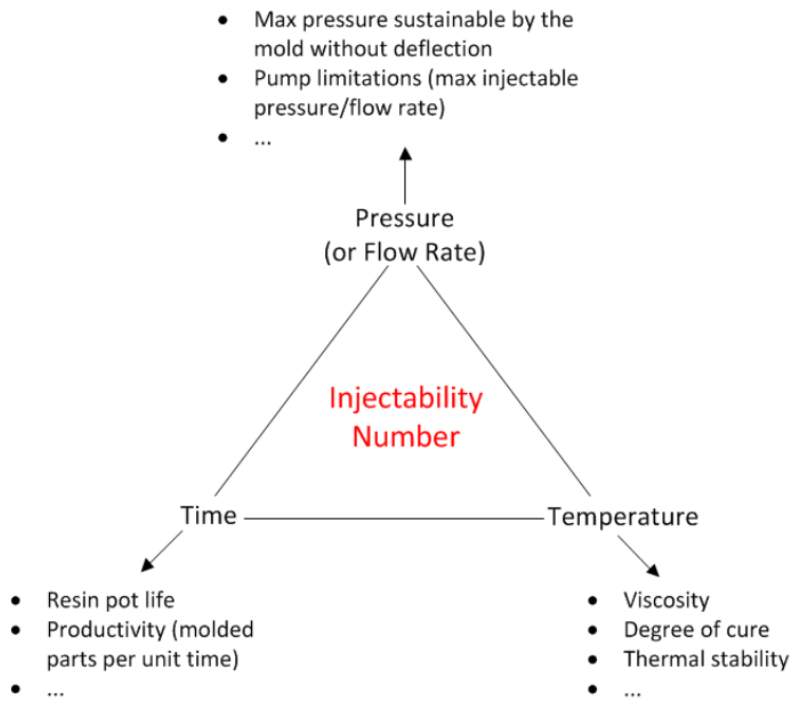

Figure 6-1: Overall process parameters linked to the Injectability number (*In*) [126].

For a given part geometry and mould configuration for a given material, the Injectability Number can be calculated by modifying the Eq. 6-1, assuming a constant injection and constant viscosity. Using the invariance property of the Injectability Number, the injection time can be calculated for different set of constant injection pressure and temperature (viscosity) using the equation:

$$In = \frac{P_{inj} t_{inj}}{\eta(T)} \quad \Rightarrow \quad t_{inj} = \frac{\eta(T)}{P_{inj}} In \qquad \text{Eq. 6-2}$$

With the help of Eq. 6-2, a parameter diagram can be created showing curves that represent a particular injection time for a resin at a sets of constant injection pressure and viscosity, as shown in Figure 6-2a. A mouldability map can be developed by choosing minimum and maximum limits of temperature for pressure and plotting the isochrones, as shown in Figure 6-2b [126].

When dealing with a non-isothermal process like the CRTM process with fast curing resins, the temperature varies with time when cold resin is injected inside a heated mould. In such situations,

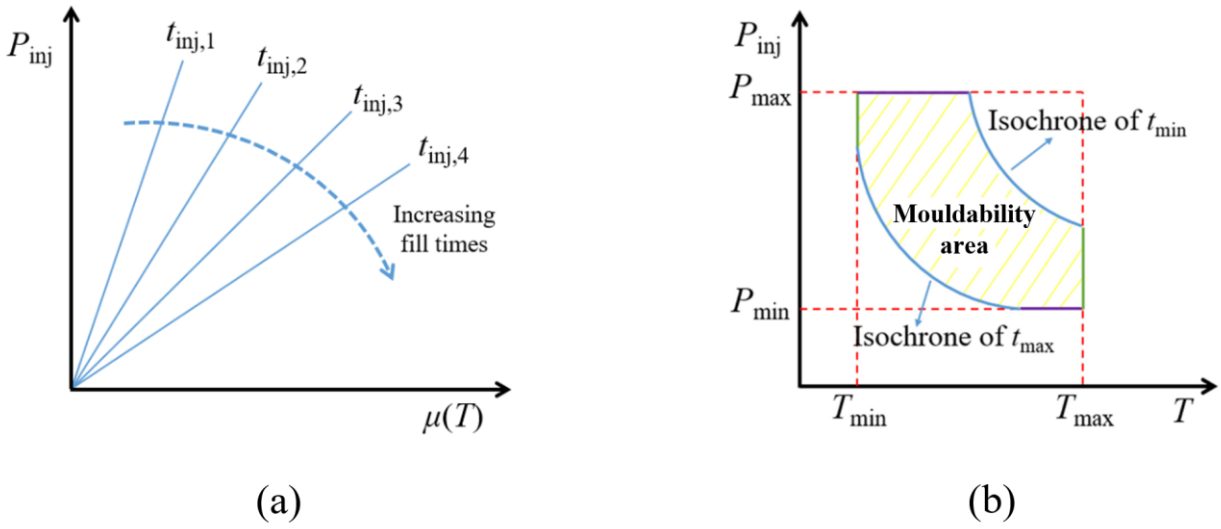

Figure 6-2: a) Parameter diagram showing the filling time isochrones for a particular geometry of the part. (b) Potential mouldability map that can be generated with the help of the injectability number showing the important process variables and the ideal region of mouldability [126].

building mouldability maps can be challenging due to the definition of the Injectability Number (Eq. 6-1) which should be used as a scaling function. Therefore, by calculating the Injectability Number for one simulation for a given injection pressure and constant viscosity, an equation-based optimization technique can be used to generate a mouldability map:

$$In - \int_0^{t_{inj}} \frac{P_{inj}(t)}{\eta(,T(t))} dt \quad \Rightarrow \quad t_{inj} = \underset{\tau>0}{\operatorname{argmin}} \left(\left| In - \int_0^{t_{inj}} \frac{P_{inj}(t)}{\eta(\alpha(t),T(t))} dt \right| \right) \qquad \text{Eq. 6-3}$$

Equation 6-3 implies that t_{inj} is chosen such that the absolute value of the integral is minimized for $\tau > 0$. Here τ serves as a candidate value for t_{inj}. So far, the work by Di Fratta et al. [121] assumed the viscosity of the material changed at the same times throughout the material. However, a cure gradient exists between the resin that entered first into the mould and the last drop of the resin entering the mould especially for fast curing resins. This significantly changes the viscosity and therefore must be factored in while calculating the Injectability Number. Therefore, in the upcoming sections, a methodology to extend the scope of the Injectability Number to develop mouldability or process maps by including the cure gradients (temperature gradients) is introduced.

6.3 Optimization methodology

The steps used for the optimization of the CRTM process using the Injectability Number are listed below for a given mould geometry and part configurations:

1) Perform a non-isothermal simulation at a given mould temperature and an initial temperature of the resin to completely fill the preform.
2) Extract nodal temperature data along the direction of flow of the resin.
3) From the extracted data, develop an equation to capture the evolution of temperature with respect to the time.
4) Calculate the degree-of-cure as a function of temperature and time and viscosity as a function of degree-of-cure and temperature.
5) Calculate the Injectability Number using Eq. 6-1.
6) Develop a simple optimization code (Python, MATLAB etc.) to solve the Eq. 6-3 to find all the values of τ.

To draw a complete mouldability or process map, minimum and maximum values of pressure and temperature are chosen based on the injection equipment and the thermal system of the mould respectively. From the obtained values of τ, a minimum and maximum injection time are chosen to give a realistic range for the CRTM process. Figure 6-3 shows a flow chart detailing the methodology used to develop the map.

6.4 Case study: CRTM flat plate geometry

6.4.1 Simulation setup and result

The same geometry used in Chapter 4 for the flat plate was used to perform the non-isothermal simulation. The initial and boundary conditions are listed as shown in Table 6-1. Additionally, virtual sensors were added to the simulation to get the nodal temperatures along the direction of flow as shown in Figure 6-4. Gurit Standard resin system material models were implemented for this simulation whose model parameters are listed in Table 4-2 of Chapter 4. The temperature simulation results are shown in Figure 6-5. The results show the gradient up until the location of sensor 6 beyond which the resin and the preform attain equilibrium temperature, which is highlighted in Figure 6-5.

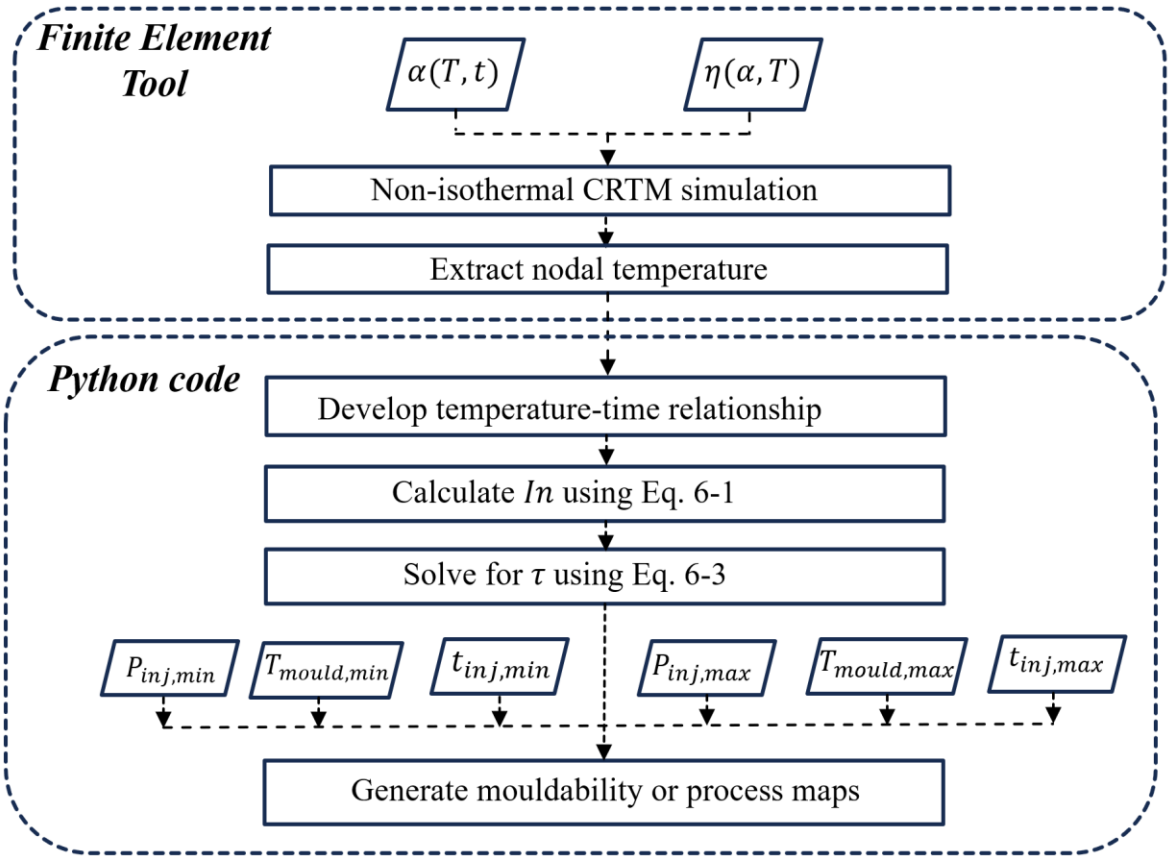

Figure 6-3: Flow chart showing the methodology used to generate the mouldability or process map using the injectability number.

Table 6-1: Important initial and boundary conditions used for the simulation.

Process Parameters	
$V_{f01} = 0.42$	Initial preform volume fraction
$U = 0.5\ mm/s$	Mould closing speed
$T_{pref} = 90\ °C$	Initial preform temperature
$T_{inj} = 25\ °C$	Resin injection temperature
$T_{umould}, T_{lmould} = 90, 90\ °C$	Upper and lower mould temperatures
$T_{amb} = 22\ °C$	Ambient room temperature
$P_{inj}, P_{vent} = 55181E+05\ Pa\ , 0Pa$	Resin injection and vent pressure

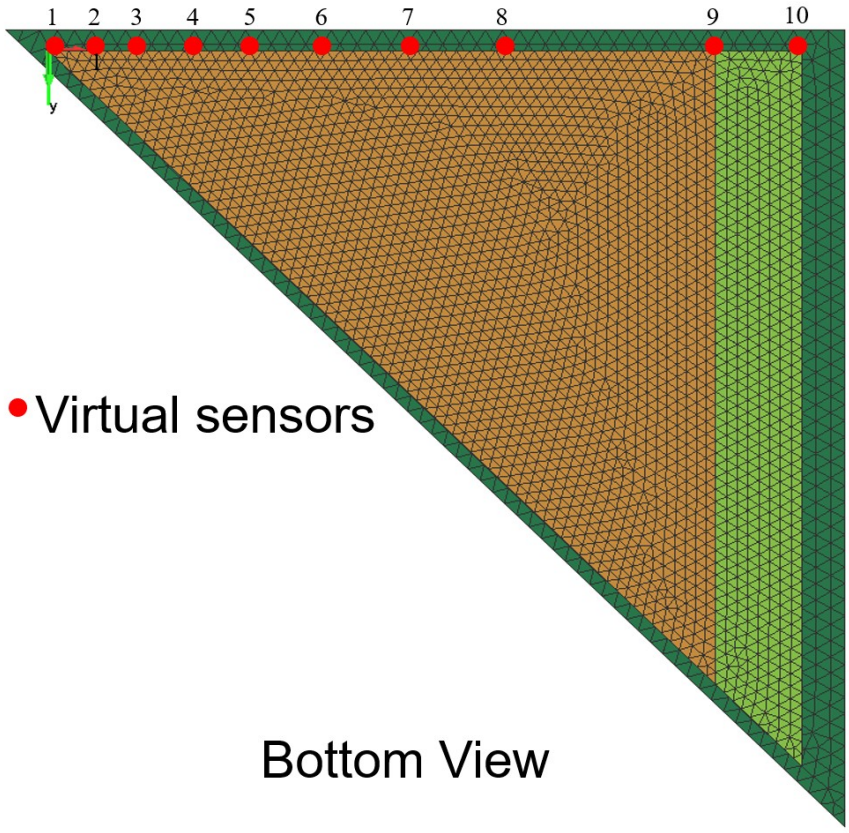

Figure 6-4: Location of virtual sensors to extract nodal temperatures on 1/8th section of the flat plate geometry used for simulation.

6.4.2 Development of temperature-time relationship

The temperature data from the sensors (nodal temperature) were extracted until sensor 6 as the temperature remained constant beyond this sensor. The results are plotted, as shown in Figure 6-6. The results show the evolution of the nodal temperatures as the resin is injected at 25 ºC (room temperature assumption). To develop an approximate rate at which the temperature increases inside the mould, an average temperature of each sensor reading starting from the point at flow front reached the sensor until the lowest recorded temperature was calculated. This was plotted against the average time the sensor took to reach the lowest reading from the arrival of the resin flow front and the resulting curve is shown in Figure 6-6. Now to develop a mathematical

relationship between the temperature and time, the following exponential relationship is proposed to fit the curve (rise in temperature inside the mould) shown in Figure 6-6:

$$T(t) = \frac{T_{mould}}{(1 + \exp(-a(t - b))} \quad \text{Eq. 6-4}$$

$$a = A' \exp(B' * T_{initialresin}) \quad \text{Eq. 6-5}$$

$$b = A'' \exp(B'' * T_{initialresin}) \quad \text{Eq. 6-6}$$

here T_{mould} and $T_{initialresin}$ are mould and initial resin temperatures in Celsius respectively and t is the time in seconds. The fitting parameters a and b are the function of initial resin temperature. The terms A', B', A'' and B'' are fitting constants whose values are listed in Table 6-2. The evolution of temperature with respect to time based on the defined Eq. 6-4 is as shown in Figure 6-7.

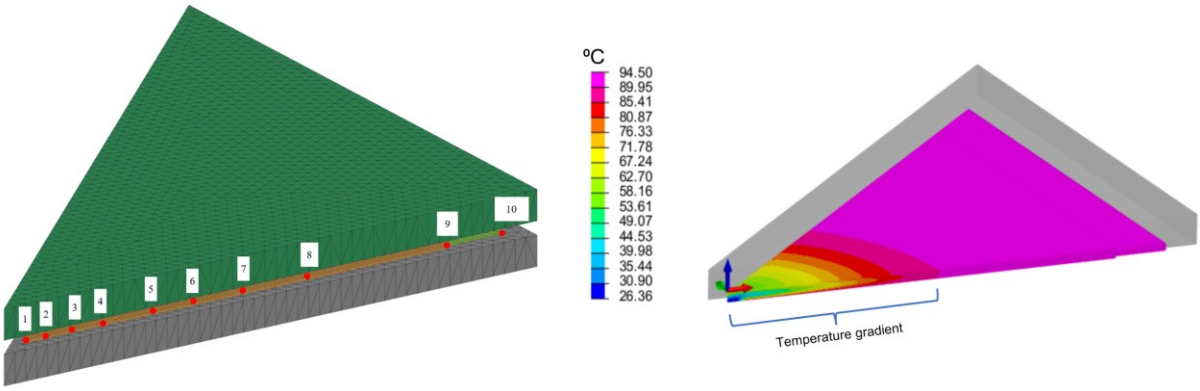

Figure 6-5: Simulation setup with the location of sensors in isometric view (left), and the temperature simulation results for complete fill highlighting the temperature gradient caused due the colder resin entering the preheated mould and preform (right).

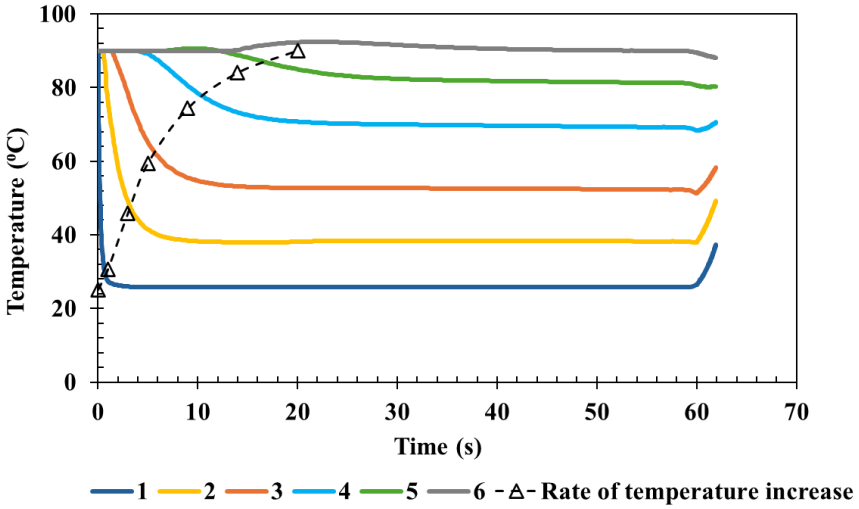

Figure 6-6: Plot showing the evolution of temperature at the virtual sensor locations from 1 to 6 with respect to time for a non isothermal CRTM simulation.

Table 6-2: The fitting constants for the model used for capturing the evolution of temperature with respect to time during resin injection.

Model parameters	Value
A'	0.2641
A''	13.59744
B'	$0.005 * T_{mould} - 0.025$
B''	−0.07207

6.4.3 Calculation of Injectability Number (In)

After calculating $T(t)$ in the previous section, the degree-of-cure was calculated using the temperature-time fit as the cure cycle. With this data, the term $\eta(\alpha(t), T(t))$ was calculated. This data was plotted along with temperature with respect to time, as shown in Figure 6-8. Using Eq. 6-1, the In was calculated for constant pressure injection (P_{inj}) and the calculated η based on the temperature-time model fit. Therefore, an In for a non-isothermal CRTM process was obtained. The calculated value of In was 4.3089x10^8.

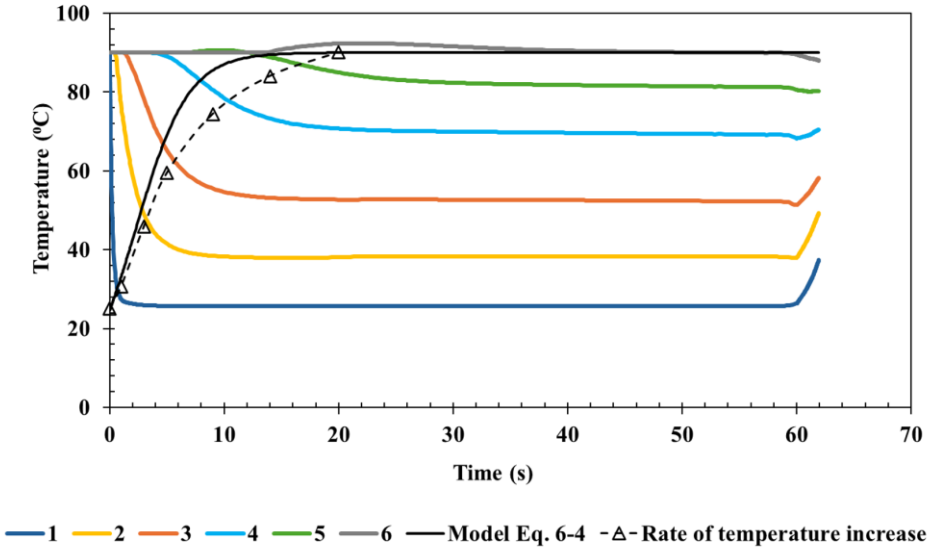

Figure 6-7: The temperature data (nodal) from the sensors 1-6 and a temperature-time fit developed to account for the temperature (cure) gradient by fitting the average rise in temperature curve during the infiltration of resin into the CRTM mould.

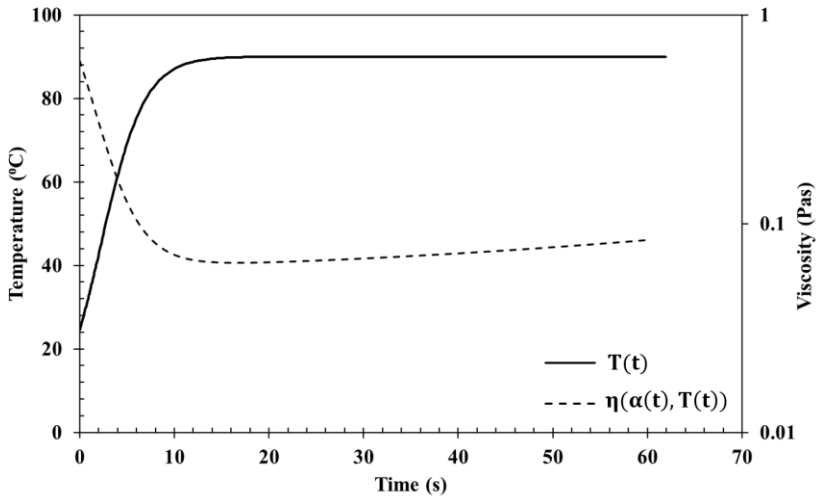

Figure 6-8: Evolution of viscosity for the corresponding temperature development inside the mould during resin infiltration into the CRTM mould.

6.4.4 Optimization and generation of mouldability map

Once the Injectability Number was calculated, a simple continuous constrained optimization code was written on python to solve Eq. 6-3. Once the minimum and maximum limit for pressure and temperature was defined for the flat plate geometry, all the possible values of τ were generated. At this point, a minimum and maximum t_{inj} was defined to obtain the mouldability map. The mouldability map generated for the flat plate geometry for non-isothermal injection of the Gurit standard epoxy resin as shown in Figure 6-9. The minimum and maximum limit values are given in Table 6-3.

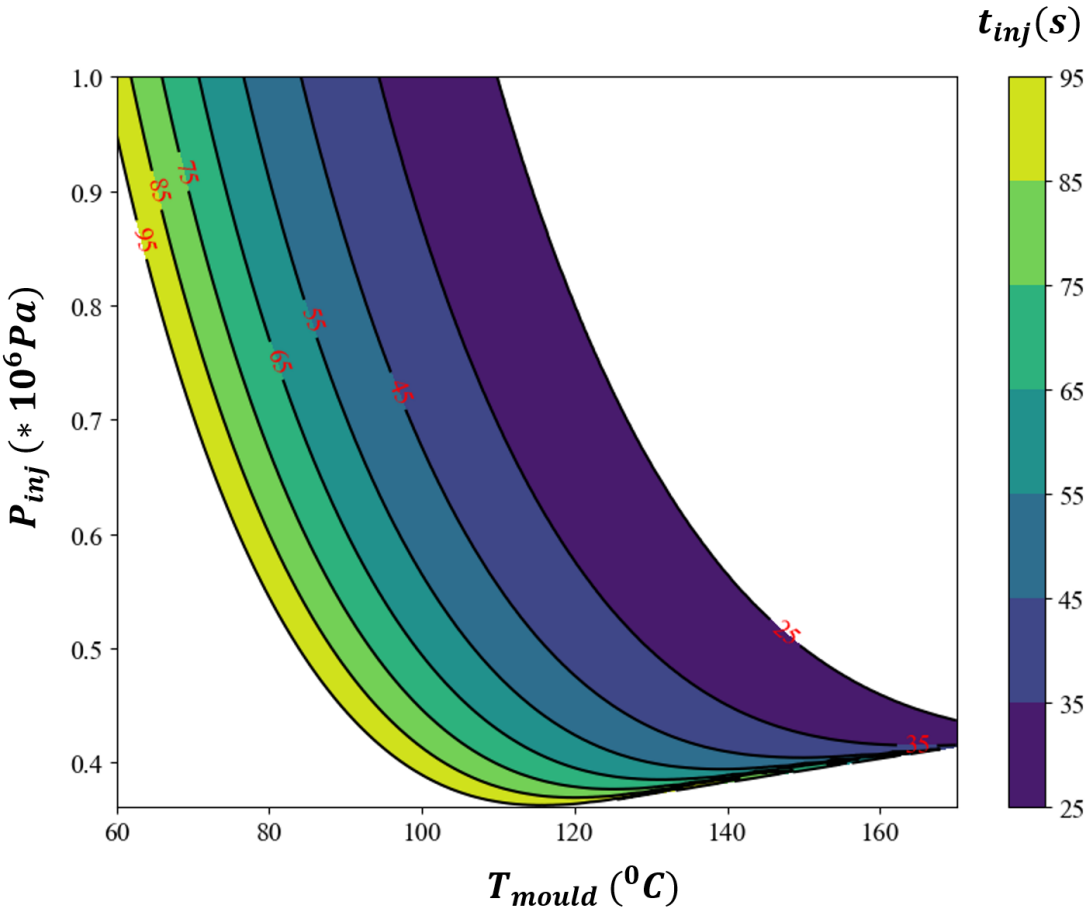

Figure 6-9: Mouldability map for Gurit standard resin in terms of injection pressure and temperature of the mould at an injection temperature of 25 ºC.

Table 6-3: Minimum and maximum values used in mouldability map.

Limit	Value
P_{injmin}	$0.01E+06\ Pa$
P_{injmax}	$1E+06\ Pa$
$T_{mouldmin}$	$60\ ^0C$
$T_{mouldmax}$	$170\ ^0C$
t_{injmin}	25 s
t_{injmax}	95 s

6.5 Validation

6.5.1 Verification of temperature-time relationship for multiple mould temperatures

Eq. 6-4 was verified for multiple mould temperatures. The simulations were carried out for mould temperatures of 110 ºC and 130 ºC with resin injected with an initial temperature of 25 ºC. The results of the models for both the cases are shown in Figure 6-10. In the figure, you can clearly see at sensor 6, the nodal temperatures for both 110 ºC and 130 ºC mould temperatures do not fall below their mould temperatures, which the model predicts accurately. This proves that the approach used can be reliable to generate the mouldability maps. However, as the mould temperature increases, the readings in sensor 5 and sensor 6 show significant overshoot of temperature above the mould temperature because of exothermic reaction, which is not captured by the model.

6.5.2 Verification of process map for Gurit standard resin

To verify the validity of the process maps, few conditions were chosen inside and outside the mouldability regions to validate the process map generated for the flat plate geometry and the Gurit standard resin system. A mix of available simulation and experimental data was checked to see if the data points lie within the minimum and maximum values defined for the mouldability maps.

A point outside the range denoted by point A as shown in the process map was chosen to check if this condition can be simulated successfully. The mould temperature and injection pressure were chosen as 160 ºC and 2 x 10^5 Pa respectively as shown in Figure 6-11a. A simulation was run on PAM-RTM to see if the resin can be completely injected under these processing conditions. As

seen in the Figure 6-11b, the resin reaches gel point before complete injection. Just with the help of the mouldability map it was possible to show that the chosen processing parameters would not result in complete impregnation. To further investigate the process map, a point B was chosen inside the map as highlighted in Figure 6-11a. The simulation result showed complete injection with final degree-of-cure well below the gel point of Gurit standard resin (0.78) ensuring complete injection at 61.5 s as shown in Figure 6-11c. The predicted point on the map showed an injection time between the contours 55 s and 65 s which is extremely close to the simulation results further validating the process map.

The In found for non-isothermal CRTM process for flat plate geometry was validated with a simulation using constant viscosity. The simulation took a total time of 69.61 seconds to completely infiltrate the preform as shown in Figure 6-12 for a viscosity of 0.1 Pas. The In was calculated for this condition using Eq. 6-2. The In value calculated was 4.5225 x 10^8. The values are compared in Table 6-4 showing a close match.

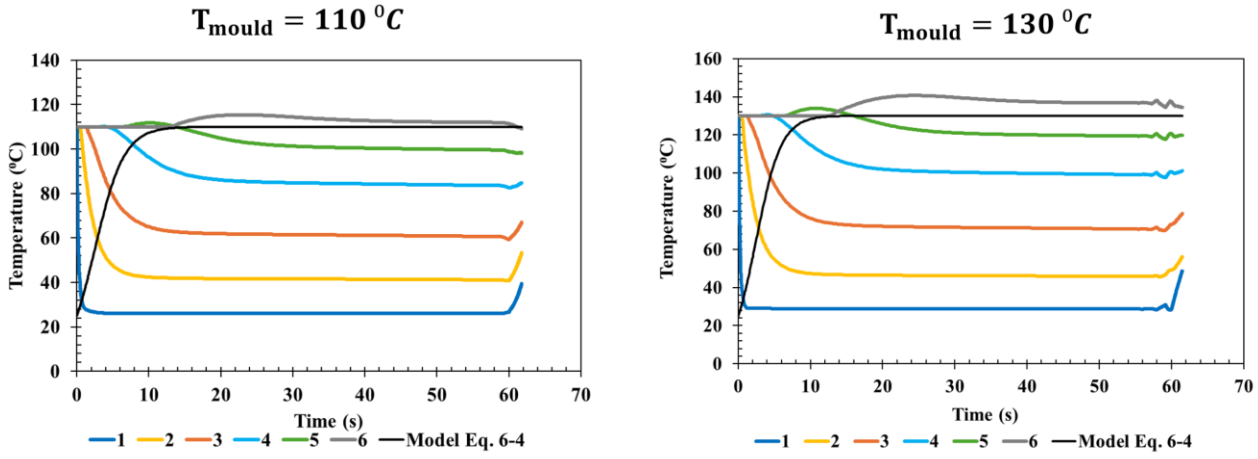

Figure 6-10: Temperature time fit showing the model fit for mould temperatures 110 ºC (left) and 130 ºC (right). The model fit effectively captures the temperature gradient as the sensor 6 temperature data shows equilibrium temperature between resin and fibre.

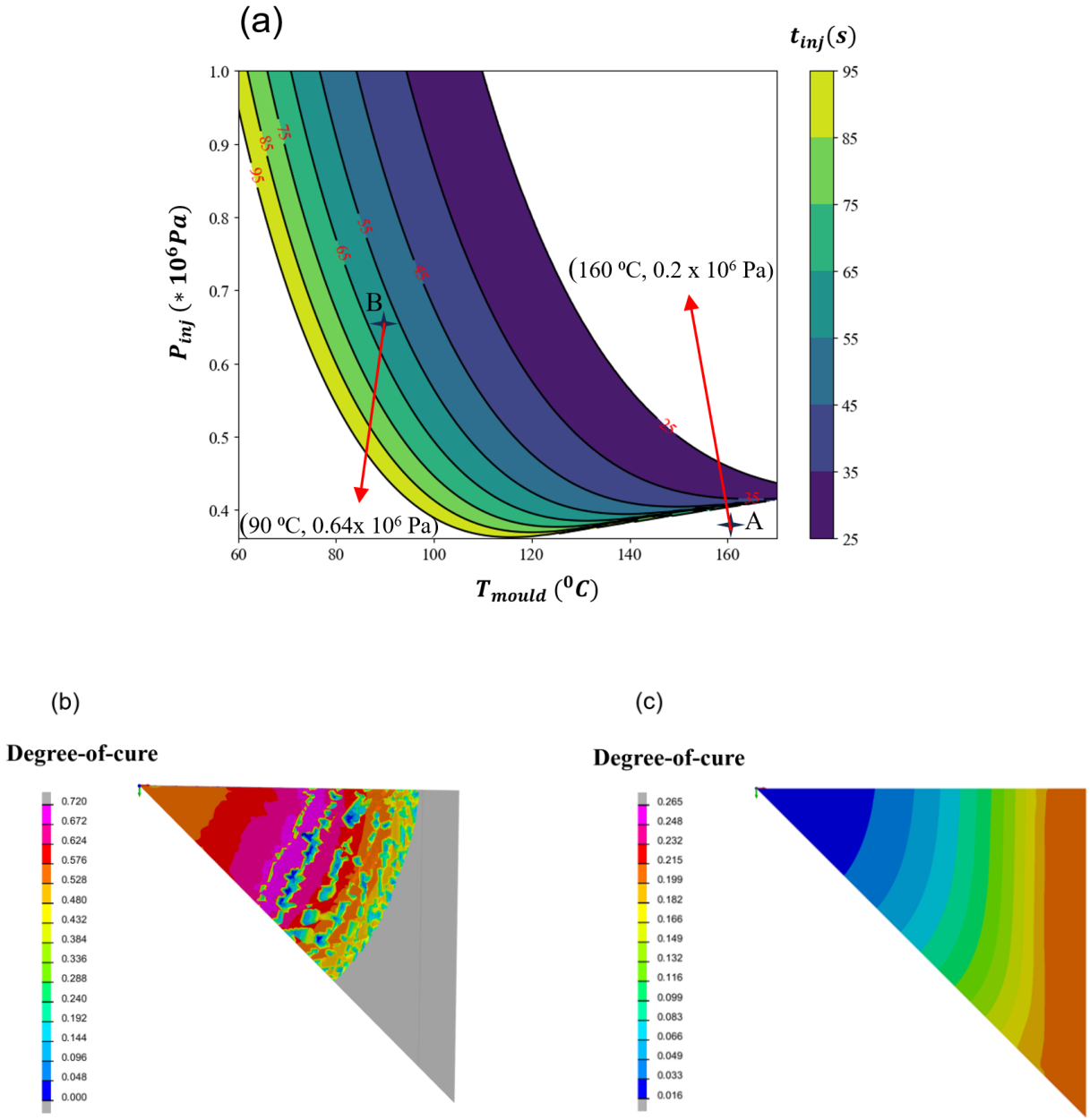

Figure 6-11: a) Mouldability map showing a point outside and inside the mouldability zone respectively. (b) Validation of simulation of the point outside the mouldability zone showing incomplete filling with a degree-of-cure greater than the gel point. (c) Validation of the point inside the mouldability zone showing complete filling with gel point well within the gel point.

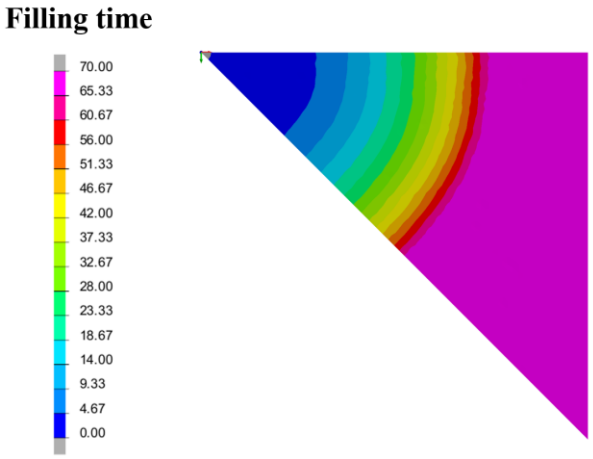

Figure 6-12: Filling time for injection of resin with constant viscosity of 0.1 Pas.

Table 6-4: Comparison of Injectability Number for non-isothermal injection and injection with constant viscosity.

Resin	Injectability Number (In)
Variable viscosity	$4.3089E+08$
Constant viscosity	$4.5115E+08$

6.6 Influence of initial resin temperature

So far, all the results have been obtained by keeping the initial temperature of the resin at 25 ºC. However, fast curing resins are extremely sensitive to the initial resin temperature. Therefore, as seen in Eq. 6-5 and Eq. 6-6, the fitting terms used in Eq. 6-4 are a function of initial temperature of the resin.

The sensitivity of the initial temperature of Gurit resin was validated with the mouldability map. The simulations were caried out at an injection pressure of 0.64 MPa for initial resin injection temperatures of 25 ºC, 30 ºC and 35 ºC and mould temperature of 100 ºC. The filling time simulation results are shown in Figure 6-13 clearly showing a faster filling time for increasing initial resin temperature. To validate the time obtained using the process map, the initial resin temperature, mould temperature and the injection time data were extracted as shown in figure 6-

14. The data points of injection time for mould and initial temperature of the resin are shown in Figure 6-15. The results obtained were listed on Table 6-5 to show the comparison of the injection time obtained using PAM-RTM simulation and the mouldability map.

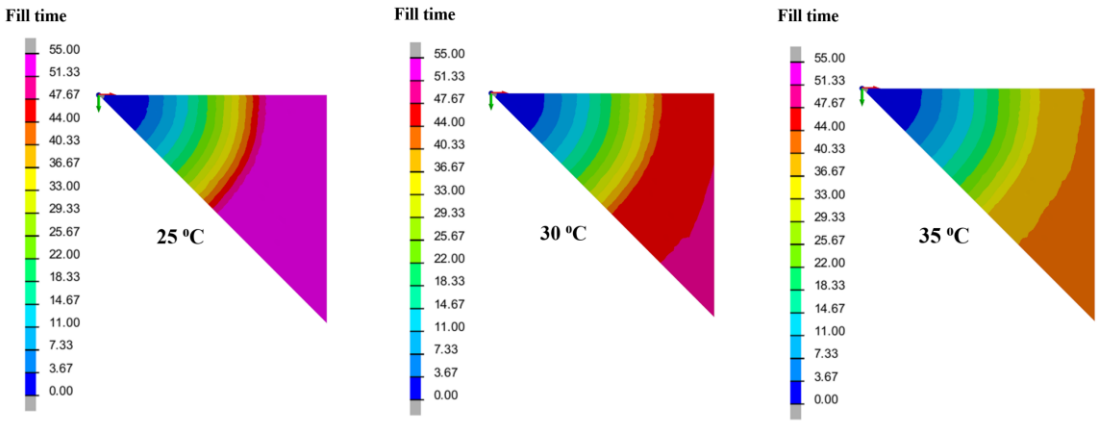

Figure 6-13: Filling time results of simulation of the CRTM flat plate geometry at three different initial resin temperatures of Gurit standard resin.

6.7 Summary and discussion

In this chapter, the Injectability Number (In) introduced by Di Fratta et al. [126] was extensively explored to optimize the important processing parameters of the CRTM process with fast curing resin. The use of Injectability Number to develop mouldability maps for the CRTM process was successfully demonstrated in this chapter.

The following important conclusions can be underlined from this chapter:

1) An optimization technique was developed to utilize the Injectability Number to predict total resin fill times for the CRTM process with flat plate geometry for a set of resin injection pressures and mould temperatures.

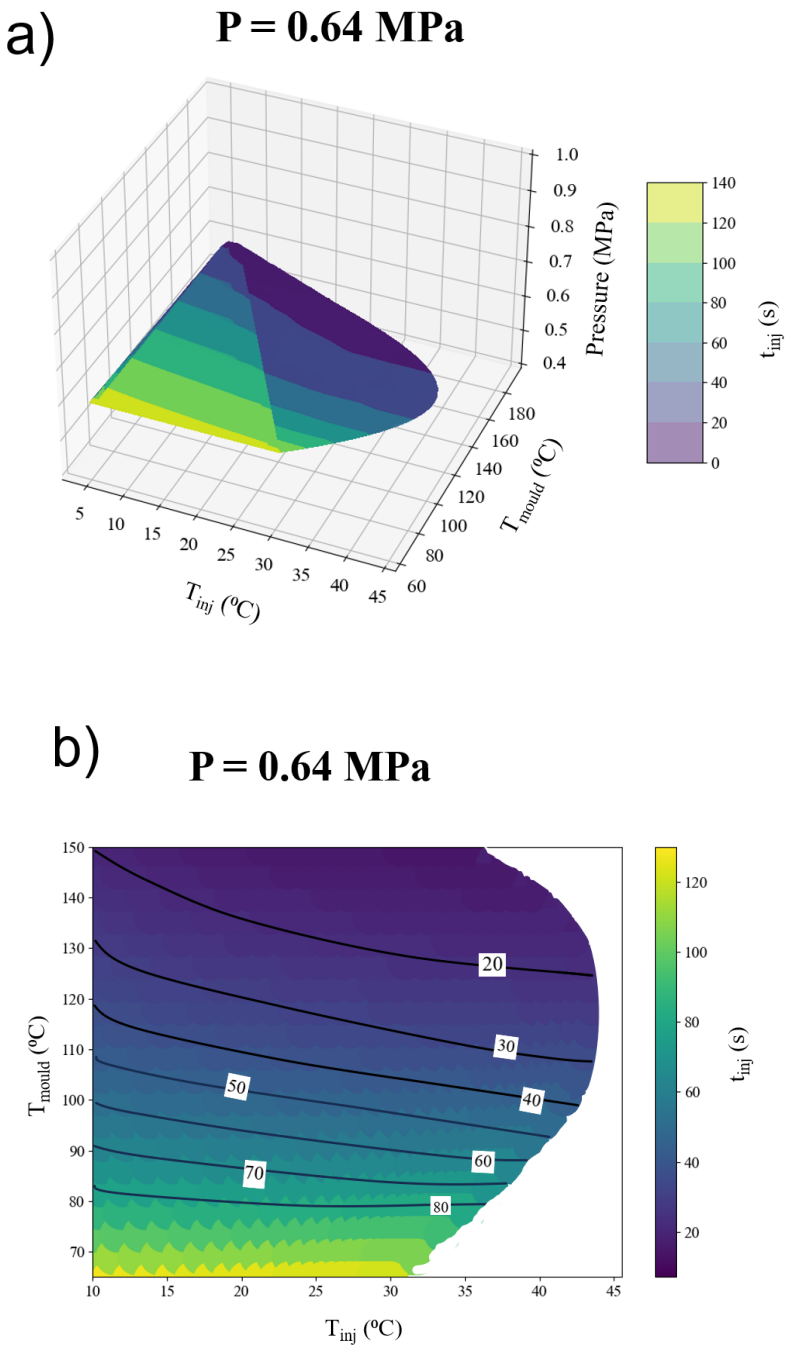

Figure 6-14: a) Plane on a 3D plot showing the injection times for different mould and initial resin temperatures for a pressure of 0.64 MPa. (b)The corresponding 2D projection showing the injection time contours in detail for mould and initial resin temperatures.

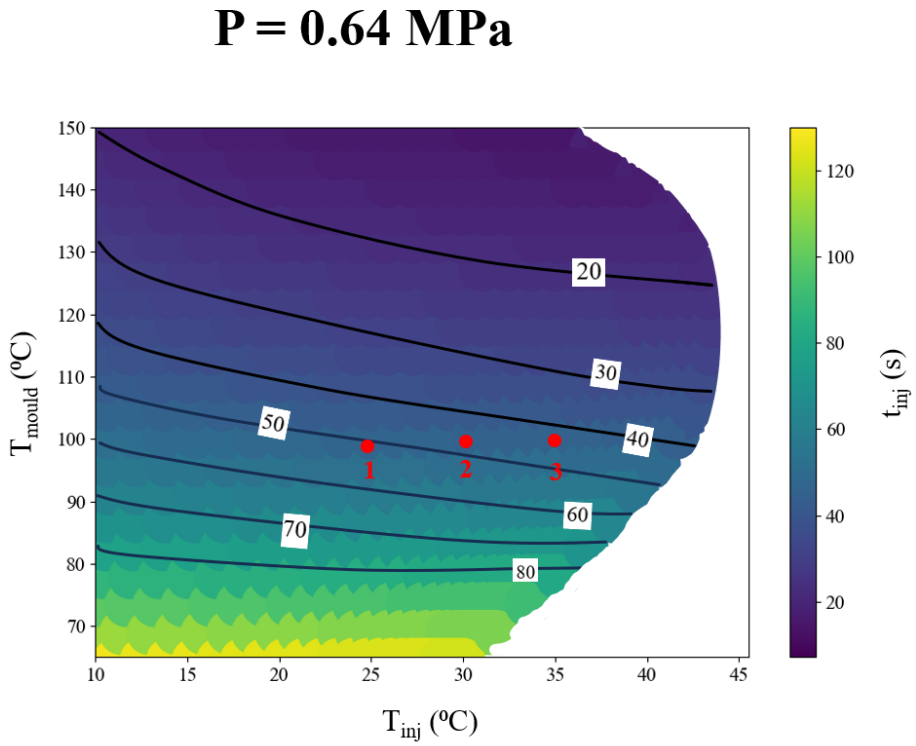

Figure 6-15: The 2D projection of the mouldability map showing the prediction for the effect of initial temperature of resin on the injection time. Points 1, 2 and 3 represent 25 ºC, 30 ºC and 35 ºC respectively.

Table 6-5: Comparison between the simulation results and the prediction by mouldability map of injection time for a set of initial resin injection temperatures.

Point	P_{inj} (MPa)	T_{mould} (ºC)	T_{inj} (ºC)	t_{inj} simulation (s)	t_{inj} mouldability map (s)	% error
1	0.64	100	25	54.90	51	7.14
2	0.64	100	30	50.60	48	5.41
3	0.64	100	35	43.52	42	3.49

2) Effect of initial temperatures of the resin before injection was included in the time-temperature relationship. This way, a 3D mouldability map was defined to include the initial temperature of resin along with the injection pressure and mould temperature, thereby, increasing the predictive capability of the mouldability maps.
3) A detailed case study was conducted on a flat plate geometry. The mouldability map generated was validated with simulation results showing excellent validation of injection times for multiple initial resin temperatures. A close agreement between simulation and mouldability map results were obtained with a maximum error of 7%.

Injectability Number serves as an important tool for industries who strive for the reduction of process cycle time. Though, simulations have helped to reduce the number of experimental trials, multiple physics fully coupled simulations can consume extreme amounts of power which is generally ignored. Here, with the help of dimensionless injectability number, the resin injection time for a known geometry of the mould and fibres can be predicted with just one simulation. These simulations were carried out on an Intel® Core™ i7-4770 CPU with four cores. Each non-isothermal simulation took approximately 30 minutes. Once the nodal temperatures were extracted, the python optimization code takes just approximately 2 minutes to generate mouldability maps, showing significant reduction in time.

The Injectability Number values calculated for constant and variable viscosity including cure gradients are very close in agreement with each other, as shown in Table 6-4. This proves that the Injectability Number remains constant as long as the mould geometry and material properties of the fibres remain consistent. This unique number can therefore be extended to develop mouldability maps for wide variety of resins by just performing a simulation on one resin system. However, it is important to find the temperature-time relationship for each resin system based on the material model used.

CHAPTER 7

7. Conclusions and Future Outlook

This thesis has developed and validated comprehensive process model for Compression Resin Transfer Moulding (CRTM) using fast curing resins successfully. The main objective of this work was to model the Compression Resin Transfer Moulding process for making composite parts using fast curing resins. The first part of the work involved the experimental characterization and material model development of fast curing resins and a non-crimp glass fibre. The second part of the work involved the implementation of these material models in the finite element tool PAM-RTM to simulate the CRTM process for two cases: (i) a simple flat plate, and (ii) a complex seat base for a long-distance coach. Finally, an optimization methodology was developed to find key processing parameters for the CRTM process. The important conclusions that can be drawn from this work are as follows:

1) **Chemo-rheological characterization of fast curing resins showed that it was extremely difficult to perform experiments at higher isothermal temperatures.**

   The recording of the experimental data at higher isothermal temperatures (greater than 110 ºC) was challenging with current equipment (DSC, rheometer). With higher reactivity of the resin the maximum temperature at which isothermal tests were conducted lowered. Furthermore, these resins were characterized by high exotherms (greater than 400 J/g) which can have detrimental effects on the final part due to thermal stresses. Moreover, the material models developed here facilitated better prediction and control of the curing process.

2) **A fully coupled CRTM simulation was performed and validated experimentally.**

   A coupled heat transfer, resin flow, compaction and resin cure models were simulated using PAM-RTM. The latest fluid-solid coupled solver of PAM-RTM was leveraged to build the model and the resin models developed were implemented with the help of user defined subroutines in the form of C-script. The sensors installed at strategic locations helped to validate the simulated resin pressure and temperature evolution inside the mould. Furthermore,

the used of sensors gave the opportunity of live data monitoring of the temperature and pressure evolution inside the mould.

Original contribution: Unlike previous work found in literature where simulations only included resin injection and compression part of the CRTM process, this work demonstrated the effectiveness of the simulation approach to replicate the entire manufacturing cycle from the placement of preform till demoulding. Furthermore, the simulations included the mould geometry and accounted for the heat transfer between the mould, preform and the injected fast curing resin.

3) **A large complex ground transportation demonstrator part was manufactured using the CRTM process.**

The simulation approach used in this work helped eliminate the process of trial and error and a composite seat base of a long-distance coach was manufactured using the CRTM process with excellent part quality. Furthermore, this project demonstrated the viability of the CRTM process to manufacture complex and intricate ground transportation components using fast curing resins.

Original contribution: This work demonstrated a step-by-step procedure for manufacturing a large component with a complex and intricate design using fast-curing resin and glass fibre. Currently, there is little to no knowledge of using fast curing resin to manufacture a complex part in an industrial setting using the CRTM process for ground transportation applications.

4) **An optimization technique was developed using a dimensionless characteristic number.**

Injectability Number (In) was used to generate mouldability map for a non-isothermal CRTM process. A close agreement (<7% error) was found between the injection time predicted by mouldability map and PAM-RTM simulations.

Original contribution: Due to the sensitivity of the fast curing resin to the initial temperature, a time-temperature relationship was defined which included the initial temperature of the resin as a parameter. This way the Injectability Number was calculated by including the cure

gradient. Furthermore, the optimization technique used to generate the mouldability maps significantly reduced the computational costs.

In conclusion, the injectability number has high potential to significantly impact the manufacturing of composite materials using LCM methods. For automotive and ground transportation industry where cycle time is highly important, having a tool to predict injection times based of a number can be incredibly beneficial. However, it is important to remember that the predictive accuracy of the injectability number solely depends on the accuracy of the material models.

7.1 Future outlook

7.1.1 Resin characterization

In terms of characterization of fast curing resins, there is still a significant room for advancement. Cure kinetics and viscosity characterization of fast curing resins at higher temperatures is extremely difficult as the current measuring techniques cause significant loss in data, as no values are captured at the onset of the reaction due to the time required for mixing and sample application into the measuring equipment [63]. Process automation can be a solution where a robotic arm or mechanical mixing system can be used to mix the resin and hardener to dispense known quantity of resin sample at rapid rates. This can save a significant amount of time and thereby reducing the data loss in the measurement of both cure kinetics and viscosity. Furthermore, machine learning models have the potential to increase the predictive accuracy of the cure kinetics and viscosity.

To select the most suitable resin material model, it is optimal to test each model, starting with the simplest and progressing to more complex ones, while evaluating their performance against the actual thermal history of the resin in the process being modelled. For instance, in this study, the CRTM mould was preheated, and the resin was injected at room temperature. The thermal history of the resin in this process follows a temperature ramp, starting from room temperature until reaching the moulding temperature. Therefore, the resin material models for this process should be validated under a temperature ramp scenario. Similarly, for processes like autoclave curing, the models should be evaluated against a cure cycle, which typically includes a combination of temperature ramps and holds.

7.1.2 Fibre characterization

Wet compaction data has been typically used to model the CRTM process. However, there exists both wet and dry regions in the preform during the injection and compression stages of the CRTM process. Few 1D simulation studies have shown the presence of hydrodynamic compaction effects and the transition of fibre compaction properties from wet to dry regions [107-109]. Incorporating these effects to complex 3D geometries could provide more accurate predictions of fibre bed deformation and resin flow during the CRTM process, thereby improving the overall process simulation.

Most preforming process for complex geometry involves the application binders to hold the fibres together in shape. These binders can potentially have significant effect on the viscosity of the fast curing resin which can be a potential area that needs to be explored. More research in process automation in preforming processes needs to be studied to increase productivity and reduce manual labour and thereby reducing the overall cycle time. Furthermore, reduction of waste caused by preforming process need to be explored by looking at potential ways to recycle the fibre offcuts.

7.1.3 Simulation

With industry 4.0 well underway, manufacturing technologies are poised for the integrations of digital twin technology. The use of digital twins in composite manufacturing using the CRTM process can have a huge potential in reducing the process cycle times and cost [145-146]. The digital twin technology has the potential to improve mould designs, control resin flow and predict defects which can be incredibly beneficial for the CRTM process.

Combining Artificial Intelligence (AI) with currently existing process models can further enhance manufacturing precision [147]. Industries can optimize processes with less physical trial and error, by training AI models on the data generated from simulations, leading to quicker development cycles and improved part quality. However, handling of substantial number of process parameters and material variabilities will require advancements in data reduction techniques and robust design of experiments.

REFERENCES

[1] L. Barcenas, S. S. Narayana, L. Khoun, P. Trudeau, and P. Hubert, "Thermochemical and rheological characterization of highly reactive thermoset resins for liquid moulding," *J. Compos. Mater.*, vol. 57, no. 19, pp. 3013–3024, Aug. 2023, doi: 10.1177/00219983231181640.

[2] S. Sarojini Narayana, L. Barcenas, L. Khoun, and P. Hubert, "Simulation and validation of 3D compression resin transfer moulding," presented at the Canadian International Conference on Composite Materials, Fredericton-Moncton, NB, CA, 2922.

[3] S. Sarojini Narayana, L. Barcenas, L. Khoun, N. Milliken, P. Trudeau, and P. Hubert, "Process development of compression resin transfer moulding of a complex demonstrator part," presented at the Flow Processes in Composite Materials, West Lafayette, IN, USA, 2023.

[4] Drew, Kojak and Mezler, Dan, "Prospects for fuel efficiency, electrification and fleet decarbonization." International Council On Clean Transportation, May 2019.

[5] L. Khoun and P. Trudeau, "SNAP RTM: A cost-effective compression-RTM variant to manufacture composite component for transportation applications," presented at the Automotive Composites Conference and Exhibition, Novi, Michigan, USA: Society of Plastics Engineers, 2018.

[6] L. W. Cheah, "Cars on a Diet: The Material and Energy Impacts of Passenger Vehicle Weight Reduction in the U.S.," PhD Thesis, Massachusetts Institute of Technology, Cambridge, Massachusetts, USA, 2010.

[7] *Cost, Effectiveness, and Deployment of Fuel Economy Technologies for Light-Duty Vehicles*. Washington, D.C.: National Academies Press, 2015, p. 21744. doi: 10.17226/21744.

[8] S. Muzumdar, "Opportunity and Challenges in Automotive Composites Industry," Dec. 12, 2013.

[9] A. P. R. Sherratt, "Computational Modelling of Resin Infiltration and Curing in High Pressure Resin Transfer Molding," PhD Thesis, The University of Western Ontario, London, Ontario, Canada, 2022.

[10] J.-A. E. Manson, M. D. Wakeman, and N. Bernet, "2.16 - Composite Processing and Manufacturing—An Overview," in *Comprehensive Composite Materials*, A. Kelly and C. Zweben, Eds., Oxford: Pergamon, 2000, pp. 577–607. doi: https://doi.org/10.1016/B0-08-042993-9/00167-4.

[11] D. S. Cairns, D. R. Humbert, and J. F. Mandell, "Modeling of resin transfer molding of composite materials with oriented unidirectional plies," *Compos. Part Appl. Sci. Manuf.*, vol. 30, no. 3, pp. 375–383, Mar. 1999, doi: 10.1016/S1359-835X(98)00081-5.

[12] P. Simacek, S. G. Advani, and S. A. Iobst, "Modeling Flow in Compression Resin Transfer Molding for Manufacturing of Complex Lightweight High-Performance

Automotive Parts," *J. Compos. Mater.*, vol. 42, no. 23, pp. 2523–2545, Dec. 2008, doi: 10.1177/0021998308096320.

[13] M. Baskaran, I. O. de Mendibil, M. Sarrionandia, J. Aurrekoetxea, J. Acosta, and D. Chico, "Manufacturing cost comparison of RTM, HP-RTM and CRTM for an automotive roof," presented at the 16TH European Conference on Composite Materials, Seville, Spain, 2014.

[14] A. Vita, V. Castorani, M. Germani, and M. Marconi, "Comparative life cycle assessment of low-pressure RTM, compression RTM and high-pressure RTM manufacturing processes to produce CFRP car hoods," *Procedia CIRP*, vol. 80, pp. 352–357, 2019, doi: 10.1016/j.procir.2019.01.109.

[15] N. Lorenz *et al.*, "Characterization and modeling cure- and pressure-dependent thermo-mechanical and shrinkage behavior of fast curing epoxy resins," *Polym. Test.*, vol. 108, p. 107498, Apr. 2022, doi: 10.1016/j.polymertesting.2022.107498.

[16] A. Bernath, L. Kärger, and F. Henning, "Accurate Cure Modeling for Isothermal Processing of Fast Curing Epoxy Resins," *Polymers*, vol. 8, no. 11, p. 390, Nov. 2016, doi: 10.3390/polym8110390.

[17] S. Bickerton and P. A. Kelly, "Compression resin transfer moulding (CRTM) in polymer matrix composites," in *Manufacturing Techniques for Polymer Matrix Composites (PMCs)*, Elsevier, 2012, pp. 348–380. doi: 10.1533/9780857096258.3.348.

[18] L. Khoun, "Process-Induced Stresses and Deformations in Woven Composites Manufactured by Resin Transfer Moulding," PhD Thesis, McGill University, Montreal, Canada, 2009.

[19] S. G. Advani and E. M. Sozer, *Process Modelling in Composite Manufacturing*, 2nd ed. Boca Raton, Florida, USA: CRC Press, Taylor and Francis Group, 2010.

[20] E. W. Liang, H. P. Wang, and E. M. Perry, "An integrated approach for modeling the injection, compression, and resin transfer molding processes for polymers," *Adv. Polym. Technol.*, vol. 12, no. 3, pp. 243–262, 1993, doi: 10.1002/adv.1993.060120303.

[21] X.-T. Pham, F. Trochu, and R. Gauvin, "Simulation of Compression Resin Transfer Molding with Displacement Control," *J. Reinf. Plast. Compos.*, vol. 17, no. 17, Art. no. 17, Dec. 1998, doi: 10.1177/073168449801701704.

[22] W.-B. Young and C.-W. Chiu, "Study on Compression Transfer Molding," *J. Compos. Mater.*, vol. 29, no. 16, pp. 2180–2191, Nov. 1995, doi: 10.1177/002199839502901605.

[23] S. Wirth and R. Gauvin, "Experimental Analysis of Mold Filling in Compression Resin Transfer Molding," *J. Reinf. Plast. Compos.*, vol. 17, no. 16, pp. 1414–1430, Nov. 1998, doi: 10.1177/073168449801701602.

[24] P. Bhat, J. Merotte, P. Simacek, and S. G. Advani, "Process analysis of compression resin transfer molding," *Compos. Part Appl. Sci. Manuf.*, vol. 40, no. 4, Art. no. 4, Apr. 2009, doi: 10.1016/j.compositesa.2009.01.006.

[25] C.-Y. Chang, “Simulation of Compression Effect on Filling Process in Compression Resin Transfer Molding,” *Adv. Compos. Mater.*, vol. 20, no. 2, Art. no. 2, Jan. 2011, doi: 10.1163/092430410X547038.

[26] J. Merotte, P. Simacek, and S. G. Advani, “Resin flow analysis with fiber preform deformation in through thickness direction during Compression Resin Transfer Molding,” *Compos. Part Appl. Sci. Manuf.*, vol. 41, no. 7, pp. 881–887, Jul. 2010, doi: 10.1016/j.compositesa.2010.03.001.

[27] M. K. Kang and W. Il Lee, “Analysis of resin transfer/compression molding process,” *Polym. Compos.*, vol. 20, no. 2, pp. 293–304, Apr. 1999, doi: 10.1002/pc.10356.

[28] A. Keller, C. Dransfeld, and K. Masania, “Flow and heat transfer during compression resin transfer moulding of highly reactive epoxies,” *Compos. Part B Eng.*, vol. 153, pp. 167–175, Nov. 2018, doi: 10.1016/j.compositesb.2018.07.041.

[29] J. Seuffert, L. Kärger, and F. Henning, “Simulating Mold Filling in Compression Resin Transfer Molding (CRTM) Using a Three-Dimensional Finite-Volume Formulation,” *J. Compos. Sci.*, vol. 2, no. 2, p. 23, Apr. 2018, doi: 10.3390/jcs2020023.

[30] J. Seuffert, P. Rosenberg, L. Kärger, F. Henning, M. H. Kothmann, and G. Deinzer, “Experimental and numerical investigations of pressure-controlled resin transfer molding (PC-RTM),” *Adv. Manuf. Polym. Compos. Sci.*, vol. 6, no. 3, Art. no. 3, Jul. 2020, doi: 10.1080/20550340.2020.1805689.

[31] A. Gupta, P. A. Kelly, M. Ehrgott, and S. Bickerton, “A surrogate model based evolutionary game-theoretic approach for optimizing non-isothermal compression RTM processes,” *Compos. Sci. Technol.*, vol. 84, pp. 92–100, Jul. 2013, doi: 10.1016/j.compscitech.2013.05.012.

[32] A. Mamoune, A. Saouab, T. Ouahbi, and C. H. Park, “Simple models and optimization of compression resin transfer molding process,” *J. Reinf. Plast. Compos.*, vol. 30, no. 19, pp. 1629–1648, Oct. 2011, doi: 10.1177/0731684411421539.

[33] A. Ganapathi, S. C. Joshi, and Z. Chen, “Experimental and numerical investigation of process-induced deformations of glass/epoxy wind turbine blade spar cap,” *J. Compos. Mater.*, vol. 51, no. 27, pp. 3791–3806, Nov. 2017, doi: 10.1177/0021998317693909.

[34] P. Bhat, J. Merotte, P. Simacek, and S. G. Advani, “Process analysis of compression resin transfer molding,” *Compos. Part Appl. Sci. Manuf.*, vol. 40, no. 4, pp. 431–441, Apr. 2009, doi: 10.1016/j.compositesa.2009.01.006.

[35] P. Marquette, A. Dereims, T. Ogawa, and M. Kobayashi, “Predictive 3D simulations of Compressive Resin Transfer Molding,” presented at the 12th International Conference on Numerical Methods in Industrial Forming Process, Troyes, France, 2017.

[36] L. Boogh and R. Mezzenga, “Processing Principles for Thermoset Composites,” in *Comprehensive Composite Materials*, Elsevier, 2000, pp. 671–699. doi: 10.1016/B0-08-042993-9/00221-7.

[37] N. Rani, N. Bisht, and S. Chauhan, “Dynamic mechanical analysis of thermosetting polymer composite materials,” in *Dynamic Mechanical and Creep-Recovery Behavior of Polymer-Based Composites*, Elsevier, 2024, pp. 79–112. doi: 10.1016/B978-0-443-19009-4.00007-2.

[38] J. C. Capricho, B. Fox, and N. Hameed, “Multifunctionality in Epoxy Resins,” *Polym. Rev.*, vol. 60, no. 1, pp. 1–41, Jan. 2020, doi: 10.1080/15583724.2019.1650063.

[39] S. Pradhan, “Synthesis and advances in rapid curing resins,” in *Rapid Cure Composites*, Elsevier, 2023, pp. 15–31. doi: 10.1016/B978-0-323-98337-2.00004-3.

[40] N. M. Barkoula, M. Karabela, N. E. Zafeiropoulos, and P. Tsotra, “Fast curing versus conventional resins – degradation due to hygrothermal and UV exposure,” *Express Polym. Lett.*, vol. 14, no. 5, pp. 401–415, 2020, doi: 10.3144/expresspolymlett.2020.34.

[41] Y. Wang, W. Liu, Y. Qiu, and Y. Wei, “Single-component and fast-curing epoxy resin for liquid composite molding processes,” *MATEC Web Conf.*, vol. 130, p. 07005, 2017, doi: 10.1051/matecconf/201713007005.

[42] M. Hayaty, H. Honarkar, and M. H. Beheshty, “Curing behavior of dicyandiamide/epoxy resin system using different accelerators,” *Iran. Polym. J.*, vol. 22, no. 8, pp. 591–598, Aug. 2013, doi: 10.1007/s13726-013-0158-y.

[43] S. Sprenger, M. H. Kothmann, and V. Altstaedt, “Carbon fiber-reinforced composites using an epoxy resin matrix modified with reactive liquid rubber and silica nanoparticles,” *Compos. Sci. Technol.*, vol. 105, pp. 86–95, Dec. 2014, doi: 10.1016/j.compscitech.2014.10.003.

[44] S. Zhang, P. Yang, Y. Bai, T. Zhou, R. Zhu, and Y. Gu, “Polybenzoxazines: Thermal Responsiveness of Hydrogen Bonds and Application as Latent Curing Agents for Thermosetting Resins,” *ACS Omega*, vol. 2, no. 4, pp. 1529–1534, Apr. 2017, doi: 10.1021/acsomega.7b00075.

[45] X. Zhao, Z. Huang, P. Song, H. Yang, and Y. Zhang, “Curing kinetics and mechanical properties of fast curing epoxy resins with isophorone diamine and *N* -(3-aminopropyl)-imidazole,” *J. Appl. Polym. Sci.*, vol. 136, no. 37, p. 47950, Oct. 2019, doi: 10.1002/app.47950.

[46] M. Lang, S. Hirner, F. Wiesbrock, and P. Fuchs, “A Review on Modeling Cure Kinetics and Mechanisms of Photopolymerization,” *Polymers*, vol. 14, no. 10, p. 2074, May 2022, doi: 10.3390/polym14102074.

[47] M. Blanco, M. A. Corcuera, C. C. Riccardi, and I. Mondragon, “Mechanistic kinetic model of an epoxy resin cured with a mixture of amines of different functionalities,” *Polymer*, vol. 46, no. 19, pp. 7989–8000, Sep. 2005, doi: 10.1016/j.polymer.2005.06.117.

[48] Y.-M. Kim, L. K. Kostanski, and J. F. MacGregor, “Kinetic studies of cationic photopolymerizations of cycloaliphatic epoxide, triethyleneglycol methyl vinyl ether, and cyclohexene oxide,” *Polym. Eng. Sci.*, vol. 45, no. 11, pp. 1546–1555, Nov. 2005, doi: 10.1002/pen.20383.

[49] J. M. Matias, P. J. Bartolo, and A. V. Pontes, “Modeling and simulation of photofabrication processes using unsaturated polyester resins,” *J. Appl. Polym. Sci.*, vol. 114, no. 6, pp. 3673–3685, Dec. 2009, doi: 10.1002/app.30405.

[50] Y. Lin and Z. Guan, “The Use of Machine Learning for the Prediction of the Uniformity of the Degree of Cure of a Composite in an Autoclave,” *Aerospace*, vol. 8, no. 5, p. 130, May 2021, doi: 10.3390/aerospace8050130.

[51] A. Woodard, “A Machine Learning Approach for the Modelling of the Cure Kinetics of a Thermoset Resin,” Maters’ Thesis, McGill University, Montreal, Canada, 2022.

[52] J. Barroeta Robles and P. Hubert, “Material characterization of cyanate ester material for structures with high dimensional stability requirements,” *Compos. Part Appl. Sci. Manuf.*, vol. 175, p. 107747, Dec. 2023, doi: 10.1016/j.compositesa.2023.107747.

[53] S. Lee, M. Chiu, and H. Lin, “Kinetic model for the curing reaction of a tetraglycidyl diamino diphenyl methane/diamino diphenyl sulfone (TGDDM/DDS) epoxy resin system,” *Polym. Eng. Sci.*, vol. 32, no. 15, pp. 1037–1046, Aug. 1992, doi: 10.1002/pen.760321509.

[54] U. Khanna and M. Chanda, “Kinetics of anhydride curing of isophthalic diglycidyl ester using differential scanning calorimetry,” *J. Appl. Polym. Sci.*, vol. 49, no. 2, pp. 319–329, Jul. 1993, doi: 10.1002/app.1993.070490212.

[55] K. C. Cole, J. J. Hechler, and D. Noel, “A new approach to modeling the cure kinetics of epoxy/amine thermosetting resins. 2. Application to a typical system based on bis[4-(diglycidylamino)phenyl]methane and bis(4-aminophenyl) sulfone,” *Macromolecules*, vol. 24, no. 11, pp. 3098–3110, May 1991, doi: 10.1021/ma00011a012.

[56] P. Hubert, A. Johnston, A. Poursartip, and K. Nelson, “Cure Kinetics and Viscosity Models for Hexcel 8552 Epoxy Resin,” in *Proceedings of the 46th International SAMPE Symposium*, Long Beach, California, USA.

[57] E. Ruiz and F. Trochu, “Thermomechanical Properties during Cure of Glass-Polyester RTM Composites: Elastic and Viscoelastic Modeling,” *J. Compos. Mater.*, vol. 39, no. 10, pp. 881–916, May 2005, doi: 10.1177/0021998305048732.

[58] J.-L. Bailleul, V. Sobotka, D. Delaunay, and Y. Jarny, “Inverse algorithm for optimal processing of composite materials,” *Compos. Part Appl. Sci. Manuf.*, vol. 34, no. 8, pp. 695–708, Aug. 2003, doi: 10.1016/S1359-835X(03)00141-6.

[59] H. Y. Song, R. Salehiyan, X. Li, S. H. Lee, and K. Hyun, “A comparative study of the effects of cone-plate and parallel-plate geometries on rheological properties under oscillatory shear flow,” *Korea-Aust. Rheol. J.*, vol. 29, no. 4, pp. 281–294, Nov. 2017, doi: 10.1007/s13367-017-0028-9.

[60] N. D. Polychronopoulos and J. Vlachopoulos, “Polymer Processing and Rheology,” in *Cellulose-Based Superabsorbent Hydrogels*, Md. I. H. Mondal, Ed., in Polymers and Polymeric Composites: A Reference Series. , Cham: Springer International Publishing, 2019, pp. 1–47. doi: 10.1007/978-3-319-92067-2_4-1.

[61] J. M. Castro and C. W. Macosko, “Studies of mold filling and curing in the reaction injection molding process,” *AIChE J.*, vol. 28, no. 2, pp. 250–260, Mar. 1982, doi: 10.1002/aic.690280213.

[62] J. B. Robles, “A Streamlined Characterization-Based Selection of Composite Material Systems for Space Structures,” Masters’ Thesis, McGill University, Montreal, Canada, 2017.

[63] D. May and P. Mitschang, “Concept for Darcy-based viscosity measurement for fast-curing resin systems,” *Compos. Commun.*, vol. 27, p. 100881, Oct. 2021, doi: 10.1016/j.coco.2021.100881.

[64] C. Garschke, P. P. Parlevliet, C. Weimer, and B. L. Fox, “Cure kinetics and viscosity modelling of a high-performance epoxy resin film,” *Polym. Test.*, vol. 32, no. 1, pp. 150–157, Feb. 2013, doi: 10.1016/j.polymertesting.2012.09.011.

[65] R. Geissberger, J. Maldonado, N. Bahamonde, A. Keller, C. Dransfeld, and K. Masania, “Rheological modelling of thermoset composite processing,” *Compos. Part B Eng.*, vol. 124, pp. 182–189, Sep. 2017, doi: 10.1016/j.compositesb.2017.05.040.

[66] A. T. DiBenedetto, “Prediction of the glass transition temperature of polymers: A model based on the principle of corresponding states,” *J. Polym. Sci. Part B Polym. Phys.*, vol. 25, no. 9, pp. 1949–1969, Sep. 1987, doi: 10.1002/polb.1987.090250914.

[67] J. P. Pascault and R. J. J. Williams, “Glass transition temperature versus conversion relationships for thermosetting polymers,” *J. Polym. Sci. Part B Polym. Phys.*, vol. 28, no. 1, pp. 85–95, Jan. 1990, doi: 10.1002/polb.1990.090280107.

[68] G. Van Assche, A. Van Hemelrijck, H. Rahier, and B. Van Mele, “Modulated differential scanning calorimetry: isothermal cure and vitrification of thermosetting systems,” *Thermochim. Acta*, vol. 268, pp. 121–142, Dec. 1995, doi: 10.1016/0040-6031(95)02693-2.

[69] P. K. Mallick, *Fiber-Reinforced Composites*, Third edition. Boca Raton, Florida, USA: CRC Press, Taylor and Francis Group, 2007.

[70] “Reinforcement Fiber Reference,” Explore Composites! Accessed: Jan. 27, 2024. [Online]. Available: https://explorecomposites.com/materials-library/fiber-ref/

[71] F. Henning, L. Kärger, D. Dörr, F. J. Schirmaier, J. Seuffert, and A. Bernath, “Fast processing and continuous simulation of automotive structural composite components,” *Compos. Sci. Technol.*, vol. 171, pp. 261–279, Feb. 2019, doi: 10.1016/j.compscitech.2018.12.007.

[72] M. R. Garnich and G. Karami, “Finite Element Micromechanics for Stiffness and Strength of Wavy Fiber Composites,” *J. Compos. Mater.*, vol. 38, no. 4, pp. 273–292, Feb. 2004, doi: 10.1177/0021998304039270.

[73] S. Pansart, M. Sinapius, and U. Gabbert, “A comprehensive explanation of compression strength differences between various CFRP materials: Micro-meso model, predictions,

parameter studies," *Compos. Part Appl. Sci. Manuf.*, vol. 40, no. 4, pp. 376–387, Apr. 2009, doi: 10.1016/j.compositesa.2009.01.004.

[74] B. D. Allison and J. L. Evans, "Effect of fiber waviness on the bending behavior of S-glass/epoxy composites," *Mater. Des. 1980-2015*, vol. 36, pp. 316–322, Apr. 2012, doi: 10.1016/j.matdes.2011.11.012.

[75] A. C. Long, *Design and manufacture of textile composites*. Elsevier, 2005.

[76] L. P. Brown and A. C. Long, "Modeling the geometry of textile reinforcements for composites: TexGen," in *Composite Reinforcements for Optimum Performance*, Elsevier, 2021, pp. 237–265. doi: 10.1016/B978-0-12-819005-0.00008-3.

[77] H. Darcy, Paris: Victor Dalmont: Les Fontaines Publiques de la Ville de Dijon, 1856.

[78] R. Arbter *et al.*, "Experimental determination of the permeability of textiles: A benchmark exercise," *Compos. Part Appl. Sci. Manuf.*, vol. 42, no. 9, pp. 1157–1168, Sep. 2011, doi: 10.1016/j.compositesa.2011.04.021.

[79] M. Hattabi, J. Echaabi, M. O. Bensalah, J. Bréeard, and A. Saouab, "Flow Analysis during On-line and Radial Injection Applications in Permeability Measurements," *J. Reinf. Plast. Compos.*, vol. 24, no. 18, pp. 1909–1920, Dec. 2005, doi: 10.1177/0731684405054356.

[80] E. Fauster *et al.*, "Image processing and data evaluation algorithms for reproducible optical in-plane permeability characterization by radial flow experiments," *J. Compos. Mater.*, vol. 53, no. 1, pp. 45–63, Jan. 2019, doi: 10.1177/0021998318780209.

[81] D. Becker, H. Grössing, S. Konstantopoulos, E. Fauster, P. Mitschang, and R. Schledjewski, "An evaluation of the reproducibility of ultrasonic sensor-based out-of-plane permeability measurements: a benchmarking study," *Adv. Manuf. Polym. Compos. Sci.*, vol. 2, no. 1, pp. 34–45, Jan. 2016, doi: 10.1080/20550340.2016.1182783.

[82] A. X. H. Yong *et al.*, "Out-of-plane permeability measurement for reinforcement textiles: A benchmark exercise," *Compos. Part Appl. Sci. Manuf.*, vol. 148, p. 106480, Sep. 2021, doi: 10.1016/j.compositesa.2021.106480.

[83] Q. Govignon, S. Bickerton, and P. A. Kelly, "Simulation of the complete resin infusion process," presented at the 9th International Conference on Flow Processes in Composite Materials, Montreal, Quebec, Canada, Jul. 2018.

[84] P. B. Nedanov and S. G. Advani, "Numerical computation of the fiber preform permeability tensor by the homogenization method," *Polym. Compos.*, vol. 23, no. 5, pp. 758–770, Oct. 2002, doi: 10.1002/pc.10474.

[85] R. S. Pierce and B. G. Falzon, "Simulating Resin Infusion through Textile Reinforcement Materials for the Manufacture of Complex Composite Structures," *Engineering*, vol. 3, no. 5, pp. 596–607, Oct. 2017, doi: 10.1016/J.ENG.2017.04.006.

[86] R. S. Pierce, B. G. Falzon, and M. C. Thompson, "Permeability characterization of sheared carbon fiber textile preform," *Polym. Compos.*, vol. 39, no. 7, pp. 2287–2298, Jul. 2018, doi: 10.1002/pc.24206.

[87] J. Seuffert, L. Bittrich, L. Cardoso De Oliveira, A. Spickenheuer, and L. Kärger, “Micro-Scale Permeability Characterization of Carbon Fiber Composites Using Micrograph Volume Elements,” *Front. Mater.*, vol. 8, p. 745084, Oct. 2021, doi: 10.3389/fmats.2021.745084.

[88] A. Dei Sommi, F. Lionetto, and A. Maffezzoli, “An Overview of the Measurement of Permeability of Composite Reinforcements,” *Polymers*, vol. 15, no. 3, p. 728, Jan. 2023, doi: 10.3390/polym15030728.

[89] M. A. Ali, “In-plane virtual permeability characterization of 3D woven fabrics using a hybrid experimental and numerical approach,” *Compos. Sci. Technol.*, 2019.

[90] E. Syerko *et al.*, “Benchmark exercise on image-based permeability determination of engineering textiles: Microscale predictions,” *Compos. Part Appl. Sci. Manuf.*, vol. 167, p. 107397, Apr. 2023, doi: 10.1016/j.compositesa.2022.107397.

[91] B. Yang, Q. Tang, S. Wang, T. Jin, and F. Bi, “Three-dimensional numerical simulation of the filling stage in resin infusion process,” *J. Compos. Mater.*, vol. 50, no. 29, pp. 4171–4186, Dec. 2016, doi: 10.1177/0021998316631809.

[92] T. G. Gutowski, T. Morigaki, and Zhong Cai, “The Consolidation of Laminate Composites,” *J. Compos. Mater.*, vol. 21, no. 2, pp. 172–188, Feb. 1987, doi: 10.1177/002199838702100207.

[93] T. G. Gutowski, J. Kingery, and D. Boucher, “Experiments in Composites Consolidation: Fiber Deformation,” in *Society of Plastics Engineers 44th Annual Technical Conference & Exhibit.*, 1986, pp. 1316–1320.

[94] B. Yenilmez, B. Caglar, and E. M. Sozer, “Viscoelastic modeling of fiber preform compaction in vacuum infusion process,” *J. Compos. Mater.*, vol. 51, no. 30, pp. 4189–4203, Dec. 2017, doi: 10.1177/0021998317699983.

[95] P. Simacek, D. Heider, J. W. Gillespie, and S. Advani, “Post-filling flow in vacuum assisted resin transfer molding processes: Theoretical analysis,” *Compos. Part Appl. Sci. Manuf.*, vol. 40, no. 6–7, pp. 913–924, Jul. 2009, doi: 10.1016/j.compositesa.2009.04.018.

[96] N. C. Correia, F. Robitaille, A. C. Long, C. D. Rudd, P. Šimáček, and S. G. Advani, “Analysis of the vacuum infusion moulding process: I. Analytical formulation,” *Compos. Part Appl. Sci. Manuf.*, vol. 36, no. 12, pp. 1645–1656, Dec. 2005, doi: 10.1016/j.compositesa.2005.03.019.

[97] S. Bickerton, M. J. Buntain, and A. A. Somashekar, “The viscoelastic compression behavior of liquid composite molding preforms,” *Compos. Part Appl. Sci. Manuf.*, vol. 34, no. 5, pp. 431–444, May 2003, doi: 10.1016/S1359-835X(03)00088-5.

[98] S. Bickerton and P. A. Kelly, “Compression resin transfer moulding (CRTM) in polymer matrix composites,” in *Manufacturing Techniques for Polymer Matrix Composites (PMCs)*, Elsevier, 2012, pp. 348–380. doi: 10.1533/9780857096258.3.348.

[99] F. Trochu, N. Vernet, Y. Sun, J. Echaabi, A. Makradi, and S. Belouettar, “Hybrid twin models of fiber compaction for composite manufacturing based on dual kriging,” *Int. J. Mater. Form.*, vol. 15, no. 3, p. 36, May 2022, doi: 10.1007/s12289-022-01679-3.

[100] P. A. Kelly, “A viscoelastic model for the compaction of fibrous materials,” *J. Text. Inst.*, vol. 102, no. 8, pp. 689–699, Aug. 2011, doi: 10.1080/00405000.2010.515103.

[101] A. X. H. Yong *et al.*, “Experimental characterisation of textile compaction response: A benchmark exercise,” *Compos. Part Appl. Sci. Manuf.*, vol. 142, p. 106243, Mar. 2021, doi: 10.1016/j.compositesa.2020.106243.

[102] K. M. Pillai, C. L. Tucker, and F. R. Phelan, “Numerical simulation of injection/compression liquid composite molding. Part 1. Mesh generation,” *Compos. Part Appl. Sci. Manuf.*, vol. 31, no. 1, pp. 87–94, Jan. 2000, doi: 10.1016/S1359-835X(99)00052-4.

[103] K. M. Pillai, C. L. Tucker, and F. R. Phelan, “Numerical simulation of injection/compression liquid composite molding. Part 2: preform compression,” *Compos. Part Appl. Sci. Manuf.*, vol. 32, no. 2, pp. 207–220, Feb. 2001, doi: 10.1016/S1359-835X(00)00137-8.

[104] A. Shojaei, “Numerical simulation of three-dimensional flow and analysis of filling process in compression resin transfer moulding,” *Compos. Part Appl. Sci. Manuf.*, vol. 37, no. 9, pp. 1434–1450, Sep. 2006, doi: 10.1016/j.compositesa.2005.06.021.

[105] P. A. Kelly, R. Umer, and S. Bickerton, “Viscoelastic response of dry and wet fibrous materials during infusion processes,” *Compos. Part Appl. Sci. Manuf.*, vol. 37, no. 6, pp. 868–873, Jun. 2006, doi: 10.1016/j.compositesa.2005.02.008.

[106] P. A. Kelly, S. Bickerton, and J. Cheng, “Transverse Compression Properties of Textile Materials,” *Adv. Mater. Res.*, vol. 332–334, pp. 697–701, Sep. 2011, doi: 10.4028/www.scientific.net/AMR.332-334.697.

[107] J. Lee, M. Duhovic, T. Allen, and P. Kelly, “Transverse liquid composite moulding processes for advanced composites material manufacturing,” *Plast. Rubber Compos.*, vol. 51, no. 8, pp. 373–382, Sep. 2022, doi: 10.1080/14658011.2022.2108983.

[108] J. Lee, M. Duhovic, T. Allen, D. May, and P. Kelly, “Computational modelling and analysis of transverse liquid composite moulding processes,” *Compos. Part Appl. Sci. Manuf.*, vol. 167, p. 107433, Apr. 2023, doi: 10.1016/j.compositesa.2023.107433.

[109] J. Lee, M. Duhovic, T. Allen, and P. Kelly, “Sensitivity of transverse Liquid Composite Moulding processing predictions to variations in constitutive data,” *Adv. Manuf. Polym. Compos. Sci.*, vol. 9, no. 1, p. 2266288, Jan. 2023, doi: 10.1080/20550340.2023.2266288.

[110] P. Marquette, A. Dereims, T. Ogawa, and M. Kobayashi, “Numerical methods for 3D compressive RTM simulations,” presented at the 17th European Conference on Composite Materials, Munich, Germany, 2017.

[111] A. Dereims *et al.*, “Compression Resin Transfer Molding (C-RTM) Simulation Using a Coupled Fluid-solid Approach,” in *American Society for Composites 2017*, DEStech Publications, Inc., Nov. 2017. doi: 10.12783/asc2017/15224.

[112] V. Guerriero and S. Mazzoli, “Theory of Effective Stress in Soil and Rock and Implications for Fracturing Processes: A Review,” *Geosciences*, vol. 11, no. 3, p. 119, Mar. 2021, doi: 10.3390/geosciences11030119.

[113] A. Dereims, S. Chatel, P. Marquette, L. Dufort, and A. C. Aeroparc, “Accurate liquid resin infusion simulation throug a Fluid-Solid coupled approach,” 2017.

[114] E. Ruiz, and F. Trochu, “Coupled Non-Conforming Finite Element and Finite Difference Approximation Based on Laminate Extrapolation to Simulate Liquid Composite Molding Processes. Part II: Non-Isothermal Filling and Curing,” *Sci. Eng. Compos. Mater.*, vol. 14, no. 2, pp. 113–144, Jun. 2007, doi: 10.1515/SECM.2007.14.2.113.

[115] M. Deléglise, P. Le Grognec, C. Binetruy, P. Krawczak, and B. Claude, “Modeling of high speed RTM injection with highly reactive resin with on-line mixing,” *Compos. Part Appl. Sci. Manuf.*, vol. 42, no. 10, pp. 1390–1397, Oct. 2011, doi: 10.1016/j.compositesa.2011.06.002.

[116] F. A. Martin *et al.*, “Simulation and Validation of Injection-Compression Filling Stage of Liquid Moulding with Fast Curing Resins,” *Appl. Compos. Mater.*, vol. 26, no. 1, pp. 41–63, Feb. 2019, doi: 10.1007/s10443-018-9682-4.

[117] P. Simacek, N. Niknafs Kermani, and S. G. Advani, “Coupled Process Modeling of Flow and Transport Phenomena in LCM Processing,” *Integrating Mater. Manuf. Innov.*, vol. 11, no. 3, pp. 363–381, Sep. 2022, doi: 10.1007/s40192-022-00268-1.

[118] P. A. Kelly and S. Bickerton, “A comprehensive filling and tooling force analysis for rigid mould LCM processes,” *Compos. Part Appl. Sci. Manuf.*, vol. 40, no. 11, pp. 1685–1697, Nov. 2009, doi: 10.1016/j.compositesa.2009.07.013.

[119] B. Verleye, W. A. Walbran, S. Bickerton, and P. A. Kelly, “Simulation and experimental validation of force controlled compression resin transfer molding,” *J. Compos. Mater.*, vol. 45, no. 7, pp. 815–829, Apr. 2011, doi: 10.1177/0021998310376110.

[120] B. Yang, T. Jin, J. Li, and F. Bi, “Three-Dimensional Numerical Simulation of Mold Filling Process in Compression Resin Transfer Molding,” *Appl. Compos. Mater.*, vol. 22, no. 2, pp. 209–230, Apr. 2015, doi: 10.1007/s10443-014-9402-7.

[121] C.-Y. Chang, L.-W. Hourng, and T.-Y. Chou, “Effect of Process Variables on the Quality of Compression Resin Transfer Molding,” *J. Reinf. Plast. Compos.*, vol. 25, no. 10, pp. 1027–1037, Jul. 2006, doi: 10.1177/0731684406064997.

[122] V. Achim and E. Ruiz, “Guiding selection for reduced process development time in RTM,” *Int. J. Mater. Form.*, vol. 3, no. S2, pp. 1277–1286, Sep. 2010, doi: 10.1007/s12289-009-0630-6.

[123] L. Kärger *et al.*, “Development and validation of a CAE chain for unidirectional fibre reinforced composite components,” *Compos. Struct.*, vol. 132, pp. 350–358, Nov. 2015, doi: 10.1016/j.compstruct.2015.05.047.

[124] M. Baskaran, L. Aretxabaleta, M. Mateos, and J. Aurrekoetxea, “Simulation and experimental validation of the effect of material and processing parameters on the injection stage of compression resin transfer molding,” *Polym. Compos.*, vol. 39, no. 12, pp. 4333–4340, Dec. 2018, doi: 10.1002/pc.24514.

[125] C. Di Fratta, Y. Sun, P. Causse, and F. Trochu, “A Dimensionless Characteristic Number for Process Selection and Mold Design in Composites Manufacturing: Part II—Applications,” *J. Compos. Sci.*, vol. 4, no. 1, p. 10, Jan. 2020, doi: 10.3390/jcs4010010.

[126] C. Di Fratta, Y. Sun, P. Causse, and F. Trochu, “A Dimensionless Characteristic Number for Process Selection and Mold Design in Composites Manufacturing: Part I—Theory,” *J. Compos. Sci.*, vol. 4, no. 1, p. 11, Jan. 2020, doi: 10.3390/jcs4010011.

[127] J. Wang, P. Simacek, and S. G. Advani, “Use of medial axis to find optimal channel designs to reduce mold filling time in resin transfer molding,” *Compos. Part Appl. Sci. Manuf.*, vol. 95, pp. 161–172, Apr. 2017, doi: 10.1016/j.compositesa.2017.01.003.

[128] N. Wright, P. Kelly, O. Maclaren, R. Nicholson, and S. Advani, “Bayesian Optimal Experimental Design for Race Tracking in Resin Transfer Moulding,” *Appl. Sci.*, vol. 13, no. 20, p. 11606, Oct. 2023, doi: 10.3390/app132011606.

[129] T. Chen and B. Rajaram, “Characterizing Thermoset Curing Using Rheology,” in *SAMPE 2019 - Charlotte, NC*, SAMPE, Apr. 2019. doi: 10.33599/nasampe/s.19.1595.

[130] L. Khoun and P. Hubert, “Investigation of the dimensional stability of carbon epoxy cylinders manufactured by resin transfer moulding,” *Compos. Part Appl. Sci. Manuf.*, vol. 41, no. 1, pp. 116–124, Jan. 2010, doi: 10.1016/j.compositesa.2009.06.014.

[131] A. M. Brown, “A step-by-step guide to non-linear regression analysis of experimental data using a Microsoft Excel spreadsheet,” *Comput. Methods Programs Biomed.*, vol. 65, no. 3, pp. 191–200, Jun. 2001, doi: 10.1016/S0169-2607(00)00124-3.

[132] N. Kiuna, C. J. Lawrence, Q. P. V. Fontana, P. D. Lee, T. Selerland, and P. D. M. Spelt, “A model for resin viscosity during cure in the resin transfer moulding process,” *Compos. Part Appl. Sci. Manuf.*, vol. 33, no. 11, pp. 1497–1503, Nov. 2002, doi: 10.1016/S1359-835X(02)00177-X.

[133] Z. Han *et al.*, “Polyester conversion by homogeneous catalysis for separating and recycling ammonia from biogas,” *Sci. Total Environ.*, vol. 907, p. 168138, Jan. 2024, doi: 10.1016/j.scitotenv.2023.168138.

[134] I. Baran, R. Akkerman, and J. H. Hattel, “Material characterization of a polyester resin system for the pultrusion process,” *Compos. Part B Eng.*, vol. 64, pp. 194–201, Aug. 2014, doi: 10.1016/j.compositesb.2014.04.030.

[135] J. Bae, “Drapability Characterization of Dry Non-Crimp Fabrics for Preforming Simulations,” McGill University, Montreal, 2022.

[136] M. Karaki, R. Younes, F. Trochu, and P. Lafon, “Progress in Experimental and Theoretical Evaluation Methods for Textile Permeability,” *J. Compos. Sci.*, vol. 3, no. 3, p. 73, Jul. 2019, doi: 10.3390/jcs3030073.

[137] N. Vernet, “Experimental determination of the permeability of engineering textiles: Benchmark II,” 2014.

[138] M. Karaki, A. Hallal, R. Younes, F. Trochu, and P. Lafon, “In-plane permeability prediction model for non-crimp and 3D orthogonal fabrics,” *J. Text. Inst.*, vol. 109, no. 8, pp. 1110–1126, Aug. 2018, doi: 10.1080/00405000.2017.1409327.

[139] P. Hubert, “Aspects of Flow and Compaction of Laminated Composite Shapes During Cure,” University of British Columbia, Vancouver, Canada, 1996.

[140] F. Trochu, R. Gauvin, and D.-M. Gao, “Numerical analysis of the resin transfer molding process by the finite element method,” *Adv. Polym. Technol.*, vol. 12, no. 4, pp. 329–342, 1993, doi: 10.1002/adv.1993.060120401.

[141] A. Dereims, S. Drapier, J.-M. Bergheau, and P. De Luca, “3D robust iterative coupling of Stokes, Darcy and solid mechanics for low permeability media undergoing finite strains,” *Finite Elem. Anal. Des.*, vol. 94, pp. 1–15, Feb. 2015, doi: 10.1016/j.finel.2014.09.003.

[142] *PAM-CMPOSITES, ESI Group*. Accessed: Dec. 10, 2023. [Online]. Available: https://www.esi-group.com/products/pam-composites

[143] I. V. Terekhov and E. M. Chistyakov, “Binders Used for the Manufacturing of Composite Materials by Liquid Composite Molding,” *Polymers*, vol. 14, no. 1, p. 87, Dec. 2021, doi: 10.3390/polym14010087.

[144] M. Tonejc, C. Ebner, E. Fauster, and R. Schledjewski, “Influence of test fluids on the permeability of epoxy powder bindered non-crimp fabrics,” *Adv. Manuf. Polym. Compos. Sci.*, vol. 5, no. 3, pp. 128–139, Jul. 2019, doi: 10.1080/20550340.2019.1647371.

[145] J. Fernández-León, K. Keramati, L. Baumela, and C. González, “A digital twin for smart manufacturing of structural composites by liquid moulding,” *Int. J. Adv. Manuf. Technol.*, vol. 130, no. 9–10, pp. 4679–4697, Feb. 2024, doi: 10.1007/s00170-023-12637-x.

[146] S. Zambal, C. Eitzinger, M. Clarke, J. Klintworth, and P.-Y. Mechin, “A digital twin for composite parts manufacturing : Effects of defects analysis based on manufacturing data,” in *2018 IEEE 16th International Conference on Industrial Informatics (INDIN)*, Porto: IEEE, Jul. 2018, pp. 803–808. doi: 10.1109/INDIN.2018.8472014.

[147] J. P.-H. Belnoue and S. R. Hallett, “4. Process models: A cornerstone to composites 4.0,” *Compos. Part B Eng.*, vol. 283, p. 111621, Aug. 2024, doi: 10.1016/j.compositesb.2024.111621.

APPENDIX

This section includes the algorithm used for generating the process map for non-isothermal CRTM process. The algorithm was implemented using Python.

Algorithm: *Optimization using Injectability Number* $\boldsymbol{In}$

Input: *In from initial isothermal simulation*

Input: *Temperature list* T_{inj_list}, T_{mould_list}, *pressure list* P_{inj_list}, *fill time range* t_{min}, t_{max}

Output: *Optimized values:* P_{inj}, T_{inj}, T_{mould}, t_{inj}, η

For T_{inj} *in* T_{inj_list} ***do***

  For T_{mould} *in* T_{mould_list} ***do***

    Compute temperature profile T (Eq. 6-4)

    Compute $\dot{\alpha}$, α, η

    For P_{inj} *in* P_{inj_list} ***do***

      Calculate t_{inj} *as*

        $t_{inj} = \underset{\tau>0}{argmin}\left(\left|In - \int_0^{t_{inj}} \frac{P_{inj}(t)}{\eta(\alpha(t),T(t))}\,dt\right|\right)$ *(Eq. 6.3)*

        If $\alpha < \alpha_{gel}$ ***and*** $t_{min} \leq t_{inj} \leq t_{max}$

          Save values

        end

      end

  end

end

Output optimized values